CONTACT MECHANICS BASED MECHANICAL CHARACTERIZATION OF PORTLAND CEMENT PASTE

A Dissertation

by

CHRISTOPHER ANDREW JONES

Submitted to the Office of Graduate Studies of
Texas A&M University
in partial fulfillment of the requirements for the degree of

DOCTOR OF PHILOSOPHY

December 2011

Major Subject: Civil Engineering

Contact Mechanics Based Mechanical Characterization of Portland Cement Paste

CONTACT MECHANICS BASED MECHANICAL CHARACTERIZATION OF PORTLAND CEMENT PASTE

A Dissertation

by

CHRISTOPHER ANDREW JONES

Submitted to the Office of Graduate Studies of
Texas A&M University
in partial fulfillment of the requirements for the degree of

DOCTOR OF PHILOSOPHY

Approved by:

Chair of Committee,	Zachary C. Grasley
Committee Members,	Robert L. Lytton
	Dan G. Zollinger
	Amine A. Benzerga
Head of Department,	John M. Niedzwecki

December 2011

Major Subject: Civil Engineering

ABSTRACT

Contact Mechanics Based Mechanical Characterization of Portland Cement Paste.

(December 2011)

Christopher Andrew Jones, B.A., Southwestern University; B.S., M.S.; Texas A&M University

Chair of Advisory Committee: Dr. Zachary C. Grasley

Current research interest in multi-scale modeling of cement paste requires accurate characterization of the time-dependent mechanical properties of the material, particularly the C-S-H phase. Nanoindentation is evaluated as a tool for measuring both the instantaneous and the short-term viscoelastic properties of cement paste. Atomic force microscopy (AFM) based indentation is compared to conventional nanoindentaion in measuring mechanical properties of cement pastes. Time-dependent solutions are derived to characterize creep indentation tests performed on hardened cement paste and to extract the time-dependent properties. The effect of approximating C-S-H viscoelastic properties with a time-independent Poisson's ratio is discussed, and arguments for utilizing a time-independent Poisson's ratio for short-term response are presented. In evaluating AFM as a mechanical characterization tool, various analytical and numerical modeling approaches are compared. The disparities between the numerical self-consistent approach and analytical solutions are determined and reported.

The measured elastic Young's modulus values acquired by AFM indentation tests are compared to Young's modulus values from nanoindentation measurements from cement paste. These results show that the calcium silicate hydrate (C-S-H) phase of hydrated portland cement has different properties on the nanometric scale than on the micron scale. Packing density of C-S-H particles is proposed as an explanation for the disparity in the measured results.

The AFM measured uniaxial viscoelastic compliance values are compared to similar values obtained with traditional nanoindentation for the same material. The comparison of these results shows that the calcium silicate hydrate (C-S-H) phase of portland cement has similar but distinct properties on the sub micron scale than on the micron scale. Additionally, the effect of moisture is evaluated by controlling the relative humidity (RH) of the testing environment between 40% and 100% plus, or wet. The viscoelastic compliance appears to be highest at 40% RH and the material appears to be less compliant at higher relative humidity levels. Possible mechanisms controlling the viscoelastic deformation are presented and evaluated in conjunction with the moisture related poromechanical effect.

DEDICATION

I dedicate this dissertation to my sweet wife Lauren. Without her support, particularly in these last weeks and months, I doubt if I could have completed this goal.

ACKNOWLEDGEMENTS

I would like to thank a number of individuals for their help with this work. First, I must thank Dr. Grasley for his continual encouragement, technical and personal guidance, and for providing me many opportunities for success. Second, I would like to thank Tony Ohlhausen for his large role in facilitating the experimental portion of my research. Without my time at Sandia National Laboratories, made possible by Tony, there is simply no way that I would be finishing up right now. Additionally, I would like to thank my other committee members, Dr. Lytton, Dr. Zollinger, and Dr. Benzerga for serving me with excellent technical instruction in the classroom and for providing excellent technical feedback on my work. Also special thanks are owed to Dr. Muliana and to Dr. Gharaibeh for filling at the defense at the last moment. I appreciate each of you immensely.

I would also like to thank Sandia National Laboratories, The National Institute for Nano Engineering, and the National Science Foundation for providing facility, organizational, and monetary support for my work here at Texas A&M. Without these resources, I believe that I would not be where I am.

Finally, I thank my parents for the opportunity and encouragement to initially pursue higher education and my wife Lauren for supporting me in so many ways in this process.

NOMENCLATURE

a	contact radius
A	Hammaker's constant
AFM	atomic force microscopy
C-S-H	calcium silicate hydrate
Cov	covariance
δ	the depth of penetration of the indenter
E	elastic Young's modulus
$E(t)$	viscoelastic Young's modulus
$E_0, E_1, E_2, E_3, \beta$	viscoelastic fitting parameters
F	force applied to the indenter
ϕ	half angle of the conical indenter
G	elastic shear modulus
$G(t)$	viscoelastic shear modulus
γ	surface energy
h	surface separation
h_0	rigid separation
$H(t)$	Heaviside function
J	elastic compliance
$J(t)$	viscoelastic compliance

k	cantilever stiffness
κ	Poisson-Boltzman exponent
K	elastic bulk modulus
$K(t)$	viscoelastic bulk modulus
M	indentation modulus
ν	Poisson's ratio
$\nu(t)$	viscoelastic Poisson's ratio
P	probability
p_s	surface pressure
P_0	maximum Hertz pressure
r	radial coordinate for axisymmetry
R	tip radius
RH	relative humidity
t	time
t_l	loading time
t_h	load holding time
t_u	unloading time
θ	dimensionless parameter for evaluation
τ	characteristic time
u	surface displacement
Var	variance

w/c	water to cement
z_0	equilibrium separation distance

TABLE OF CONTENTS

Page

CHAPTER Page

Page

LIST OF FIGURES

Page

Page

Page

Page

LIST OF TABLES

Page

CHAPTER I

INTRODUCTION AND PROBLEM STATEMENT

Portland cement concrete is a heterogeneous composite composed of portland cement, water and natural mineral aggregates that is the most widely consumed manmade material worldwide [1]. Despite being widely used for over a century, various problems still plague concrete infrastructure today such as chemical attack [2], limited freeze thaw durability [3], and reinforcement corrosion [4]. Furthermore, concrete structures tend to be difficult and expensive to retrofit or repair when unexpected problems do arise [5].

Despite the ubiquity of concrete, many of its fundamental material properties, particularly at small length scales, are not well understood. This is likely due to the lack of a regular microstructure in the portland cement paste. The calcium silicate hydrate (C-S-H) phase of the cement paste is generally understood to be crystalline on the atomic to molecular scale and amorphous on any larger scale [6]. The C-S-H phase is of particular interest since its properties tend to control the properties of the bulk concrete. Unfortunately, since the microstructure and fundamental deformation mechanisms are not very well understood, predicting mechanical properties from material inputs has not progressed much from the early empirical work of Abrams [7].

This dissertation follows the style of Cement and Concrete Composites.

With the recent interest in muli-scale constitutive modeling of infrastructure materials, the promise of accurate mechanical predictions from mathematical models has created some excitement in the materials community. For example, CEMHYD3D, created at the National Institute for Standards and Technology, provides realistic three dimensional microstructure and can be used with finite element modeling to predict elastic properties for cement paste [8]. Current efforts aim to create similar models for predicting viscoelastic properties.

Given the multi length scale heterogeneity of cement paste, fundamentally accurate models must account for mechanical behavior on these different length scales. In an effort to effectively model the multi-scale response of portland cement concrete, experimental techniques are required that characterize the material on ever shorter length scales. In addition to providing intrinsic input properties for multi-scale models [9-13] for predicting the macroscale behavior of cement paste and concrete, measuring fundamental mechanical properties on the micro to nanometer length scale enhances the understanding of concrete deformation mechanisms. The indentation technique provides an excellent means for obtaining the mechanical properties from a localized region of a material.

Recent technology has made measurement of mechanical properties on these ever-decreasing length scales possible. The nanoindentation technique is particularly appealing for use on cement paste because the small probe dimensions allow measurement of the properties on short enough length scales to discern heterogeneity in mechanical properties. Furthermore atomic force microscopy (AFM) provides an even

smaller probe that can be used to extract properties from yet shorter length scales [14-18]. Nanoindentation has long been the method of choice for micromechanical characterization of all sorts of materials [19-23], but when applied to cementitious materials, the interpretation of the measured results are complicated by the somewhat ambiguous nanostructure of the calcium silicate hydrate (C-S-H) phase of portland cement paste.

Several studies have been conducted using the nanoindentation technique on cement and concrete to measure elastic properties. Velez et. al performed nanoindentation experiments on portland cement clinker and measured properties for the main phases [21]. Multiple studies have investigated the elastic properties of hydrated portland cement paste [24-30] with various experiments and calculations. Nanoindentation has also been used to measure elastic properties of phases in atypical cements and cement composites [15, 23]. The existence of low density and high density C-S-H first proposed by Jennings and collaborators [31-33] was later utilized as an explanation for the bimodal distribution of elastic properties measured by Ulm and collaborators [34-36]. Trtik et al. [37] suggested that the presence of varying amounts of crystalline products (such as unhydrated cement or calcium hydroxide) within the nanoindentation interaction volume provide a more likely explanation for the measured bimodal distribution of elastic properties when ostensibly indenting C-S-H. However, Ulm et al. [38] subsequently provided evidence that large enough compositionally homogenous regions exist in hardened cement paste such that the nanoindentation interaction volume may often be a (compositionally) single phase; as such, the bimodal

distribution of measured elastic properties in indentation of cement paste would suggest two types of C-S-H. More recent studies have proposed the existence of a third distinct phase or a trimodal distribution of measured elastic properties [29, 39].

The mechanical properties of hardened portland cement paste have been shown to be time dependent by various experimental methods, (e.g. [40-44]) and the time dependency has traditionally been attributed to the C-S-H phase of the paste. While the nanoindentation technique has most often been used for determination of elastic properties, recently the technique has been applied to measure time-dependent mechanical properties as well. This time dependency has generally been considered detrimental; however, if this time dependent mechanical behavior of C-S-H were better understood, perhaps it could be used for beneficial purposes such as mitigating shrinkage cracking or facilitating healing of cementitious materials. In the present work, the term "viscoelastic" will be used in a very broad sense to encompass any sort of time dependent mechanical behavior to include viscoplasticity, apparent viscoelasticity arising from poromechanical relaxation, and true viscoelasticity.

The specific mechanism responsible for the time dependency of the mechanical properties of portland cement paste is not clear from the literature and is likely not a single specific mechanism but rather a combination of different mechanisms acting in concert. Powers offered one of the earliest discussions of the phenomenon and suggested that creep of concrete is related to the seepage of physically bound water into the capillary pores of the pasted thus creating an apparent viscoelastic effect [45]. Power's theory is commonly referred to as seepage theory in the literature. Feldman

hypothesized that creep in cementitious materials is related to the formation of new interlayer space as the C-S-H crystallizes and this mechanism is referred to as the interlayer theory in the literature [46]. The rearrangement of C-S-H particles in response to localized shear stress has been theorized as the mechanism responsible for creep of cementitious materials by several researchers [43, 47-49]. This mechanism of viscoelastic response is known as the viscous shear theory, and is presented in different forms relating to the assumed structure of the C-S-H. Cementitious materials have also been considered poromechanical materials by various researchers [50-52]. The poromechanical response is related to the movement of fluid within the porous cement paste in response to pressure gradients from the applied mechanical stress, but is distinct from the seepage theory in that it only considers unbound water that can readily flow through the pore network. As a result, the poromechanical response of cement paste is considered only a short term phenomenon. Additionally, a more recently proposed mechanism involves the dissolution and reformation of load bearing phases in response to stress applied to the paste [53].

While numerous studies have investigated the elastic properties of cement paste using nanoindentation, fewer studies have been conducted that investigate the nanoindentation technique as a tool for measuring viscoelastic properties of cementitious materials. Vandamme and Ulm provide solutions for the problem of time-dependent indentation and perform some experiments to validate the solutions [54]. Additionally, Vandamme and Ulm show that the measured “creep modulus” indicates the presence of low density C-S-H, high density C-S-H, and an ultra-high density C-S-H [55]. Nemecek

et. al also considered nanoindentation creep as it affects the measured elastic properties of cement paste [56].

Some general solutions for time-dependent indentation also exist in the literature. Cheng offers a viscoelastic solution for a spherical indenter [57] and a flat punch indenter [58], neither of which extend well to more common conical indenters. Cheng and Cheng also provide an excellent review of various phenomena present in indentation including indentation solutions for viscoelastic materials [59] for constant displacement rate indentation tests. Other studies have been aimed at accounting for the viscoelastic dissipation that occurs when performing elastic indentations [56, 60]. Fischer-Cripps [61] proposed a straightforward, phenomenological solution to characterize indentation creep, but the solution is empirical and thus not useful for understanding fundamental material behavior.

To date the application of time-dependent nanoindentation to cementitious materials has been limited. This study aims to characterize the short-term time-dependent viscoelastic Young's modulus of C-S-H using nanoindentation. Various assumptions made while formulating a time-dependent indentation solution will also be analyzed and a generalized solution for time-dependent indentation response of a viscoelastic material to a step loading will be presented.

Nanoscale mechanical characterization of portland cement paste has yielded interesting new findings about this ubiquitous construction material but has also raised many questions as well. There exists a great deal of ongoing discussion regarding the

interepretation of nanoindentation results obtained from testing portland cement. Specifically in question is the source of the multimodal distribution of measured properties reported in virtually every nanoindentation based study of portland cement paste [25, 27, 29, 30, 34-36, 62-65]. Ulm et al. assert that the source of the distribution of measured mechanical properties could be attributed to distinct levels of packing density within the C-S-H. Lura et al. suggest that there may be other explanations for the distribution including the inclusion of ostensibly stiffer nano-crystalline phases present in the C-S-H phase, all within the interaction volume of an individual indentation test [37, 66]. Both explanations are tractable and have basis in well established existing theories. The packing density explanation owes to the colloidal model for C-S-H first proposed by Powers [67] and then later developed by Jennings and coworkers [33, 35, 41, 68-70]. Similarly, crystalline hydration products have long been known to exist in hydrated portland cement [53] and the mechanical properties of the crystalline phases do differ from those of the C-S-H phase [71]. Chen et al. confirmed existence of nano-crystalline phases present within C-S-H that could influence nanoindentation results [25]. It should be noted that neither explanation necessarily excludes the other and that the debate on this topic has mainly centered on determining the most likely explanation for the mostly undisputed experimental results.

Atomic force microscopy based indentation can illuminate this discussion to some degree because the AFM probe interacts with a smaller volume of material than is typical of nanoindentation experiments. A reduction in interaction volume should reduce the effect of the porosity, causing the measured values to approach those of the

intrinsic C-S-H particles. The measurement of mechanical properties with AFM is not a new idea, but obtaining consistent, accurately calibrated properties from AFM based indentation experiments has proved difficult. Furthermore, since nanoindentation produces perfectly acceptable results for homogeneous materials, the added complexity of AFM based measurements makes AFM based indentation less appealing for large classes of materials. Nevertheless, given the heterogeneous structure of C-S-H on the micron to nanometer scale, useful and distinct information can be gained from AFM that is not garnered from nanoindentation.

AFM based characterization of portland cement paste has been initiated by various researchers. Mondal et al. performed nanoindentation experiments coupled spatially with AFM to correlate various results with particular morphological phases [16]. Similarly, Saez de Ibarra et al. used AFM and nanoindentation to characterize cement paste with carbon nanotube dispersions [15]. More recently, Kim et al. used atomic force acoustic microscopy to measure the elastic properties of portland cement paste [72]. None of these approaches use the AFM probe as one would use a nanoindenter to extract a force versus displacement curve to characterize the material elastic properties.

CHAPTER II

OBJECTIVES

The primary objectives of this study are to experimentally measure the instantaneous and time-dependent mechanical properties of portland cement paste with AFM on the sub-micron length scale and to differentiate these measured results from analogous results obtained from traditional nanoindentation on the micron length scale. This study will address the interpretation of AFM indentation data and provide insight into the application of various approaches for modeling AFM indentation.

To date the application of time-dependent nanoindentation to cementitious materials has been limited. This study aims to characterize the short-term time-dependent viscoelastic Young's modulus of C-S-H using nanoindentation. Various assumptions made while formulating a time-dependent indentation solution will also be analyzed and a generalized solution for time-dependent indentation response of a viscoelastic material to a step loading will be presented.

Additionally, the elastic properties of C-S-H will be experimentally measured on the tens-of-nanometers length scale with AFM and these measurements will be used to help illuminate the discussion surrounding the multimodal distribution of C-S-H mechanical properties measured with nanoindentation. The proposed mechanisms of time-dependent deformation within C-S-H will be reviewed and hypotheses will be made to explain the difference in measured viscoelastic compliance obtained with nanoindentation and with AFM.

Objective 1: Develop experimental characterization techniques

Elastic characterization

The technique of choice for interrogation of material properties at the micro to nano scale has been, and likely will continue to be, nanoindentation, although relatively few researchers have applied this technique to cement paste or concrete [15, 34, 36, 73-75] and all have been relatively recent. Nanoindentation involves the instrumented loading of a surface with a sharp probe while monitoring the applied force, F, and the displacement into the surface, δ. For an arbitrary material a conceptual force versus displacement curve can be found in Figure 1.

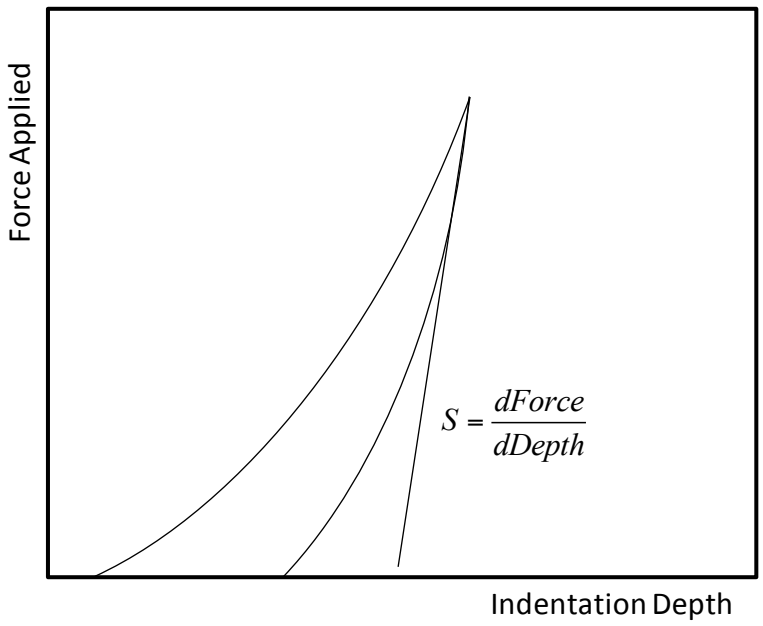

Figure 1: A conceptual force versus displacement curve for an arbitrary material where the slope, *S*, defines the stiffness or modulus of the material.

The probe is pushed into the material and is then retracted and the slope of the initial portion of the retraction curve is most closely tied to the elastic properties of the material since this response does not include plasticity.

For this study, portland cement paste will be indented with a traditional nanoindenter and with AFM to compare the indentation size effect. Though the same property is measured the results are not the same since the interaction volumes of the two different probes are quite a bit different. Figure 2 shows the relative difference in size for typical nanoindenter and AFM probe tips.

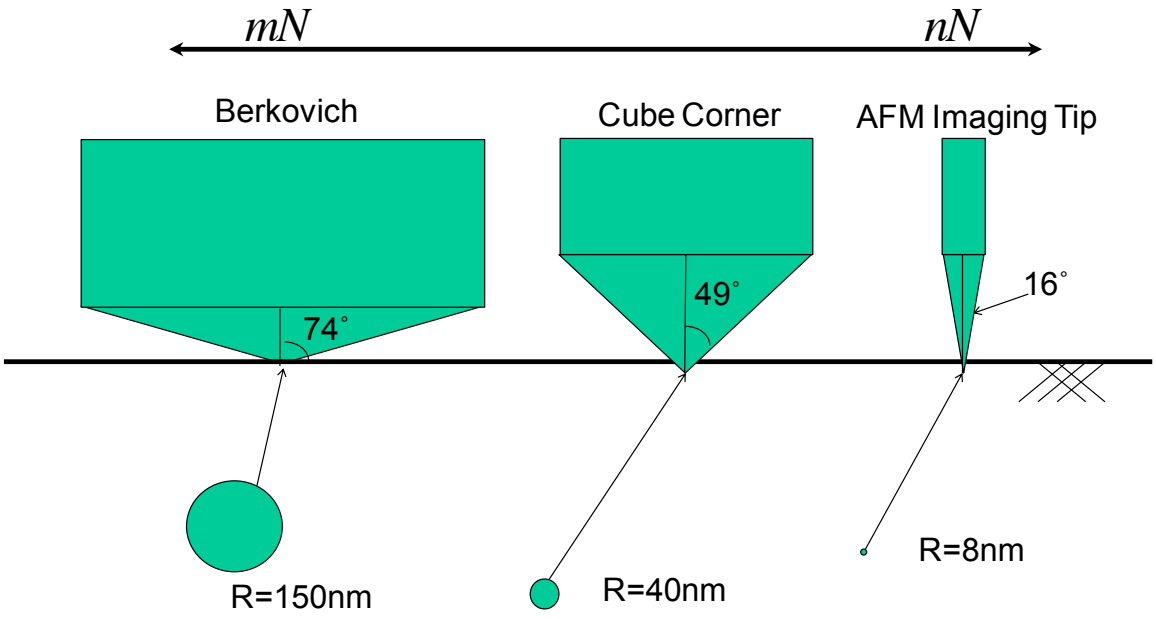

Figure 2: A schematic representation of the difference in probe size between typical nanoindentation probes and AFM probes.

The Berkovich tip, which was used for traditional nanoindentation testing in this study, has a typical tip radius of 150 nanometers while a typical AFM imaging tip is on the

order of eight nanometers. A cube corner tip which could potentially be used on either instrument has a typical tip radius of 40 nanometers. Furthermore, the tip angle should be considered. For the Berkovich tip with a typical half angle of 74°, the contact area and the interaction volume change very quickly with increased indentation depth. Conversely, tips with smaller half angles preserve a smaller indentation volume at deeper indentation depths compared to the Berkovich tip.

The elastic properties of C-S-H will be experimentally measured on the tens-of-nanometers length scale with AFM and these measurements will be used to help illuminate the discussion surrounding the multi modal distribution of C-S-H mechanical properties measured with nanoindentation, which probes the hundreds to thousands of nanometers length scale.

Viscoelastic characterization

Though often treated strictly as an elastic material for design purposes, the mechanical properties of portland cement concrete are known to have a history effect or memory [42, 76, 77]. It is possible that a more complete understanding of the fundamental nature of the time dependent deformation mechanisms in the C-S-H phase of the cement paste could lead to processing, mixture, design, or placement techniques that could optimize the performance of portland cement concrete.

Analogous to the perception of concrete as a time-independent material, the nanoindentation technique has most often been used for determination of elastic properties; however, recently the technique has been applied to measure time-dependent

mechanical properties as well. Viscoelastic nanoindentation testing involves the instrumented loading of a surface with a sharp probe while monitoring the applied force as a function of time, $F(t)$, and the displacement into the surface as a function of time, $\delta(t)$. Viscoelastic experiments can be cast into general categories: creep tests (controlled force), relaxation tests (controlled displacement), mixed creep and relaxation, and oscillatory.

With the traditional nanoindenter, the force applied to the probe is easily controlled and the creep test is the most practical. With AFM, neither force nor displacement are totally controllable, and the analysis of the experiment becomes more complicated as it involves mixed creep and relaxation. In this study both traditional nanoindentation and AFM will be used to measure viscoelastic properties of the cement paste.

Objective 2: Describe and interpret the nanomechanical-behavior of cement paste

Interpret AFM and nanoindenter results

In general, the cement paste has higher elastic modulus and lower viscoelastic compliance when tested with AFM than with nanoindentation. This difference will be explained from a microstructural perspective, particularly the micro and nano porosity present in the C-S-H phase of the cement paste. The disparity in elastic results is somewhat obvious, but the difference in viscoelastic properties is less so. This study will address the interpretation of AFM indentation data and provide insight into the application of various approaches for modeling AFM indentation.

Compare results and draw conclusions regarding the nanometric structure

The reduced elastic modulus measured with nanoindentation versus AFM, coupled with the colloidal spheres model [31, 33, 41, 69, 70] for C-S-H microstructure implies that there may be two or more different packing densities of crystalline spheres within the C-S-H. In the context of coordination number, the individual spheres of C-S-H are more coordinated within the colloidal groups, than the colloidal groups are coordinated with one another. Figure 3 schematically shows the colloidal model for C-S-H in portland cement.

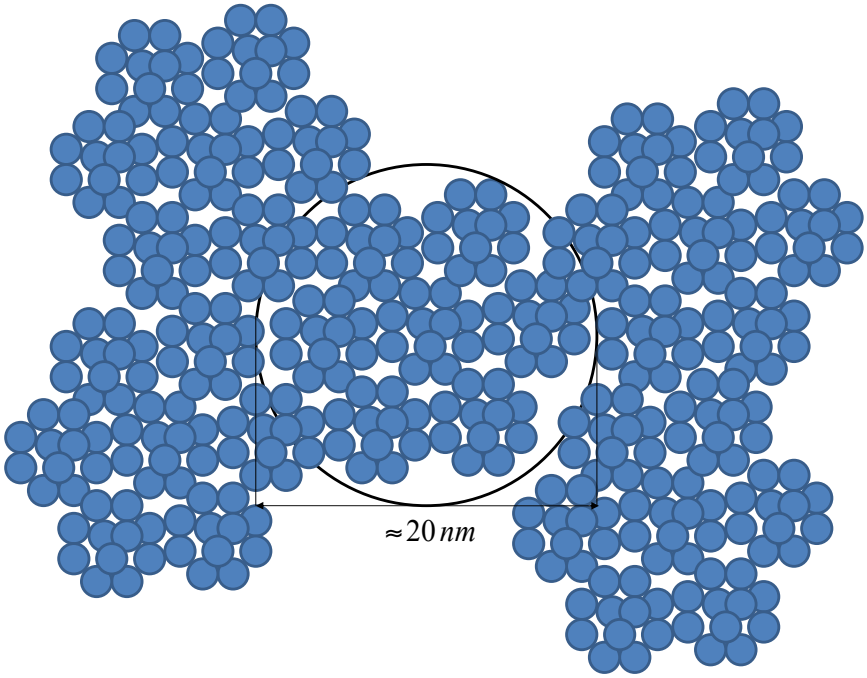

Figure 3: The colloidal model for C-S-H consists of multiple levels of agglomerated particles that are held together by some sort of Van der Waals type surface forces.

The colloidal spheres model for C-S-H provides a convenient explanation for the distribution of mechanical properties observed with nanoindentation, but this explanation should not be seen as causal. Other models exist for the structure of C-S-H such as the Feldman-Serada model [78, 79] and other theories exist to explain the modality observed in the results of nanoindentation testing [37, 66].

CHAPTER III

THEORY

This chapter will develop the theory that will be used to model the experimental results presented in Chapter V. The chapter will begin with a general introduction to contact mechanics: the description of how bodies deform against one another. The specific issues that manifest with small length scale and small load contact will be analyzed and evaluated. Finally, time dependent solutions for describing viscoelastic contact will be formulated.

Utilization of either a nanoindenter or atomic force microscope to extract mechanical properties necessitates employment of contact mechanics. The contact problem was first solved by Hertz [80] as a means of calculating the deflection of optical lenses when stacked against one another and, as a result, the Hertz solution describes the elastic contact of spherical bodies. More recently, Galin and Sneddon provided a contact solution for a cone with an elastic half space [81, 82]. Since the AFM and nanoindentation probes used in this study can be approximated as conical in shape, and are penetrated into the cement paste to a significant enough depth such that the sides of the probe dominate the contact area, the Galin-Sneddon solution provides a better starting point than the Hertz solution for this application. Indentation is also similar to the Boussinesq problem of a rigid foundation interacting with an elastic half space. The primary difference between the classic analytical contact theories is the geometry of the body interacting with the elastic half space. More recently, numerical approaches have

been proposed that avoid some of the simplifying assumptions present in each of the analytical theories.

Classic analytical

The two most common contact theories regularly in use are the Hertz and Sneddon theories and the major difference in these theories involves the assumed geometry of the contact, or for indentation, the assumed shape of the indenter being used to press into the material and the related pressure field in the contact area. In the case of Hertzian indentation, the indenter is a half sphere of radius R [80]. The central equation of the Hertz solution that relates indentation depth to load may be cast as

$$F = \frac{4}{3} M R^{1/2} \delta^{3/2}, \tag{1}$$

where F is the load applied to the spherical indenter, δ is the indentation depth, and M is the indentation modulus expressed as

$$\frac{1}{M} = \frac{1-\nu_{material}^2}{E_{material}} + \frac{1-\nu_{indenter}^2}{E_{indenter}}, \tag{2}$$

where E is the elastic Young's modulus, ν is the Poisson's ratio, and the subscripts denote whether the property is of the indenter or of the material being indented. For diamond indenters (E~1TPa), the second term in (2) is often negligible such that

$$M \approx \frac{E_{material}}{1-\nu_{material}^2} = \frac{E}{1-\nu^2}. \tag{3}$$

In traditional nanoindentation and with many AFM probes, pyramidal indenters are the norm and can be idealized as conical. The Galin-Sneddon solution is appropriate for these experiments and the solution for conical indentation can be cast as

$$F = \frac{2M\,Tan(\phi)}{\pi}\delta^2, \tag{4}$$

where ϕ is the half angle of the conical indenter probe [81, 82]. Equations (1) and (4) can be used to fit experimental force versus displacement data and determine M for the indented material.

Surface forces

Classical contact mechanics has adequately described the interaction and deformation between bodies in the cases of micro and nanoindentation for many years, but with the increase in popularity of AFM, new questions have been raised regarding the applicability of classical solutions to the AFM contact problem. Since the attractive forces measured with AFM are approximately the same order of magnitude as those applied to the AFM probe, ignoring adhesive surface forces may result in significant error. Figure 4 schematically shows a generalized contact scenario and a generalized indentation scenario. For two axi-symmetric bodies or for an axi-symmetric indenter and a flat surface, the separation between the bodies h varies as a function of the radial coordinate r. For most materials, the combination of varied surface separation as a function of position and general surface physics causes the indenter probe to experience both attractive and repulsive forces while in contact.

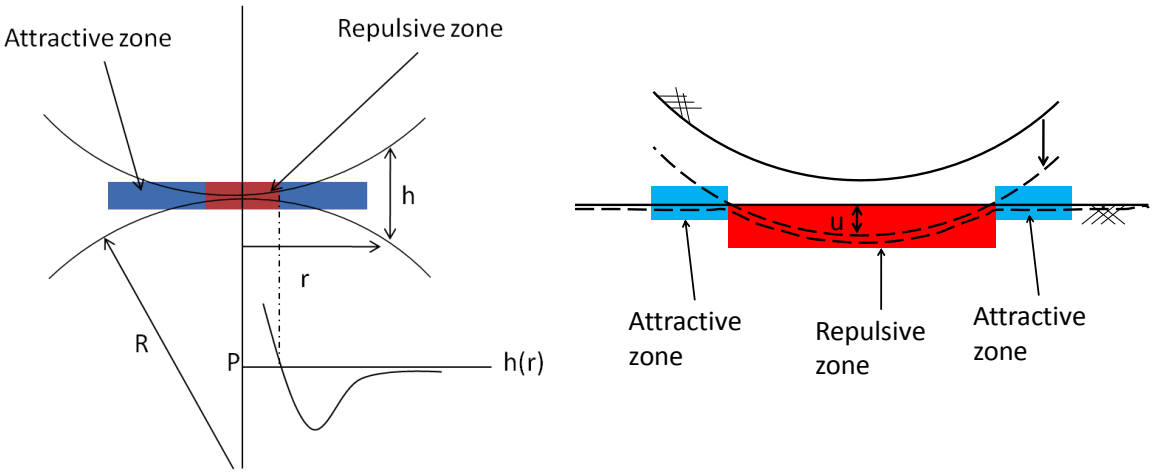

Figure 4: A) As two arbitrary bodies come into contact, separation dependent surface forces (assumed to obey a Lennard-Jones form) dictate that there must be a region of repulsive action and an attractive region. The forces are a function of separation between the bodies which is in turn a function of radial position for curved bodies. B) In the case of indentation, the force applied to the indenter body deforms the material being indented and the area of repulsive surface forces grows as the contact area increases while the attractive zone remains roughly constant.

While separation dependent surface forces do exist in micro and nanoindentation experiments, generally the load applied to the indenter tip is so much larger than the contribution of the adhesive surface forces, that the surface forces can simply be neglected. The bodies experience various surface forces which in aggregate can often be adequately described by the empirical Lennard-Jones potential function [83].

The Lennard-Jones model proposes that the two bodies in question experience negligible surface forces at large separations, attractive surface forces at intermediate

separations, and repulsive surface forces at very small separations (what would generally be known as “in contact”). The Lennard Jones equation can be cast as

$$p_s(h) = \frac{A}{6\pi h^3}\left[\left(\frac{z_0}{h}\right)^{12} - \left(\frac{z_0}{h}\right)^{6}\right], \tag{5}$$

where $p_s(h)$ is the pressure profile between the two bodies as a function of surface separation h, z_0 is the equilibrium separation distance, and A is Hamaker’s Constant, which can be related to the interfacial surface energy of the interacting bodies according to

$$\gamma = \frac{A}{16\pi z_0^2}. \tag{6}$$

For the purposes of this study, γ is not precisely the intrinsic interfacial surface energy of the interacting indenter and substrate; rather, it is a sum of surface energy, meniscus forces, and electro-chemical forces. The Lennard-Jones expression has the advantage of describing both the attractive and repulsive phenomena known to exist in contact mechanics of most materials. For minimally adhesive materials, or for large indentation depths where the adhesive contribution to the total force is minimal compared to the repulsive contribution, a simpler Poisson-Boltzman repulsion form may be more appropriate [84]. The exponential repulsive form considered here is

$$p_s(h) = P_r e^{-\kappa h} + P_r\left(\frac{z_0}{h}\right)^{9}, \tag{7}$$

where P_r controls the magnitude of the pressure and κ and z_0 control the separation at which the interaction takes place. The term z_0 is taken to be small so that the second term in (7) dominates the pressure response at small separations and prevents negative values of h from being encountered in the simulation.

Two primary analytical theories exist that account for the influence of adhesive surface forces on the contact problem. The solution proposed by Johnson, Kendall, and Roberts (JKR) [85] accounts for adhesion within the area of contact while the solution proposed by Derjaguin, Muller, and Toporov (DMT) [86] considers adhesion outside the area of contact. Both the JKR and DMT theories account for the effect of adhesive surface forces but both do so while making assumptions about the region of contact and the pressure profile between the interacting bodies. Furthermore, both theories are applicable to spherical contact which does not generally extend well to conical indenters. Also, neither theory describes the interaction between bodies in the pre-contact regime.

Geometry

All of the analytical contact theories make assumptions regarding the geometry of the bodies that are in contact with one another. As mentioned previously, the Hertz theory assumes contact of spherical bodies while the Sneddon theory represented in (4) assumes the contact between a cone and a flat half space. In general, true indentation probes are neither simply conical nor spherical. Figure 5 schematically demonstrates how a realistic AFM or nanoindentation probe might look.

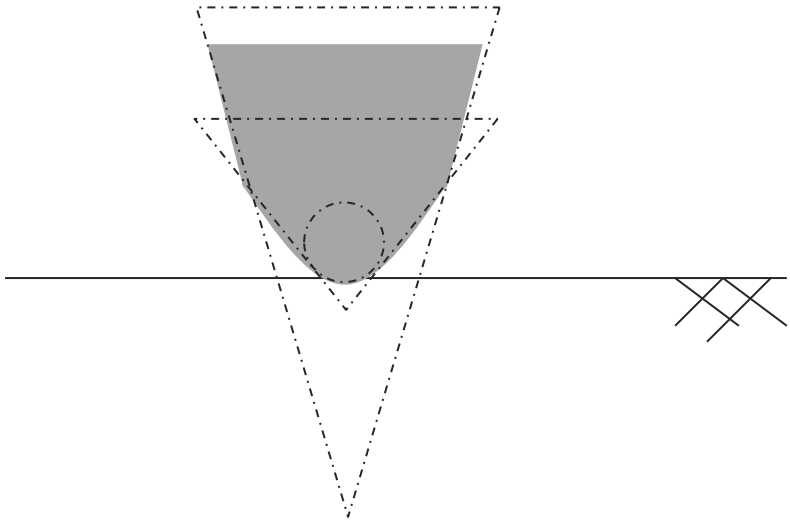

Figure 5: A realistic indentation probe could be considered conical or spherical depending on the depth of the indentation. The potential assumed geometries are shown by the dashed lines.

With respect to the assumption of a particular geometry, the researcher would need to know how deep the probe penetrates the material. In practice, this determination is fairly straight forward, particularly for the nanoindenter which presses very far into the material. However, for the AFM based indentation tests with very low applied forces, the indentation depth of the real probe may make this determination ambiguous.

Numerical

A few numerical solution approaches have been formulated for modeling contact problems. The solution proposed by Paul and Hashemi focused on accounting for non spherical geometries often encountered in real engineering problems and was solved by assuming positive pressure within the "contact area" and zero pressure outside [87, 88]. Another method proposed by Kalker involves minimizing elastic strain energy by

iterating pressure and deformation profiles and also assumes no interaction outside the contact area [89]. A more recent numerical solution method was proposed by Attard that makes fewer assumptions and is therefore considered to be potentially more accurate [90-94]. Attard's method assumes that small deformation elasticity applies, and that all displacements occur in the vertical direction.

Attard's self-consistent method

Attard's self-consistent approach involves modeling the surface forces such that their affect on the indenter pressure profile is separation distance dependent [90, 91]. In other words, the axisymmetric pressure profile between the indenter and the material being investigated is

$$p_s(r) = p_s(h(r)), \tag{8}$$

where p_s is the surface force profile and $h(r)$ is the separation between the surfaces at a radial coordinate r. Furthermore, the separation of the surfaces can be determined by subtracting the surface displacement $u(r)$ from the separation expected if the motion were considered rigid, such that

$$h(r) = h_0(r) - u(r), \tag{9}$$

where $h_0(r)$ is the rigid separation (negative indicating interpenetration of the original undeformed surfaces) for the two surfaces. The surface displacement may be expressed as

$$u(r) = \frac{-1}{\pi M}\int \frac{p_s\left(h(s)\right)}{|r-s|}ds \quad , \tag{10}$$

where ds is the element of the area over which the integration takes place, and s is simply a spatial variable in the plane that bisects the axis of contact.

The self-consistent approach conceptually mimics a displacement controlled indentation experiment. The method begins with the indenter and the material far apart such that no surface force is expected. In this initial state it is assumed that

$$\begin{aligned} u(r) &= 0 \\ h(r) &= h_0(r) \end{aligned} \quad . \tag{11}$$

Then, the indenter makes one small step toward the material such that the new $h_{0new} = h_{0old} +$, where Δ is small (on the order of 10^{-10} to 10^{-11} meters). With a new h_0, a new displacement, $u(r)$, is *guessed* according to,

$$u(r)_{guess} = h_0(r)_{new} - h(r)_{old}. \tag{12}$$

With the guessed displacement, a new separation, $h(r)$, can be calculated with (9) and a new pressure profile can be calculated with (8) and either (5) or (7). With a new pressure profile, a new displacement, $u(r)$, can be *calculated*. This calculated displacement profile is then blended with the guessed displacement from (12) at a prescribed mixing ratio to create a new "guessed" displacement profile and the loop is started a new. For each h_0 step, this loop will continue until the difference between the newly calculated displacement profile and the previously guessed displacement profile

differ by a small amount, 1×10^{-12} m in this case. Once the error in the deformation is minimized, a new h_0 step is made and the process is repeated for each h_0 step. This process is illustrated in Figure 6 in flow chart form.

The self-consistent numerical method yields many advantages and some disadvantages over analytical solutions. First, $h(r)$, $u(r)$, and $p(h(r))$ are determined (and recorded) at every step, in addition to simply recording the force. Recording these quantities yields a wealth of information that is not available in the analytical solutions. However, the major problem with this method is the computational expense required to arrive at a solution. Since each incremental step must be iterated to find the correct displacement and separation, the process can be computationally expensive. Additionally, the value of Hamaker's constant is generally not known a priori for most materials. Drawbacks aside, the Attard method of modeling the contact between two bodies is the most general approach currently in use.

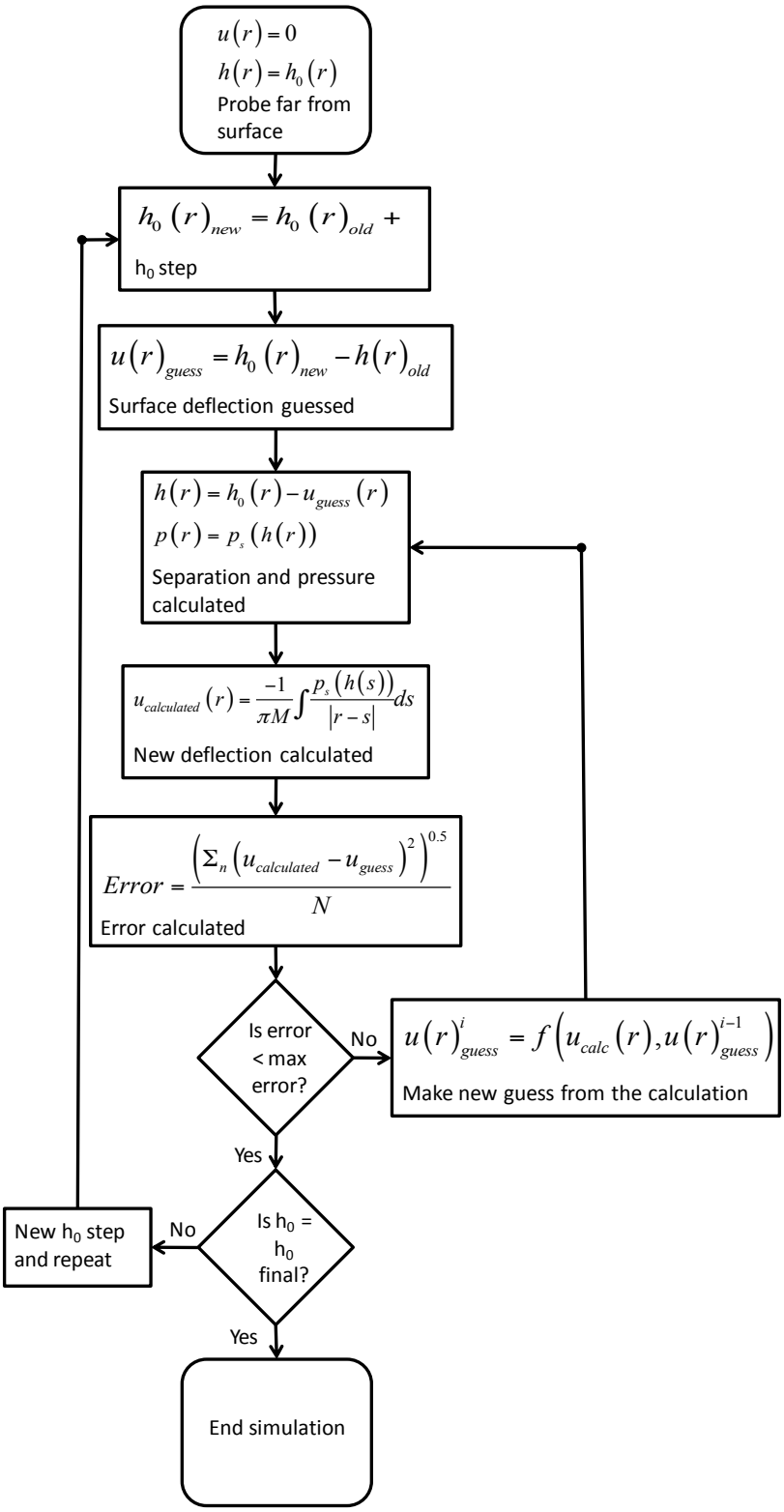

Figure 6: A flow chart representing the self-consistent method [90] shows the equations and the routine for simulating an indentation experiment.

Advantages of the self-consistent method

As alluded to above, the self-consistent method has two primary practical advantages compared to traditional analytical techniques. First, given the generalization of the self-consistent method by Graham et al. [17], realistic tip geometries can be considered for any axi-symmetric indenter shape. Second, realistic surface forces and their related pressure profiles can be considered. Figure 7 shows a simulated indenter probe with a 40 nm tip radius and an included cone half angle of 48.5°, which represents a typical cube corner indentation probe.

The benefits of accurately accounting for the actual tip geometry in an indentation experiment depends on the particular experimental conditions, specifically, the indentation depth compared to the characteristic geometry of a particular tip. For example, if a spherical indenter is displaced to a depth much less than the radius of the spherical tip, then the geometric assumptions of the Hertz solution are perfectly acceptable [95, 96]. Similarly, if a cono-spherical tip is indented such that the depth of penetration is much greater than the radius of the conical tip, then the geometric assumptions of the Sneddon solution are suitable [97]. The advantage of the self-consistent method is that the geometry of the contact is accounted for at any indentation depth.

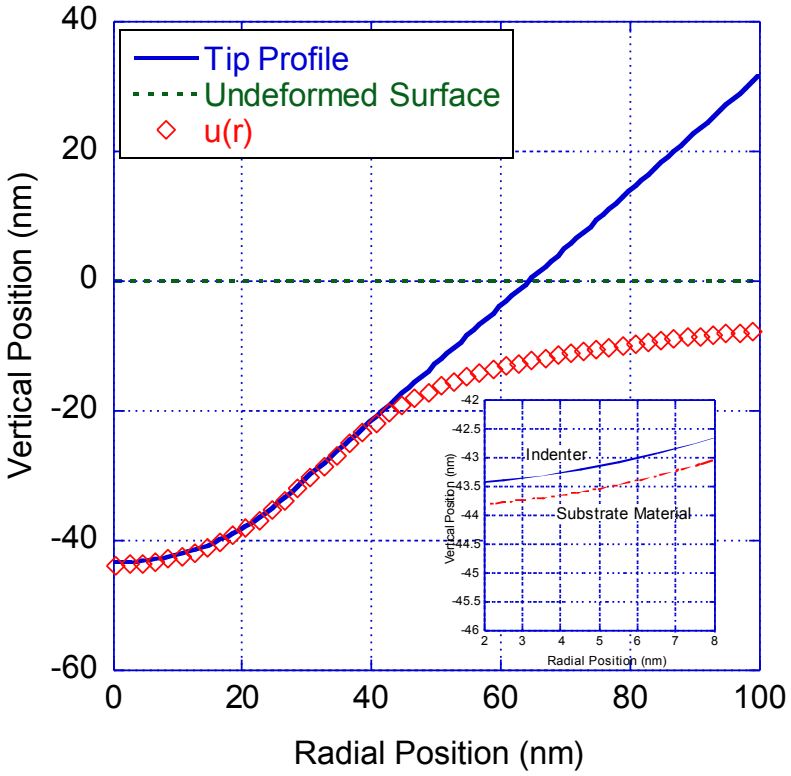

Figure 7: The idealized cono-spherical tip geometry representing a diamond cube corner probe at $h_0 = 42\,\text{nm}$ generated with the self-consistent solution. The inset shows that the surfaces never "touch" with realistic separation dependent surface forces.

With AFM based indentation, one approach has been to use relatively large spherical probes with low applied forces in an effort to meet the conditions of the Hertz solution [94]. This approach unfortunately neutralizes one of the great advantages of AFM, which is the extremely small tip dimensions available and the potential for measuring properties of adjacent dissimilar materials. By accurately accounting for the tip geometry of sharp AFM probes, one retains the ability to extract accurate material properties from very small areas of a material sample. For large classes of materials such as composites and naturally heterogeneous materials like portland cement paste, the

material properties can vary on short length scales of the same relative magnitude as the tip dimensions.

The second major advantage of the self-consistent approach is the flexibility in the pressure profile between the indenter and the material. For the Boussinseq problem to be analytically solved, a mathematical form of a pressure profile must be assumed. For example, in the case of the Hertz solution, the pressure is of the form of an ellipse such that,

$$p(r) = P_0\left(1 - \frac{r^2}{a^2}\right)^{1/2}, \tag{13}$$

where P_0 is the maximum pressure and a is the radius of the circular "contact area". The first major advantage of accurate geometric accounting is also related to the second major advantage through the concept of contact area in the analytical expression of $p(r)$ given in (13). As is expected from an understanding of realistic surface forces, the two surfaces in contact never actually "touch."[1]

[1] In continuum mechanics, the idea of "contact" is ambiguous since bodies are assumed to be comprised of points having no dimension, but no two points are allowed to coexist in the same space.

This separation between the two surfaces, even at positive applied force levels, is preserved in the self-consistent solution and is shown in the inset in Figure 7. Since the self-consistent method only predefines the pressure-separation relationship, this allows for a more general $p\left(h\left(r\right)\right)$ and, as a result, a more general solution to the contact problem.

Figure 8 shows the calculated pressure profiles at multiple indentation depths determined from a simulated experiment with a typical silicon AFM imaging probe and portland cement paste. It is interesting to note that as the indentation depth increases, the shape of the pressure profile changes to match the shape of the indenter, since the repulsive contribution dominates the $p\left(h\left(r\right)\right)$ response. Also plotted in Figure 8 is (13) plotted at the same indentation depths with a assumed to equal the r position corresponding to the inflection point of the numerically generated pressure profile. The particular P_0 value chosen for the solid curves in Figure 8 were determined by matching the total force applied to the indenter probe. Since the Hertz solution does not account for adhesive surface pressure clearly shown, the peak repulsive pressure in the Hertzian case is lower than that generated by the self-consistent solution.

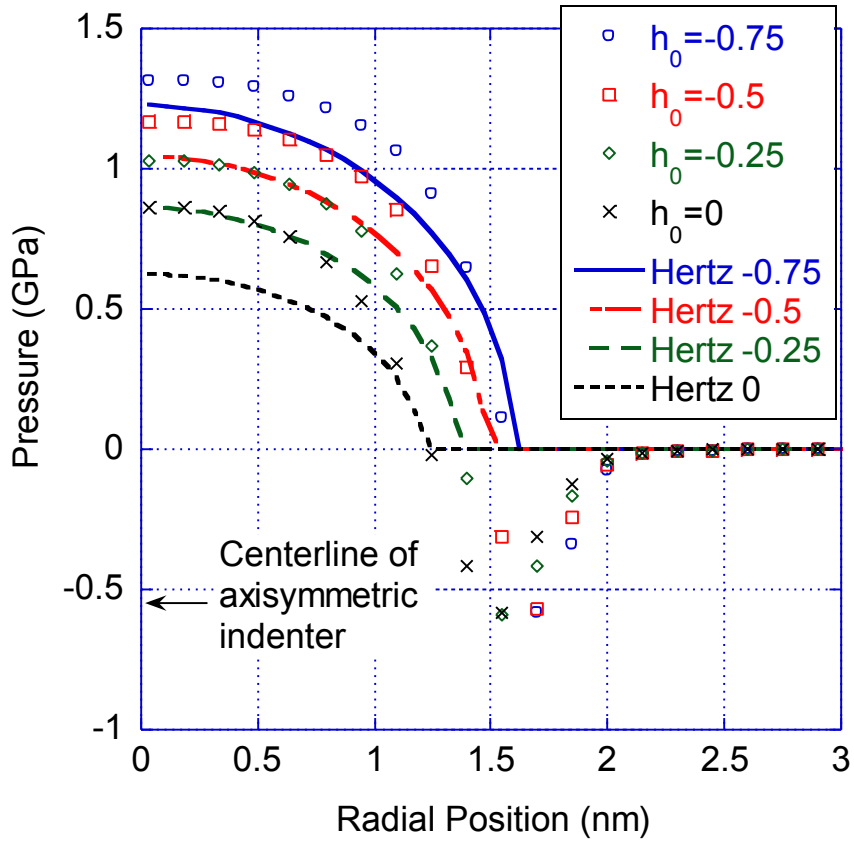

Figure 8: The simulated pressure profiles for an AFM probe with tip radius 2 nm at several indentation depths show the ability of the self-consistent solution to capture both repulsive and adhesive effects. Also plotted are the Hertzian pressure profiles for the same indentation depths. Notice that because the Hertz solution neglects the adhesion outside the area of contact, the overall magnitude of the pressure profile is reduced to achieve an equivalent total applied force.

Applicability of the self-consistent method

Given the computational expense needed to implement the self consistent method, particularly when compared with the relative simplicity of analytical solutions, one naturally questions when the extra effort is necessary. This subsection aims to identify conditions where the self consistent method of modeling AFM contact provides tangible benefit over analytical solutions.

As alluded to in the previous sections, the applicability of an analytical solution may depend on the particular experimental conditions, or conversely, the necessity of the more cumbersome self-consistent solution may depend on specific experimental conditions. With this in mind, several AFM indentation tests are modeled with both analytical solutions and the self-consistent method. First, Figure 9 shows a typical force (F) vs h_0 data from an AFM indentation test fitted with Hertz, Sneddon, and self-consistent models. These data were obtained with a diamond cube corner tip with an effective tip radius of $40\,\mathrm{nm}$. The loads applied to the tip in this case are in the range of $\mu\mathrm{N}$, which is roughly comparable to very low nanoindentation loads.

Best fit values for the Hertz and Sneddon solutions for the fit parameter M were coincidentally both found to be $42\,\mathrm{GPa}$ while the self consistent solution yielded $45\,\mathrm{GPa}$. Figure 9 shows that for this experiment, the self-consistent model does not provide a substantially better description of the experiment than the analytical solutions.

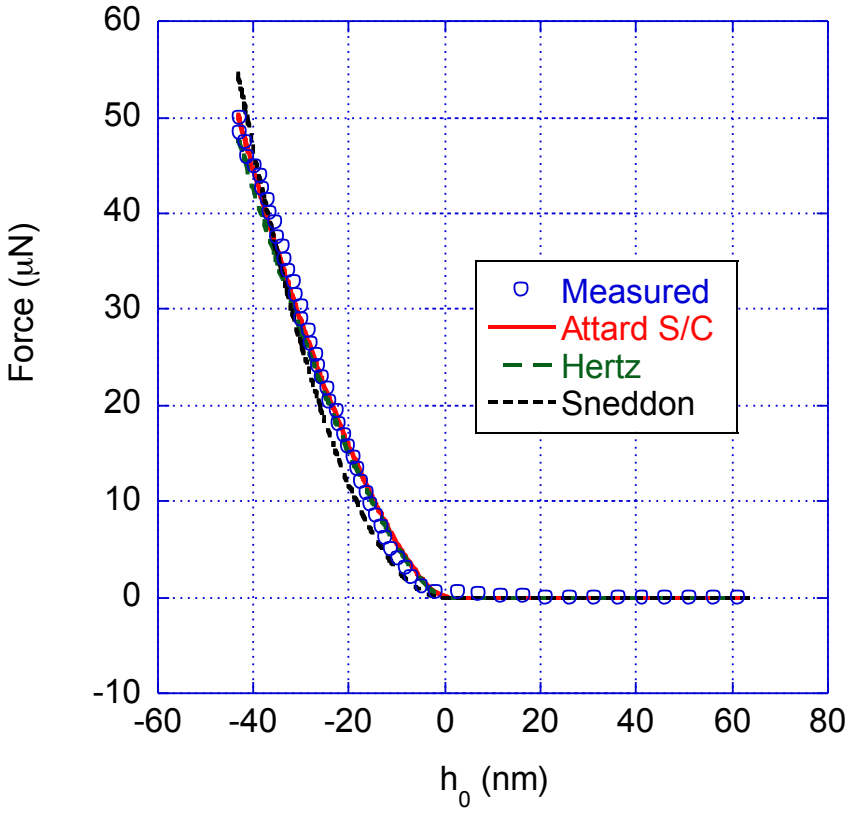

Figure 9: AFM based indentation data for cement paste indented with a diamond cube corner probe are fitted with the self-consistent, Hertz, and Sneddon solutions. The data shown are obtained from the retraction of the probe from the hydrated cement surface to minimize incorporation of plasticity. The Hertz and self-consistent solutions are virtually identical for $h_0 < 0$.

The results in Figure 9 should not be generalized, however, as the applicability of the self-consistent routine is highly dependent on the experimental conditions. Figure 10 shows a typical indentation test performed on cement paste with a very small probe and a very shallow indentation depth. For these data, the probe has a tip radius of approximately 2 nm and the maximum force is in the tenths of nanonewtons.

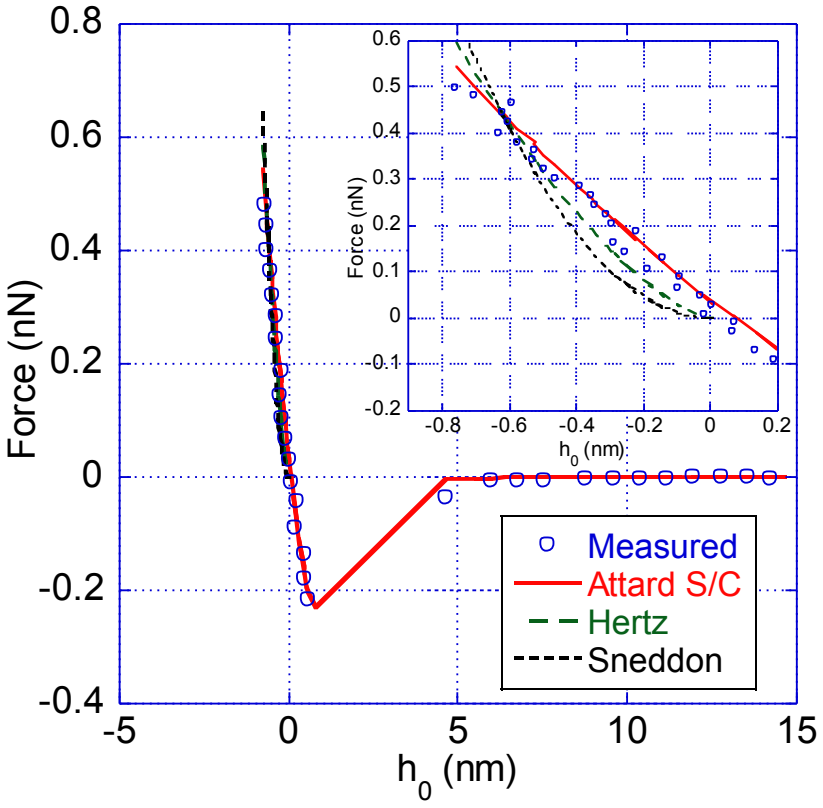

Figure 10: Typical low force elastic indentation data obtained with a typical AFM imaging probe with tip radius $\approx 3\,\mathrm{nm}$ for very shallow indentation depth indicates the ability of the self-consistent solution to model the pre-contact behavior readily observed in AFM experiments. The inset shows the typical contact (e.g. $h_0 < 0$) regime that highlights the difference between self-consistent and analytical models.

The most noticeable improvement that the self-consistent approach gains over the analytical solutions is the description of the pre-contact behavior. The inset in Figure 10 highlights the traditional contact region (i.e. $h_0 < 0$). Since the analytical contact theories are only defined in the repulsive contact regime, the pre-repulsive (adhesive force) region is not described in either the Hertz or the Sneddon theories. Furthermore in terms of fitted elastic indentation modulus, there is great disagreement between the

models. The self-consistent model data shown in Figure 10 was generated with $M = 5$ GPa, while the Hertz and Sneddon solutions yielded $M = 0.95$ GPa and $M = 10$ GPa, respectively, as best fit modulus values. Since neither analytical solution accounts for the relatively large affect of surface forces in this test, the error introduced by modeling with the analytical solutions is significant.

Two cases have been shown where AFM obtained indentation data has been fitted with Attard's self-consistent solution and with traditional analytical solutions. For the data shown in Figure 9, the benefit of using the self-consistent solution to model the experimental data is negligible, while for the data in Figure 10 the self-consistent method is all but required. This section will conclude with an analysis of the relative accuracy of the analytical solutions versus the self-consistent method. A simple dimensionless parameter, θ, by which various test conditions can be compared was proposed by Fuller and Tabor [98, 99] and will be modified very slightly here. This parameter can simply be thought of as the force required to displace a given indenter to some depth in the material compared to the maximum adhesive pull off force exerted between that indenter and the material being tested, such that,

$$\theta = \frac{F_{indentation-peak}}{F_{attraction-peak}}. \tag{14}$$

Specifically, the terms in (14) can be substituted with (1) or (4) in the numerator, depending on the maximum indentation depth and the geometry of the tip used, while the denominator can be defined as

$$F_{attraction} = 4\gamma\pi R, \tag{15}$$

where for this case, R is the radius of the spherical indenter tip or the radius of the tip of the conical-spherical indenter tip. Eq. (15) may be recognized as the adhesive pull off force term defined in [86]. For Hertzian indentation where the geometry is spherical or where the indentation is spherically dominated

$$\theta = \frac{M\delta_{\max}{}^{3/2}}{3\gamma R^{1/2}}, \tag{16}$$

and for Sneddon indentation where the indentation geometry is conically dominated

$$\theta = \frac{\delta_{\max}{}^{2} M\, Tan(\phi)}{2\pi R\gamma}. \tag{17}$$

As a way of characterizing the error one might encounter from applying an analytical solution versus the self-consistent numerical solution, one may define,

$$Error\% = \frac{\left|M_{fitted} - M_{simulation}\right|}{M_{simulation}} \times 100. \tag{18}$$

Figure 11 represents the error in fitted M (determined via analytical solutions) compared to the same value from Attard's self-consistent numerical solution ($M_{simulation}$). The data points in this figure were created by generating combinations of $M, \delta_{Max}, R,$ and γ that resulted in θ values that were spaced over a large range. Next, the self-consistent solution method was used to simulate indentation experiments with these combinations of input parameters and the force versus displacement data were exported and fitted with the Hertz, JKR, and DMT solutions to determine M_{fitted} using a nonlinear

optimization routine in Mathematica. Finally the error for a given θ was computed with (18).

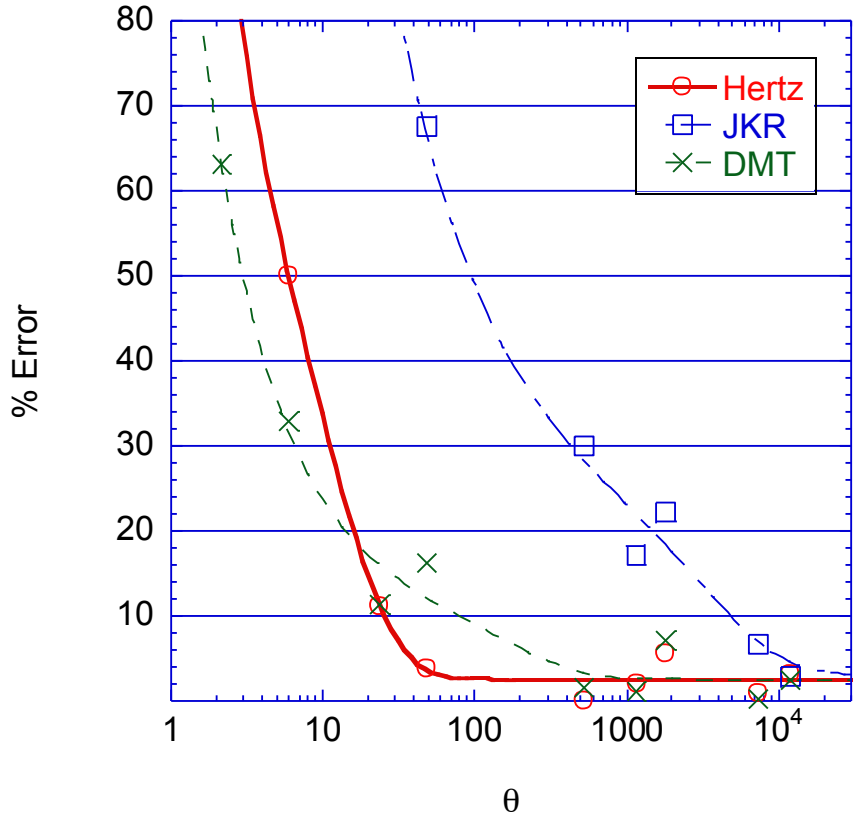

Figure 11: As θ decreases, the error introduced by using the analytical solutions rapidly increases. Since some of the parameters that define θ are experimentally controllable, AFM based indentation experiments can be designed such that minimal error is introduced by modeling with analytical solutions.

Figure 11 shows that for high values of θ, the error introduced by modeling indentation experiments with analytical solutions is minimal, while as θ decreases the error increases rapidly. This is an important fact to note because the maximum indentation depth and the tip geometry can be selected when designing the experiment.

It is also interesting to note that for these simulated indentation tests, neither the JKR nor the DMT theories produce tangible benefit compared to the Hertz theory, though for traditional contact mechanics applications such as determining the contact area between bodies, the JKR and DMT theories may provide more benefit. In general, for $\delta = 0$, both the JKR and DMT theories over predict the adhesive force compared to the self-consistent simulation. For experimental conditions where θ must be small such as very shallow indentation depth or very low modulus-high surface energy materials, numerical modeling such as the Attard self-consistent method should be employed to achieve accurate results.

Viscoelastic theory

A common method for deriving solutions to boundary value problems involving viscoelastic materials involves the elastic-viscoelastic correspondence principle in which field variables and constitutive properties in an elastic solution are replaced by the corresponding Laplace (or Fourier) transformed viscoelastic analogs, solved in the transform domain, and then inverted back to the time domain. Unfortunately, the correspondence principle generally precludes problems that involve time-dependent transition from traction boundary conditions to displacement boundary conditions (or vice versa) on the boundary of the bodies involved. However, Lee and Radok [100, 101] showed that transforms could be applied and accurate solutions obtained so long as the contact area between an indenter and the material being indented was monotonically increasing with time. In other words, for indenters of increasing cross section with

increasing contact depth, the correspondence principle could be used so long as the indenter probe was moving into the material, but not for the retraction. This method was used by Vandamme and Ulm [54] to create closed-form solutions for the indentation problem and apply their solution to indentation tests of cement paste.

Background theory

The elastic solution for indentation of an isotropic solid considered in this analysis is the widely known Galin-Sneddon solution [81, 82],

$$\delta^2(t) = \frac{\pi}{2\tan\phi}\frac{F(t)}{M}, \tag{19}$$

where $\delta(t)$ is the indentation depth as a function of time, θ is the half-angle of the conical indenter tip, $F(t)$ is the load as a function of time, and M is the indentation modulus defined in (2) and (3). Applying common intermoduli relations to (3) quickly show the result from equation 10 of [54],

$$M = 4G\frac{3K+G}{3K+4G}, \tag{20}$$

where G is the shear modulus, and K is the bulk modulus of the body being indented.

Application of the correspondence principle

To apply (19) to the problem of creep indentation, all time-dependent parameters must be transformed to remove the time dependence. Once the relevant transformed parameters are obtained, the solution can be formed in the transform domain, and then

this solution can be inverted back to the time domain. Substituting transformed parameters into (19) yields

$$\overline{\delta^2(s)} = \frac{\pi}{2\tan\phi}\frac{\overline{F(s)}}{s\overline{M(s)}}, \tag{21}$$

where the overbars denote the Laplace transformed quantity and s is the Laplace transform variable. Since an approximated step loading is applied in these experiments,

$$F(t) = F_{max}H(t), \tag{22}$$

where $F_{\max}$ is the peak applied load and $H(t)$ is the Heaviside function. The Laplace transform of (22) is

$$\overline{F(s)} = \frac{F_{max}}{s} \tag{23}$$

and the Laplace transform of (3) is

$$s\overline{M(s)} = \frac{s\overline{E(s)}}{1-(s\overline{\nu(s)})^2}, \tag{24}$$

where the s-multiplication is necessary because of the differential operation in the Laplace transformed constitutive equation of a linear viscoelastic material. The viscoelastic compliance $J(t)$ is related to the viscoelastic Young's modulus $E(t)$ in the transform domain as

$$\overline{E(s)} = \frac{1}{s^2\overline{J(s)}}. \tag{25}$$

Depending on the particular forms selected for $J(t)$ and $\nu(t)$ (or $K(t)$ and $G(t)$) the solution to the problem may not be analytically invertible into the time domain and a numerical inversion routine may be appropriate.

Approximating constant *K* or constant *v*

The derivation presented in [54] holds K as constant (time-independent) and thereby assumes that the only time-dependent deformation is deviatoric. The indentation "creep modulus" reported in [55] is not utilized to determine traditional viscoelastic moduli, and thus the issue of approximating a constant K or ν is not broached. If $K(t)$ is approximated as constant, common intermoduli relations (applied in the transform domain) show that $\nu(t)$ must be an increasing function of time. The approximation of a constant value for $K(t)$ has precedent [102, 103] since for most solid materials $G(t)$ relaxes faster than $K(t)$. Figure 12 shows the normalized bulk and shear modulus plotted with $\nu(t)$ for the case of constant $K(t)$.

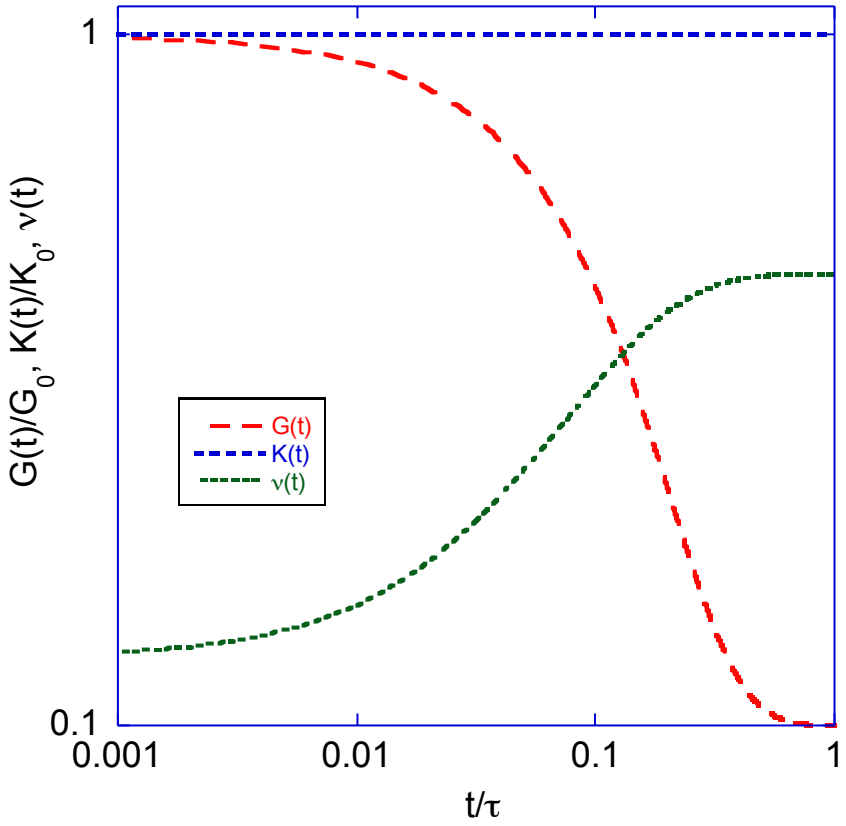

Figure 12: For a constant bulk modulus, common intermoduli relationships dictate that if the shear modulus decreases with time, the viscoelastic Poisson's ratio must increase.

For cementitious materials the literature seems to suggest that $\nu(t)$ may be approximated as time independent [104-108] and $K(t)$ allowed to change with time, although a study by Bernard and Ulm [109] indicates an increasing $\nu(t)$ (constant $K(t)$) after longer loading times. The question of time independent ν seems to revolve around whether the material tested is behaving as a true isotropic solid or as a porous body [42]. No matter the externally applied traction on the boundary of a porous body, the internal state of stress in the solid phase is always mixed deviatoric and dilatational.

Thus, we expect the relaxation rates of a highly porous body to be the same under applied hydrostatic or deviatoric stresses. With a nanoindenter, the interaction volume of the cement paste tested is conservatively on the order of single digit cubic microns [25] and cement paste is known to contain substantial porosity in the nanometer range [32]. This nano-porosity contributes to a mixed stress state in the solid colloidal C-S-H particles, supporting the approximation of a time independent $\nu(t)$, at least for short-term creep tests.

As will be shown in the results section, the average measured elastic Young's modulus in the nanoindentation tests was $E = 21.6$ GPa. An assumed constant $\nu = 0.25$ combined with common intermoduli relations would suggest that $K = 7.57$ GPa. Based on [110, 111], this calculated K agrees with that measured for the porous body of a typical hardened cement paste, not the bulk modulus of the solid phase (K_s), which is on the order of 45 GPa. The fact that the K calculated from the indentation experiments agrees with the value of K for a typical porous body of hardened cement paste suggests that the pore volume fraction in the indentation interaction volume is similar to the pore volume fraction in a bulk sample of hardened cement paste. Indeed, Vandamme and Ulm suggest C-S-H porosities ranging from 17-34%, depending on packing density of the particles [55]. Additional motivation for holding $\nu(t)$ constant is the insensitivity of the indentation modulus M to changes in ν.

Vandamme and Ulm [55] suggest that the C-S-H creep mechanism is primarily nano-particle sliding. According to this proposed mechanism, an applied hydrostatic stress on a C-S-H colloidal mass results initially in a mixed dilatational and deviatoric

stress state, but as deformation increases with time the packing density also increases. The result would be a gradual shift to purely dilatational stress state, and thus a purely dilatational response. As such, at later ages $\nu(t)$ will likely become an increasing function of time as the porosity of the material is reduced.

Because the durations of the creep tests performed in this research were short, in the analysis in this paper $\nu(t)$ will be held constant ($\nu = 0.25$) such that the Laplace transform of $\nu(t)$ is simply

$$\overline{\nu(s)} = \frac{0.25}{s}. \tag{26}$$

With the approximation that $\nu(t) = \nu(t = 0) = 0.25$, (21) can be fully defined in the transform domain and then inverted back to the time domain to give

$$h(t) = 1.21\sqrt{F_{max}\left(J(t)\right)Cot\phi}\,. \tag{27}$$

Eq. (27) will be used to fit the experimental data in subsequent sections.

Atomic force microscopy creep indentation

The modeling of the AFM based creep indentation experiment can be handled with a similar analytical approach as that presented above. The contact need not require numerical modeling. Furthermore, as discussed above the error introduced by analytical modeling of AFM indentation can be minimized by careful selection of experimental parameters as they affect the dimensionless θ parameter from (16) or (17). For these experiments, the load levels and indentation depths do not necessitate the use of numerical modeling ($\theta \approx 10,000$).

As discussed above, the elastic-viscoelastic correspondence principle is a common and popular method of obtaining viscoelastic solutions for engineering problems where a suitable elastic solution already exists. Unfortunately, for these particular experiments the load function $F(t)$ is not of the form of a step load as was the case in [44]. Therefore, the inversion from the transform domain into the time domain cannot be performed analytically and a numerical inversion routine such as [112] must be employed. This does not present an insurmountable problem since the aforementioned inversion routine is quite accurate, but it does add complexity and computational expense to the modeling of these indentation experiments and the numerical inversion precludes acquiring a closed form analytical solution. Fortunately, (19) can be easily manipulated as,

$$h^2(t) = \frac{\left(1-\nu^2\right)}{2Tan\left(\phi\right)} F\left(t\right) J \quad , \tag{28}$$

where J is the uniaxial elastic compliance, or inverse of the elastic Young's modulus. In this research, ν will be approximated to be time-independent, however the time-dependence of ν deserves some discussion. In [44] it was argued that for a highly porous material, ν may be approximated closely as a time-independent value since the state of stress on the solid particles is always mixed deviatoric and dilatational stress regardless of the boundary conditions applied to the porous body. In the case of the AFM based indentation tests, it is perhaps not as clear that the interacted material is highly porous in nature; however with the interaction volume in these tests on the order of a few hundred cubic nanometers, the material is likely to contain a significant pore

volume fraction. In addition, based on the form of (2), small changes in ν do not significantly affect the model. If ν is assumed to be constant with respect to time [42, 44, 110], the fractional first term of (28) is entirely time-independent and the time-dependence relies only on the product of $F(t)$ and $J(t)$ (which now expresses the viscoelastic rather than the elastic uniaxial compliance). From this form, a viscoelastic solution can be obtained by applying the convolution integral technique to the product of $F(t)$ and $J(t)$ in (28) to produce,

$$h^2(t) = \frac{(1-\nu^2)}{2Tan(\phi)}\left[\int_0^t F(t-t')\dot{J}(t')dt'\right] \tag{29}$$

where $J(t)$ is the uniaxial viscoelastic compliance, $\dot{J}(t')$ is the first time derivative of $J(t)$, and t' is the dummy variable for time integration. Depending on the forms of $F(t)$ and $J(t)$, (29) may be analytically integrated to determine a closed form viscoelastic solution to the problem of viscoelastic indentation experiments. Forms for both $F(t)$ and $J(t)$ will be presented in subsequent sections.

CHAPTER IV

EXPERIMENTAL

In order to study the nanomechanical properties of portland cement paste, nano-scale experiments were performed on hardened portland cement paste samples, which were intended to be representative of realistic paste that might be encountered in construction materials. This chapter will summarize the experimental program of this research. Both the materials and the methods will be introduced and discussed. For this work, the primary instruments used were the nanoindenter and the atomic force microscope. In addition, a custom relative humidity control apparatus was fabricated and utilized. The results of the experimental program are modeled with various solutions from the previous chapter and these results are presented in the subsequent chapter and discussed in Chapter VI.

Materials

The specimens used in this study were cast from a typical Type I/II cement with a *w/c* of 0.4. The cement and water were mixed according to ASTM C305-99 and the resultant paste was placed into acrylic tubes with a square cross-section and an inner dimension of 1cm (0.394 in). On one end, an acrylic plate was affixed with a two-part epoxy. The length of the tubes was approximately 10 cm (3.94 in). The fresh paste filled molds were vibrated and vacuumed to remove any entrapped air. The specimens were then sealed and placed into a 98% relative humidity room at a temperature of 23° C

for 24 hrs. Once the initial curing had taken place, the specimens were carefully demolded and placed in lime water for approximately 90 days.

The cured "beams" were radially sliced across the long axis of the beam into 3 mm thick 1x1cm^2 plates using an Isomet precision wet saw. The slices were allowed to dry in the laboratory environment and were then affixed with cyanoacrylate glue to circular steel discs measuring 15 mm (0.591 in) in diameter. The exposed flat surface of the cement paste sample was polished using techniques similar to those presented in [113], with the addition of final polishing using diamond slurries in five steps with diamond particle sizes ranging from 6 μm to 0.25 μm. In these final steps the diamond slurry was placed on a glass plate and the specimen was manually oscillated against the glass. After each diamond slurry polishing step the specimen was wiped dry with denatured alcohol to remove any residue from the slurry.

Nanoindentation

In this study, a Hysitron Triboindenter model TI-900 was used for the creep indentation tests, which were conducted at room temperature ($\approx 23^\circ$ C) and relative humidity ($\approx 50\%$ RH). The indenter was fitted with a typical diamond Berkovich indenter tip. Figure 13: The nanoindenter used in this study was the Hysitron Triboindenter. This device is a flexible, stand-alone nanomechanical testing system and is widely considered the industry standard for nanoindentation testing.Figure 13 is a photograph of the actual nanoindenter used in this research. The control software for the

nanoindenter was capable of automation or scripting. This facilitated convenient sequencing of the longer creep indentation tests.

Figure 13: The nanoindenter used in this study was the Hysitron Triboindenter. This device is a flexible, stand-alone nanomechanical testing system and is widely considered the industry standard for nanoindentation testing.

For the creep loading, a trapezoidal shape load history was used in all cases which included a rapid load application phase with elapsed time t_l where the load was increased from $F = 0$ to $F = F_{\max}$, a load holding phase whose time was t_h, and an unloading phase whose time was t_u, where the load was reduced from $F = F_{\max}$ to $F = 0$. Since $t_h \gg t_l$, step loading was used as an approximation to simplify the

analysis. Figure 14 plots the generalized loading applied in the creep nanoindentation tests.

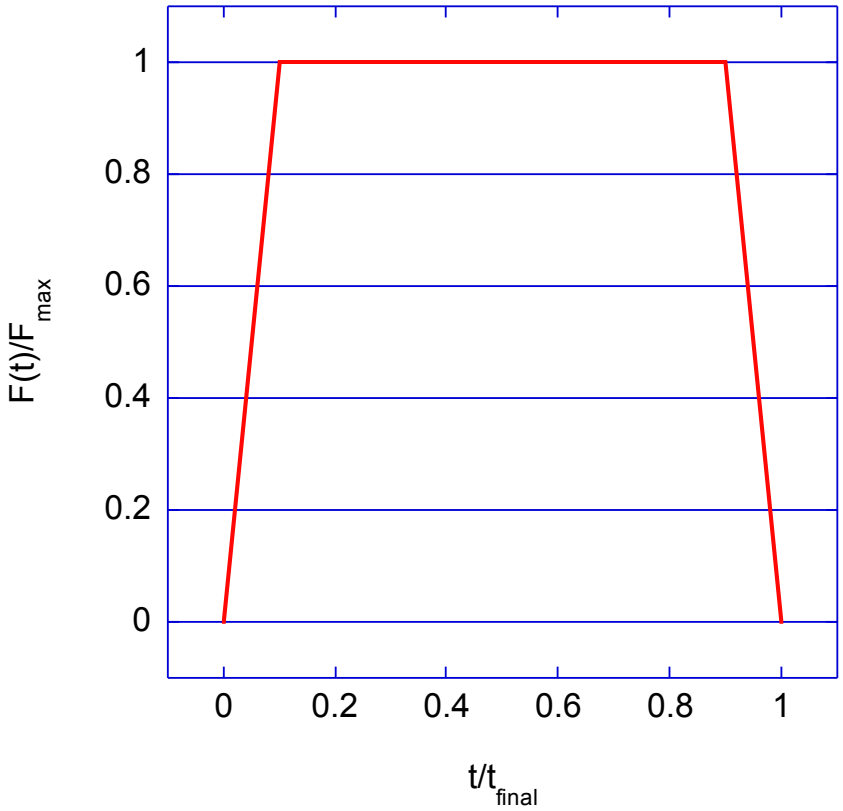

Figure 14: A schematic representation of the loading for the creep nanoindentation tests shows the rapid loading followed by a holding phase and finally the unloading of the material. The loading and unloading slopes are not realistic and are only intended to demonstrate that the load is applied and removed over a finite period of time.

Upon unloading, the penetration depth versus load was also monitored to determine the elastic properties for each test. The slope of the unloading curve was used in the Oliver and Pharr method [97] to determine the elastic indentation modulus.

The creep indentation tests performed in this study were all conducted at a single $F_{max} = 1500$ μN to minimize any variability arising from the testing procedure. Two different holding times were used to assess the response of the material over different time scales. A total of forty-eight tests were conducted for the 30 s holding time and eight tests were conducted for the 1 hr holding time. The results from four tests (of the forty-eight 30 s tests) were discarded; two tests lacked any time-dependent response (no creep) perhaps suggesting that the indentation occurred solely within a crystalline phase, and two tests were discarded due to erratic jumps in the displacement indicating crushing, fracture, or slipping. The fact that 52 of 56 total tests displayed some time-dependency in the measured response indicates that nearly all indentation tests of cement paste include some effect of C-S-H in the interaction volume. Test durations longer than 1 hour were attempted, but the long-term thermal drift present in the nanoindentation measurement limited the value of the results.

To quantify the inherent drift present in the indenter in the 30 s and 1 hr tests, a sample of polished sapphire was indented with identical load levels and holding times. In each batch of tests, an identical number of creep indentations were performed on the sapphire and on the cement. Since there is no reason to expect creep in the sapphire, any change in recorded indentation depth once the load reached its maximum level was attributed to drift. The average drift rate of the displacement for the 30 s creep tests was -0.0536 nm/s with a standard deviation of 0.00964 nm/s or a coefficient of variation of 18%. The total drift over a 30 s period was less than 3 nm. For the 1 hr tests the displacement drift rate was -0.4316 nm/s with a standard deviation of 0.0286 nm/s and a

coefficient of variation of 2%. For both the 30 s and 1 hr creep tests of cement paste, the displacement response was adjusted to account for the drift rate.

Atomic force microscopy

Figure 15 schematically illustrates the concept of AFM based indentation. As the actuator presses the probe tip into the material, the cantilever bends upward and the difference in these displacements is interpreted as the penetration depth. Additionally, if the stiffness of the cantilever is known, the deflection of the end of the cantilever also defines the force applied to the tip.

The AFM based indentation experiments in this study were performed with a Veeco Dimension Icon atomic force microscope. Interestingly, during the conclusion of this research the AFM division of Veeco was purchased by Bruker. Since the atomic force microscope used in this research was housed at Sandia National Laboratory, where photography was strictly prohibited for national security reasons, a stock photo of the Dimension Icon is shown in Figure 16. Combining these two facts, the instrument used in this research was identical to the one in Figure 16 except for the Bruker logo, which was a Veeco logo.

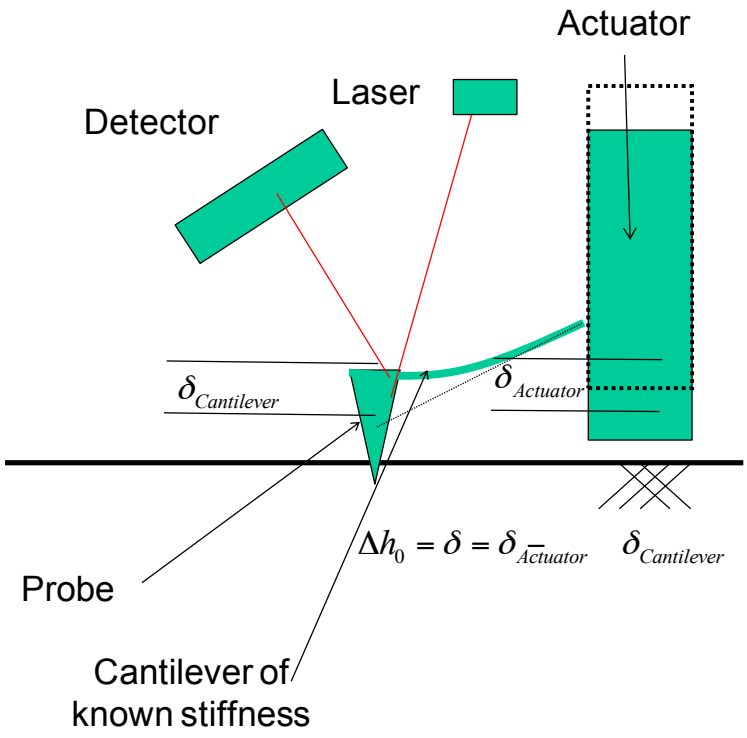

Figure 15: A schematic representation of an atomic force microscopy probe shows the deflection of the cantilever being generated by the movement of the base of the cantilever. The deflection of the cantilever and the movement of the actuator define the penetration depth δ of the AFM probe.

In concept, the experiment is identical to the nanoindenter based experiment but with a few key procedural differences that are inherent to the atomic force microscope. First, the deflection sensitivity of the cantilever used must be determined. Second, the spring constant or k value must also be obtained for the cantilever. The calculated value of deflection sensitivity is obtained by deflecting the cantilever against a very hard material such that negligible deformation of the surface can be expected and all of the movement of the actuator is directly related to deflection of the cantilever. For these experiments a calibrated cantilever was used that had a k value of $219 N/M$.

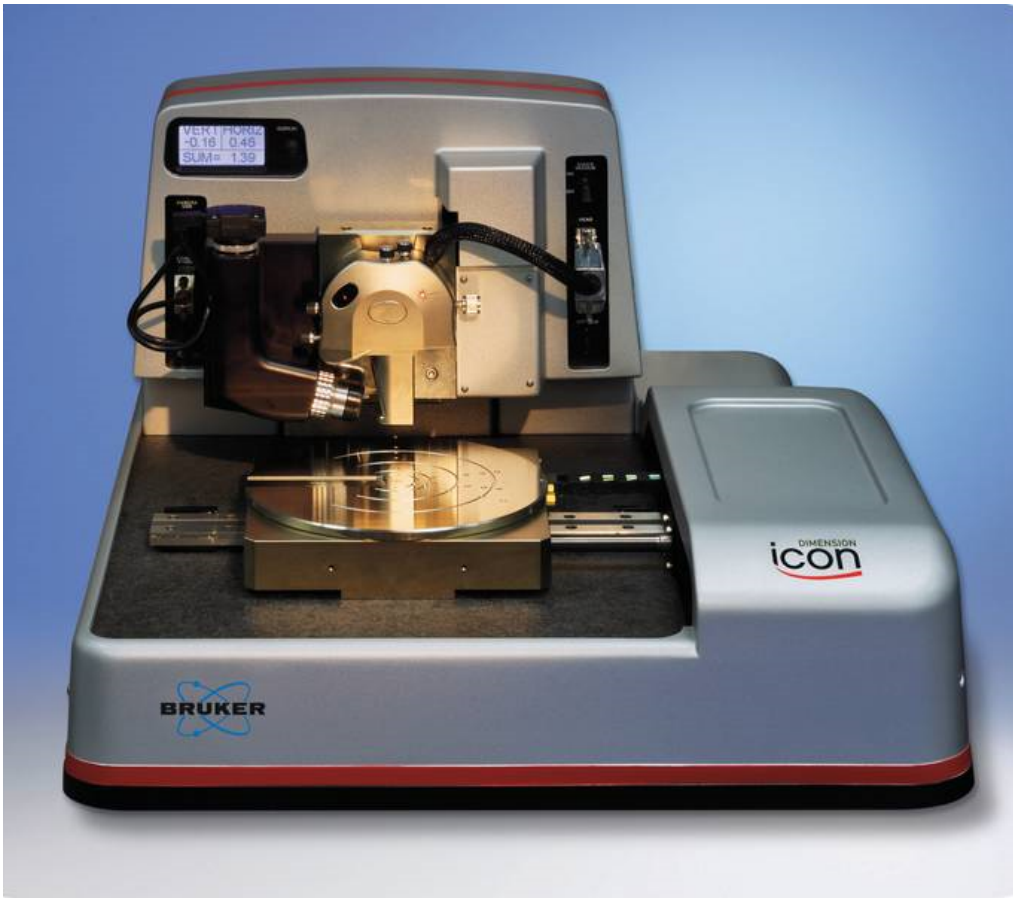

Figure 16: The Dimension Icon system used in this research was actually manufactured by Veeco before the acquisition of the AFM division of Veeco by Bruker. The instrument used in this research was identical to the device pictured here except for the Bruker logo [114].

It should be noted that the deflection sensitivity is dependent on the mounting of the cantilever and alignment of the internal laser in the atomic force microscope and therefore should be calibrated each time an experiment or batch of experiments is performed. Finally, the tip of the diamond cube corner probe was scanned across a polycrystalline titanium reference sample to calibrate the tip shape. With the Veeco supplied tip shape deconvolution routine, the tip radius was found to be approximately 40 nm which is in good agreement with the tip specifications. For these AFM based

experiments the indentation depth averaged 36.6 nm such that only the spherical tip of the otherwise pyramidal indenter probe interacted with the sample.

Since the cantilever deflection values are calculated based on changes in photodiode voltage values from a baseline, the resultant data must be shifted to accurately match the zero force and zero indentation depth points of the curve. This is done by simply setting an offset to the indentation depth and to the applied force data to accurately shift the origin of the plot to the correct point. This correction is necessary simply due to the inherent design of the atomic force microscope.

For the elastic AFM based indentations, 5x5 grids of indentation points were performed at 8 different randomly selected locations on the surface of the cement paste specimen.

Unfortunately, for creep indentation purposes, the particular instrument used in this research could not reliably maintain feedback control on the cantilever deflection (applied force) signal. This prohibited true "creep" (constant applied force) experiments from being performed. On the other hand, the experiment could not be performed as a true "relaxation" (constant applied displacement) test either owing to cantilever deflection as the method of load application in AFM. Given these limitations, the experiment was performed by applying a specified actuator rigid displacement step and then maintaining this step for a specified period of time. The experiment is schematically demonstrated in Figure 17.

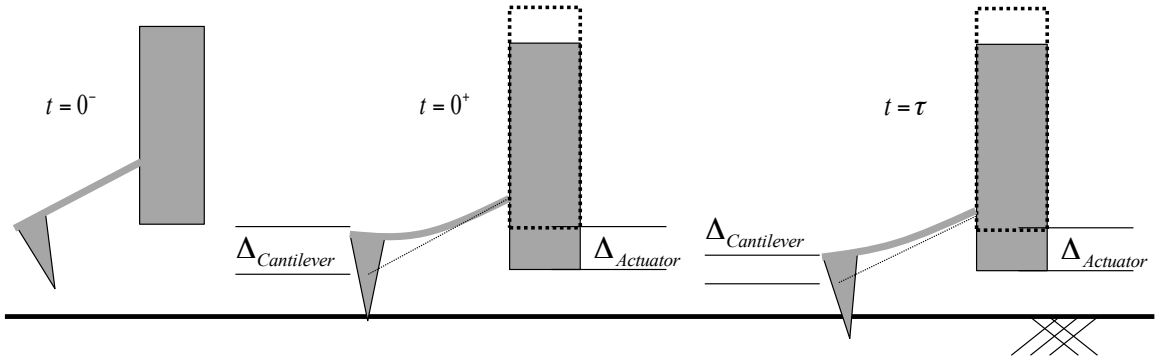

Figure 17: The conceptual representation of the time-dependent indentation experiment performed in this research illustrates that with step actuator movement the cantilever deflection is reduced due to material relaxation.

The electronic feedback loop of the atomic force microscope was able to very accurately maintain the actuator displacement of the base of the cantilever. However, as the material relaxed under the stress of the probe the cantilever's deflection was also reduced. Fortunately, the deflection in the cantilever is very accurately recorded and this value with respect to time can be easily fitted with

$$F(t) = F_{Max} - \sum F_i \left(1 - e^{(t/\tau_i)}\right), \tag{30}$$

where P_{Max} is the initial maximum force, P_i is the fitted parameter controlling the magnitude of the loss of force over a characteristic time τ_i. For these experiments $i = 3$, or three summed terms, fit the loss of force data extremely well with τ_i values corresponding to decades of time, in this case $\tau_i = 0.3, 3, \text{and } 30$ seconds. The form of (30) was chosen as a mathematically convenient form for integration as a part of (29). The load loss was also calculated according to

$$F_{Loss} = \frac{F(0) - F(t_{Max})}{F(0)} \times 100 \quad (31)$$

,

where t_{Max} is the total duration of the load application. F_{Loss} for all experiments was on the order of 1-2%. This was considered acceptably small when compared with the typical change in penetration depth (calculated similarly to (31)), which was on the order of 10-20%.

Since the cantilever deflection values are calculated based on changes in photodiode voltage values from a baseline, the resultant data must be shifted to accurately match the zero force and zero indentation depth points of the curve. This is done by simply setting an offset to the indentation depth and to the applied force data to accurately shift the origin of the plot to the correct point.

Relative humidity control

Moisture within the porous cement paste has long been considered to play an important role in its time-dependent mechanical behavior [115] and for this reason creep indentation tests were performed at several distinct moisture levels. With bulk specimen testing, waiting for complete equilibration of the sample to a change in relative humidity (RH) can take a very long time depending on the sample dimensions. With the AFM based indentation tests however, only the top few hundred nanometers are interacted, and therefore complete moisture equilibration of the entire sample need not be achieved. For this research four different RH levels were investigated: 40%, 80%, 90%, and wet. For the wet sample, a drop of de-ionized water was placed on the polished surface of the

sample and allowed to diffuse into the sample for several minutes before testing. A layer of water was present at all times during the wet sample testing. For the 80% and 90% RH tests, the relative humidity was controlled with a custom water bubbler system that fed compressed nitrogen gas through a porous stone immersed in de-ionized water. The resulting fine distribution of bubbles maximized moisture uptake in the nitrogen. The flow of gas then entered a chamber filled with glass beads to remove any large water droplets and ensure that only vapor was being passed through the system. Finally, the flow of "wet" gas was blended with additional dry nitrogen to achieve a given RH level. The relative humidity of the blended gas was measured with an electronic RH sensor just downstream of blending and then again after the gas had flowed over the sample. The system was considered to be in steady state equilibrium when the electronically measured relative humidity between the two sensors held steady within 1% of one another (i.e. 89.5% and 90.5%). Figure 18 shows a schematic of the bubbler system.

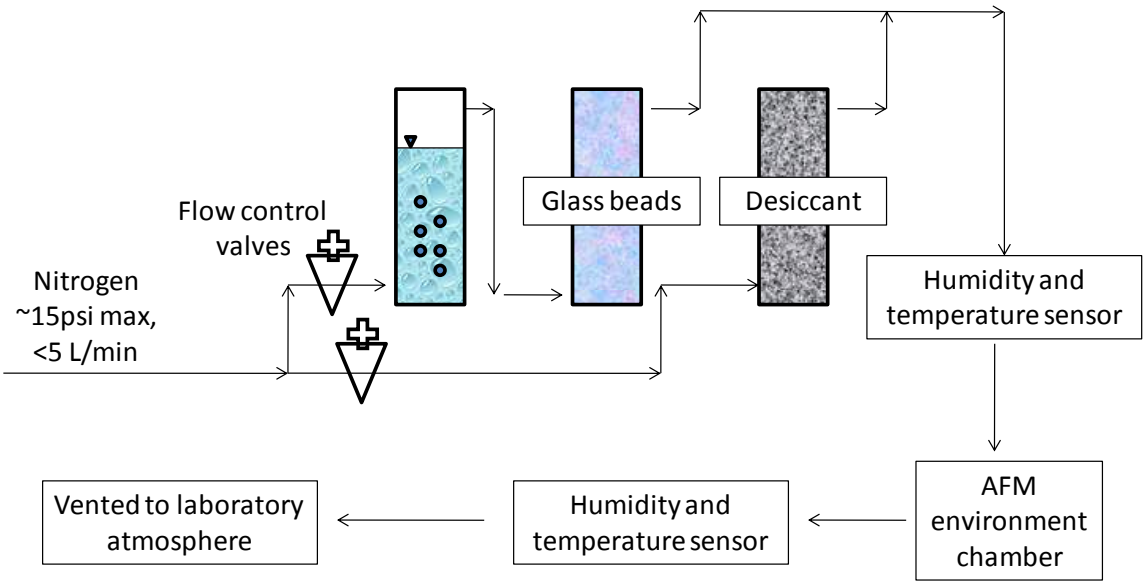

Figure 18: The customized bubbler system for controlling the relative humidity of the portland cement paste during AFM indentation tests works by blending "wet" gas with dry gas to achieve a desired relative humidity.

The humidity controlled gas was contained around the sample with a silicone "skirt" that attached to the scanner tube of the atomic force microscope and then sealed against a flange that encircled the sample. The seal was achieved primarily by deforming the silicone skirt and was enhanced by a thin layer of vacuum grease both on the scanner tube and on the flange. Since the flow rate of the gas was low and since the chamber was vented, very little pressure was developed around the sample and the silicone skirt was able to maintain a stable environment.

Experimental challenges

This research involved novel experimental techniques and the development of these techniques involved overcoming various challenges. Perhaps the most significant problem encountered in this program was the issue of drift when performing longer term

creep indentation tests. Since the actuators in both the nanoindenter and the atomic force microscope are piezo-electric, maintaining an extended position for an extended period of time causes the buildup of heat in the actuator. It is believed that piezo heating is the most likely source of the drift noted in these experiments. As mentioned above, this drift was characterized by indenting a sample of polished sapphire and recording the time dependent behavior. Figure 19 shows a long term AFM based indentation test performed on sapphire.

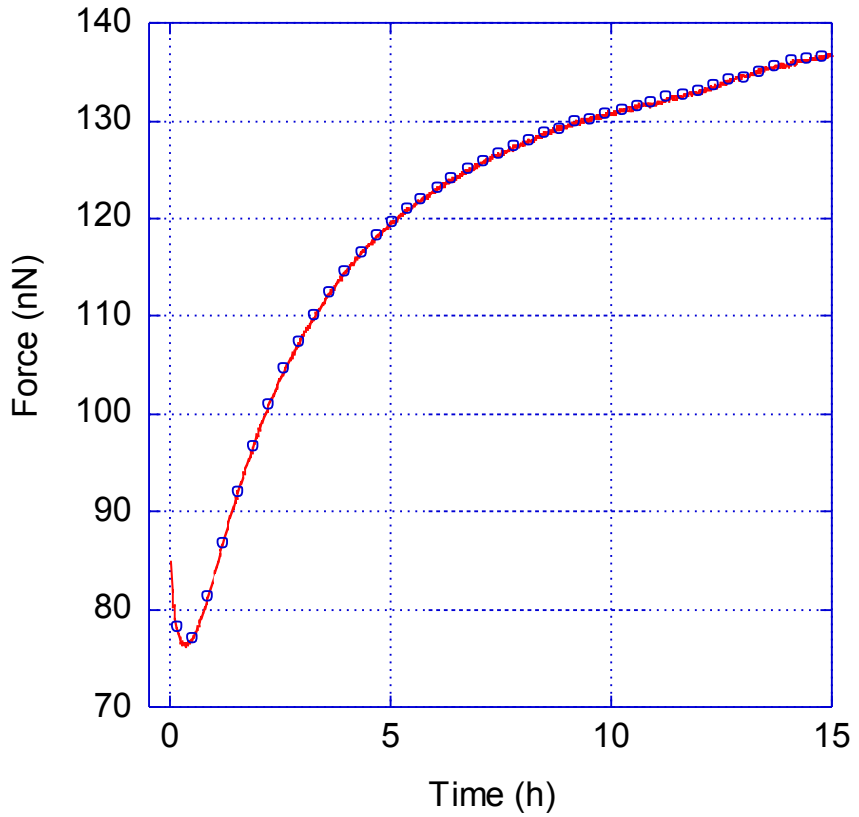

Figure 19: The long term drift inherent to the atomic force microscope made long term creep testing of the material difficult.

The long term drift represented in Figure 19 proved difficult to account for since it was rather large in magnitude and very non-linear. A similar trend was also noted with the nanoindenter drift. Because of this problem long term nanoscale creep tests with either AFM or nanoindentation may prove very difficult. Recently released technology from CSM Instruments does attempt to solve this problem for nanoindentation [116].

CHAPTER V

RESULTS

This chapter focuses on reporting the results of the experimental program described in the previous chapter. A discussion of these results and their implications will occur in the subsequent chapter. This chapter will be divided into two main sections reporting elastic and viscoelastic results. In the elastic results section, the mechanical properties obtained from nanoindentation, on the micron length scale, will be compared to the mechanical properties obtained from AFM based indentation, on the sub micron length scale. The viscoelastic section will also include a comparison between the data collected from each instrument, but the results from each instrument will primarily be separated into sub sections for clarity.

Elastic

A total of 200 AFM based indentations were performed at various locations on the cement paste sample as well as 44 traditional nanoindentation tests. Since the θ value associated with the AFM indentation tests was approximately 1000 on average, the retraction portion of each test was fitted with (1) to determine M and a value of $\nu = 0.25$ was assumed to calculate E from (3). Figure 20 shows a histogram of the measured moduli from the AFM indentation tests along with similar results obtained from nanoindenatation.

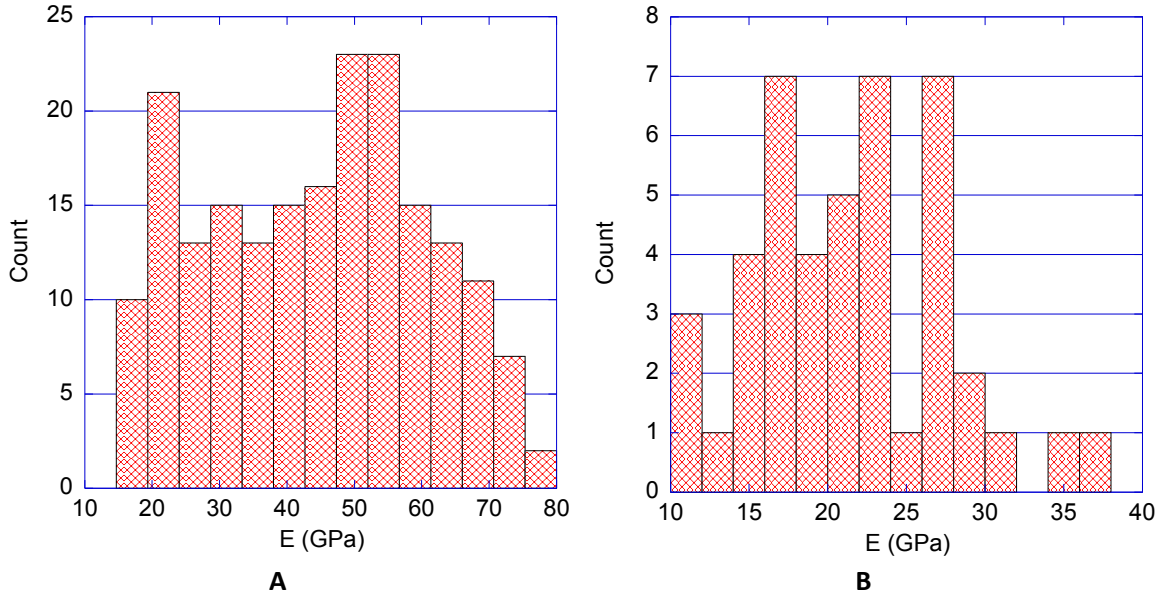

Figure 20: A) The elastic Young's modulus measured with AFM shows an apparent bimodal distribution while B) Young's modulus measured with nanoindentation [44] shows a multimodal trend.

It is interesting to note in Figure 20A that the distribution appears to be bimodal in nature as opposed to multimodal (when measured with nanoindentation) as suggested in recent literature [25, 68] and in Figure 20B. It is also interesting to note that the average value of E extracted from the AFM tests is higher than that measured with nanoindentation.

Two plausible explanations exist in the literature for the modality of the distribution of elastic properties measured with indentation tests. The first plausible explanation of the modality of E obtained from indentation tests can be gleaned from the colloidal model for C-S-H. This model proposes small spherical particles as the

basic building block of C-S-H. According to the model, these particles flocculate into larger, roughly spherical clumps that in turn flocculate into the C-S-H gel. Jennings [69] suggested that C-S-H particles are packed in two distinct densities: low density and high density forms. Based on Jennings' model, Ulm et al. [34, 36, 49] has suggested that there are a limited number of *distinct* packing densities (either 2 or 3) of the C-S-H particles, with each distinct packing density reflecting a peak in the measured Young's modulus determined through nanoindentation. The second plausible explanation for the modality of measured E is related to the presence of multiple phases (i.e. C-S-H with other phase(s)) within the interaction volume of the indentation test [37, 66]. Either proposed mechanism (alone or in concert) could explain the observed modality in nanoindentation results.

However, there are distinct differences between the materials probed in the AFM test versus the nanoindenter test. Figure 21 shows a typical AFM topography image of polished cement paste that indicates rounded particles grouped into clumps, which ostensibly supports the colloidal spheres model of C-S-H. Furthermore, the clumps appear to have interspersed voids. In general, a topographical image from AFM does not have great intrinsic quantitative value other than for determination of morphology, but in this case, AFM images can be useful for providing insight into the interpretation of the AFM indentation results.

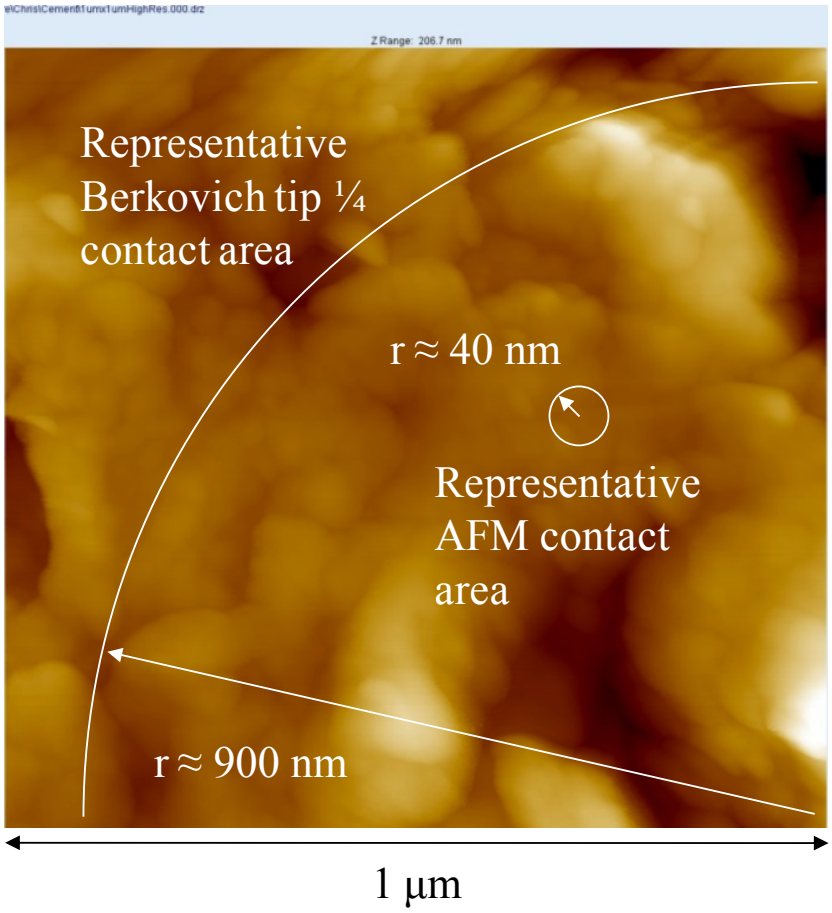

Figure 21: A typical AFM topographical image of cement paste seems to support the colloidal structure of C-S-H. Inscribed on the image are representations of the approximate contact areas of the AFM probe and a typical nanoindentation probe at maximum indentation depth.

Figure 21 shows scaled representations of the typical contact area between the indenter tip (AFM or nanoindenter) and the cement paste. The significant difference in contact area suggests that the nanoindenter is interacting with the larger length scale porosity while the AFM based indentations are not. As a result of this observation, it appears likely that the bimodal distribution of measured E with AFM compared to the multimodal distribution measured with the nanoindenter is explained by the increased

influence of porosity when testing with nanoindentation. When comparing the results in Figure 20A to analogous nanoindenter results in Figure 20B and the literature [25, 44], the peak missing from Figure 20A appears to be that in the lowest stiffness range, which would correspond to interaction volumes containing larger porosity that is avoided in the AFM tests.

Viscoelastic

Viscoelastic nanoindentation experiments were performed with both the nanoindenter and with the atomic force microscope. The results are similar but distinct. In the interest of clarity the results obtained from the two instruments will be separated.

Nanoindentation

Once the corrected creep curves were obtained for the cement paste, the indentation depth with respect to time, $h(t)$, was plotted and fitted with (27). The creep compliance function is assumed to be of the form of a stretched exponential [117], which has been used previously to fit short-term creep of cement paste [118]. A modified form of the stretched exponential function is

$$J(t) = \frac{1}{E_0} + \frac{1}{E_1\left(1 - e^{-1}\right)}\left(1 \quad e^{-(t/t_h)^{\beta}}\right), \tag{32}$$

where E_0, E_1, and β are fitting parameters. In the second term of (32), the presence of $\left(1 - e^{-1}\right)$ in the denominator serves to normalize the entire term from 0 at $t = 0$ to $1/E_1$ at

$t = t_h$. The form of creep compliance expressed in (32) was chosen because it fits data well with only a few fit parameters and the fit parameters possess physical meaning. When t_h is chosen to match the length of the load hold period of the test in question, the constitutive parameter E_0 controls the initial (instantaneous) elasto-plastic penetration into the material, E_1 controls the magnitude of the time-dependent penetration into the material over time t_h, and β controls the shape of the relaxation/retardation function. The parameter E_0 was determined using (19) and (3) with the initial measured loading depth at $t = t_l$. It is critical to note that this parameter is not equivalent to the elastic Young's modulus since the initial penetration almost certainly includes plastic deformation in addition to elastic deformation. The parameters E_1 and β were determined by fitting (27) with $J(t)$ expressed in (32) to the measured $h(t)$ using nonlinear regression. Figure 22 shows a typical 30 s creep curve fitted with (27).

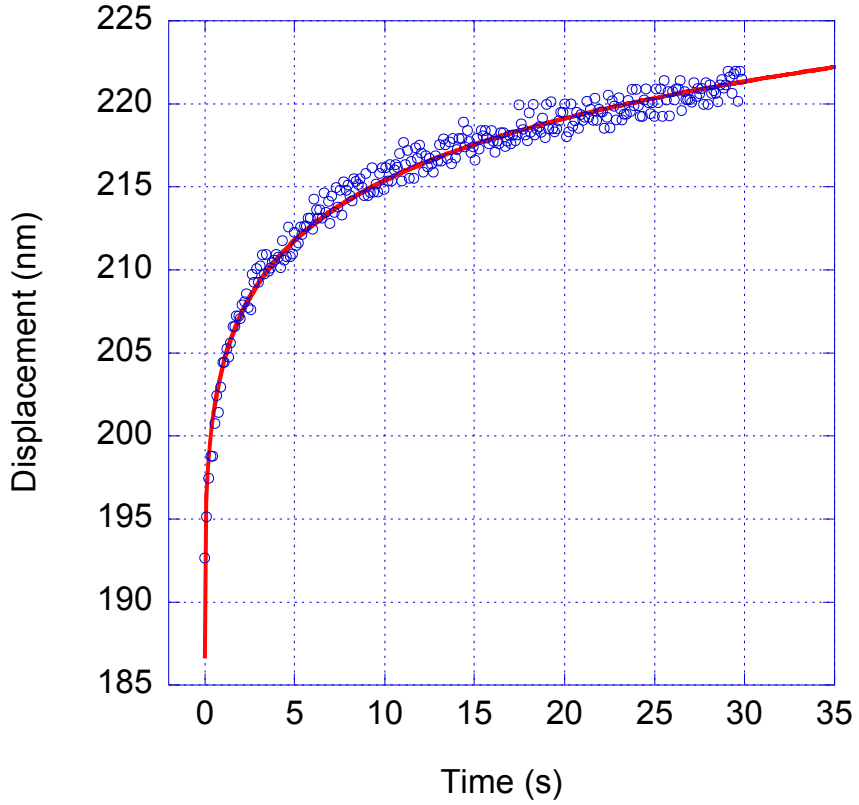

Figure 22: Typical 30 s nanoindentation displacement versus time plot including the fit function. The data has been time shifted so that $t = t - t_1$.

Table 1 shows a summary of the average fitted parameters for the 30 s load holding data and for the 1 hr load holding data as well as the averages, standard deviations, coefficients of variation, and average *r*-squared value.

Table 1. Fit parameters for the 30 s load holding data and for the 1 hr load holding data.

	t_h=30 s				t_h=1 hr			
	E_0	E_1	β	r^2	E_0	E_1	β	r^2
Average	10.772	27.311	0.280	0.987	10.342	2.038	0.755	0.898
Stand. dev.	5.202	14.261	0.026		1.536	2.851	0.242	
Coeff. of var. (COV)	0.483	0.522	0.092		1.115	1.399	0.321	

By comparing the fit functions (27) evaluated at the mean values for E_0, E_1, and β for both the 30 s creep tests and the 1 hr creep tests, the similarity between the functions can be shown. Figure 23 shows (27) plotted with the mean values of E_0, E_1, and β obtained from both the 30 s and 1 hr tests.

Figure 23 shows that the increase in displacement plateaus after roughly 30 to 40 s for 1 hr load holding time tests. This plateau in displacement seems to imply that the reduction in material stiffness also plateaus over this time frame, but this is not necessarily the case. For an indenter of increasing cross-sectional area with depth of penetration, the applied stress decreases with increasing penetration depth. Similar to the size effect discussed by Nemecek [119], as the indenter creeps into the material the applied stress (under constant load) is reduced since the contact area increases with time.

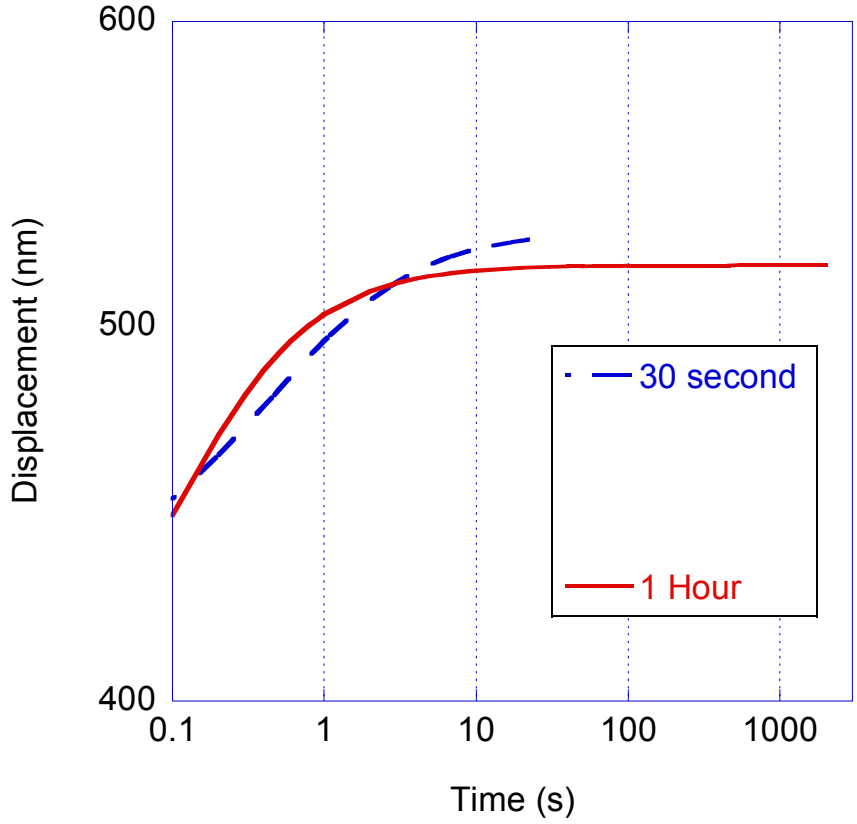

Figure 23: The fit function $h(t)$ plotted using the mean values of E_0, E_1, and β calculated from the 30 s tests and from the 1 hr tests.

Various functions have been developed to characterize the contact area to penetration depth relationships for indenter tips. The contact area versus depth relationship generally obeys a parabolic relationship of the form

$$A(h) = C_0 h^2 + C_1 h^1 + C_2 h^{1/2} \ldots + C_n h^{1/(2^{n-1})}, \tag{33}$$

where $C_0 - C_n$ are tip specific parameters and h is the indentation depth. For a Berkovich indenter, $C_0 = 24.5$. If only the first term is considered and the average stress is assumed to be $1500\,\mu\mathrm{N/A(h)}$, then Figure 24 shows the inverse relationship between

average contact stress and contact area as a function of penetration depth over the realistic range of indentation depths encountered in these experiments.

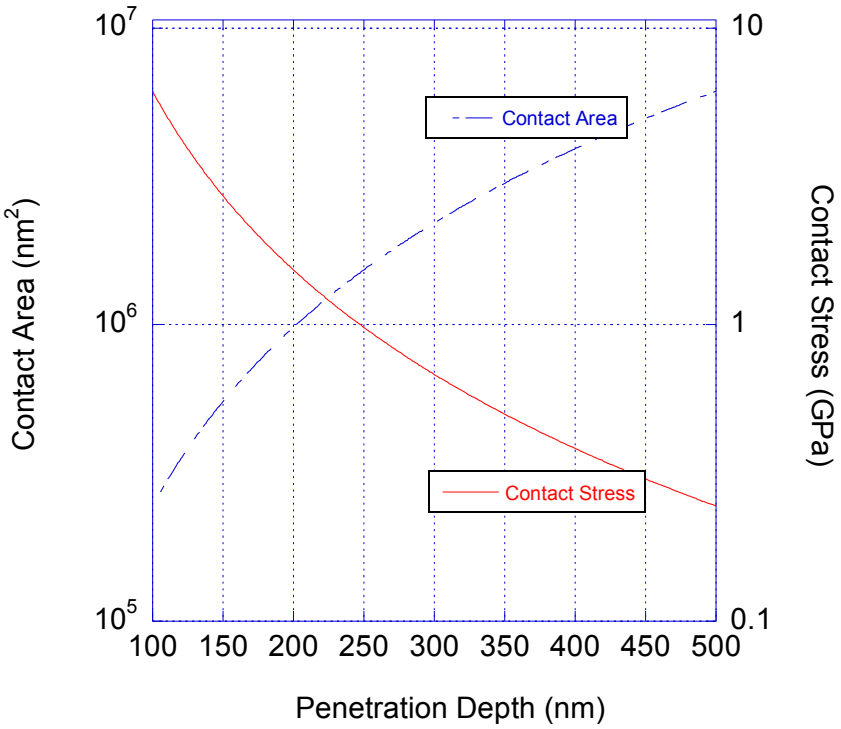

Figure 24: For conical indenters, as the penetration depth (displacement) increases the contact area must increase, thus reducing the applied stress for a constant load. These curves assume a constant load of and a typical Berkovich indenter.

Based on the results shown in Figure 24, it is possible that the dissipation of the displacement rate shown in Figure 23 is not due solely to a reduction in the creep rate, but rather a time-dependent reduction in applied stress. For a Berkovich tip with a half angle of 70.32°, the reduction in stress occurs at a greater rate than for a sharper indenter tip (i.e. cube corner, cono-spherical, etc.). Though longer term creep data was obtained in this study with a Berkovich indenter and successfully fitted, performing long term

indentation creep tests with a sharper indenter may more accurately characterize the long term micro to nano scale creep response of the material and enable even longer term tests to be performed. Additionally, a quasi-static ramp load function instead of a step load function may also improve the viscoelastic characterization of cementitious materials for longer time periods since the reduction in stress would be partially offset by the increasing load.

In agreement with the trimodal distribution of measured elastic and viscoelastic responses recently reported by Vandamme and Ulm [55], many of the model fitting parameters obtained from fitting the measured indentation creep data with (27) also showed a multimodal trend. Figure 25 shows the histograms for the fit parameters that indicate a multimodal response. A histogram of E, the elastic Young's modulus (calculated from the unloading slope) is also included in Figure 25, and agrees well with data shown in [34]. The parameters E_0 and E_1 in particular demonstrate trimodal distributions. The trimodal response noted in this study could be attributed to varying quantities of low density (outer product) C-S-H, high density (inner product) C-S-H, and ultra high density C-S-H within the indentation interaction volume, or it could be related to varying amounts of crystalline phases present in the interaction volume as shown in [25] and suggested by [37]. Of particular interest is the modality of the parameter E_1, which suggests that there may be distinct mechanisms facilitating the time-dependent response, that the different types of C-S-H proposed for the elastic case may have unique delayed elastic responses, or that varying fractions of crystalline products in the interaction volume results in the trimodal viscoelastic response.

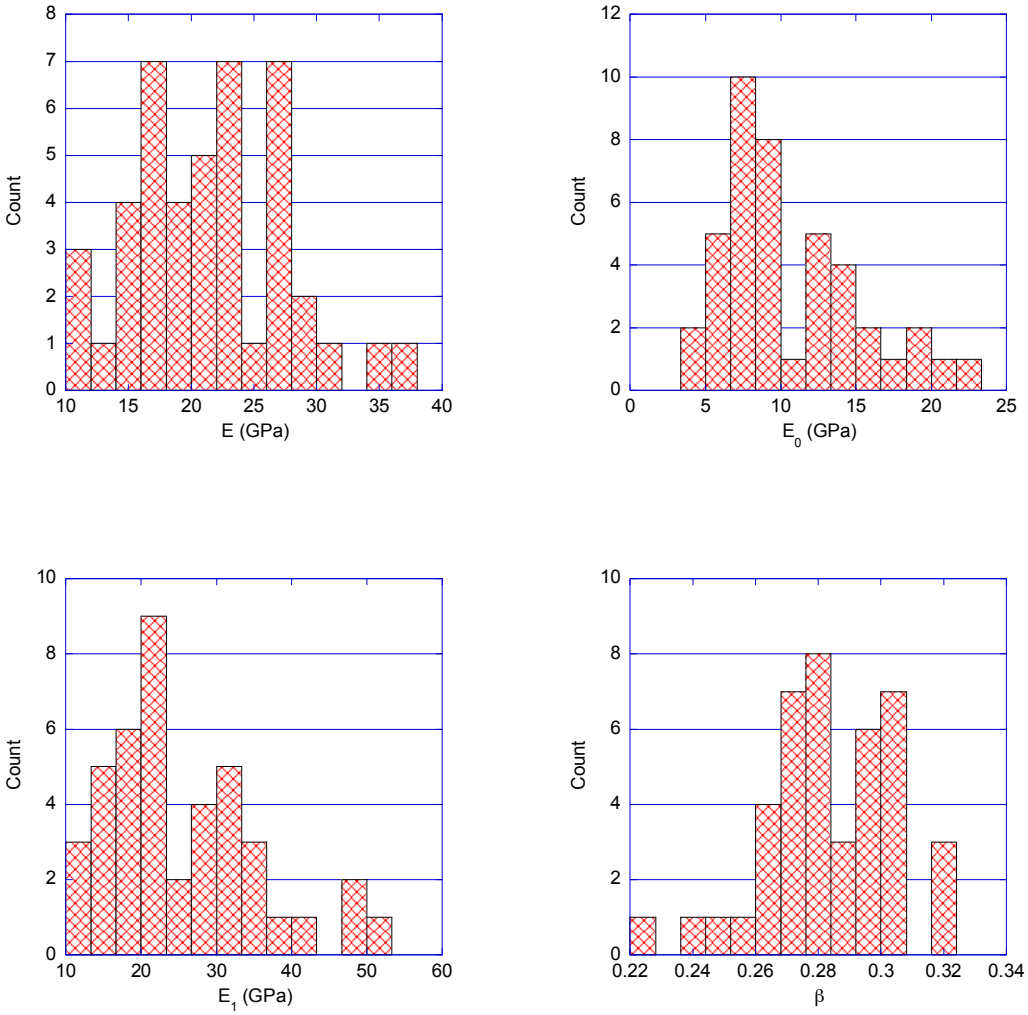

Figure 25: Histograms for the fit parameters obtained from the 30 s creep indentation tests show a multimodal trend.

In addition to the trimodal trend noted in the individual fit parameters, a trimodal trend was also noted in the overall measured displacement response in the creep tests. As a way of analyzing this trend, the probability of measured indentation depth was

analyzed. The probability of the response function (27) was decomposed as the sum of three overlaid Gaussian distributions as

$$P\left(h\left(t\right)\right) = a\,P\left(h\left(t\right)_{low}\right) + b\,P\left(h\left(t\right)_{medium}\right) + c\,P\left(h\left(t\right)_{high}\right), \tag{34}$$

where P is the probability and a, b, and c are linear multipliers that represent the fraction of each type of response (low, medium, or high deformation, respectively) such that $a+b+c=1$. The variability of a function can be approximated using the Delta Method [120], where the function is approximated by a first order Taylor's series. The variance of the total function can be approximated as

$$Var\left(h_j\left(t,x_i\right)\right) = \sum_i \left(\frac{\partial h_j\left(t,\bar{x}_i\right)}{\partial x_i}\right)^2 Var\left(x_i\right) + \frac{\partial^2 h_j\left(t,\bar{x}_i\right)}{\partial x_i \partial x_k} Cov\left(x_i x_k\right),\ i \neq k \tag{35}$$

where $h_j\left(t,x_i\right)$ is the set of displacement functions for low, medium, or high deformation material, x_i is the set of fit parameters present in the function h_j (i.e. E_0, E_1, or β), $\bar{x}_i$ is the set of mean values computed for the fit parameters E_0, E_1, or β, and $Cov\left(x_i x_k\right)$ is the covariance between variables x_i and x_k. A significant covariance was found between E_0 and E_1, indicating that mechanisms or material structure that dictate the magnitude of E_0 likewise dictate the magnitude of E_1. With the variance for each function, and assuming a Gaussian probability distribution for each $h_j\left(t\right)$, the total probability density function (PDF) for the measured $h\left(t\right)$ can be formulated as

$$P\left(h\left(t\right)\right) = a\frac{1}{\sqrt{2\pi Var\left(h_{low}\left(t,\overline{x_i}\right)\right)}}\exp\left[-\left(\frac{\left(h\left(t\right)-h_{low}\left(t,\overline{x_i}\right)\right)^2}{2Var\left(h_{low}\left(t,\overline{x_i}\right)\right)}\right)\right]$$
$$+b\frac{1}{\sqrt{2\pi Var\left(h_{medium}\left(t,\overline{x_i}\right)\right)}}\exp\left[-\left(\frac{\left(h\left(t\right)-h_{medium}\left(t,\overline{x_i}\right)\right)^2}{2Var\left(h_{medium}\left(t,\overline{x_i}\right)\right)}\right)\right] \quad (36)$$
$$+c\frac{1}{\sqrt{2\pi Var\left(h_{high}\left(t,\overline{x_i}\right)\right)}}\exp\left[-\left(\frac{\left(h\left(t\right)-h_{high}\left(t,\overline{x_i}\right)\right)^2}{2Var\left(h_{high}\left(t,\overline{x_i}\right)\right)}\right)\right],$$

where $a = 0.1219$, $b = 0.1953$, and $c = 0.6829$. The relative weighting of *a*, *b*, and *c* indicates that the high deformation response is most likely to be measured when indenting the material considered in this set of experiments. In contrast, Vandamme and Ulm [55] found that the medium deformation response was most probable for a material with a *w/c* of 0.3 and 25% calcareous filler. Based on the difference in the materials tested in this study and in [55], it is likely that the specimens tested in this study (*w/c* of 0.4) include a greater fraction of low density C-S-H in comparison to those tested by Vandamme and Ulm. This supports the hypothesis that the relative fractions of low, high, and ultrahigh density C-S-H dictates the measured viscoelastic response in nanoindentation tests of cement paste. Additionally, this finding indicates that the viscoelastic response of C-S-H is controllable through material design at the nanoscale. A plot of (36) for the 30 s fit data, with the variance of the $h\left(t\right)$functions approximated using (35), can be seen in Figure 26 (a), which clearly shows a demarcation between high deformation (upper curve), medium deformation (middle curve), and low deformation (lower curve) responses, with the high deformation most probable. The

probability of the viscoelastic Young's modulus, $E(t)$, was also calculated using the same procedure as for the displacement, with a plot of these results shown in Figure 26 (b). The Gaussian PDF that yields the stiffest $E(t)$ (upper curve in Figure 26 (b)) influences the lowest deformation indentation response $h_{low}(t)$, the Gaussian probability PDF that yields the median $E(t)$ (middle curve in Figure 26 (b)) influences the median deformation indentation response $h_{medium}(t)$, and the Gaussian PDF that yields the most compliant $E(t)$ (lower curve in Figure 26 (b)) influences the high deformation indentation response $h_{high}(t)$. The lower coefficient of variation of $E(t)$ in the high stiffness regime causes $COV\left(h_{low}(t)\right) << COV\left(h_{high}(t)\right)$, which tends to sharpen the Gaussian PDF of $h_{low}(t)$ in comparison to the Gaussian PDF of the upper curve of $E(t)$. Likewise, the Gaussian PDF of $h_{high}(t)$ is flattened versus the lower curve of $E(t)$.

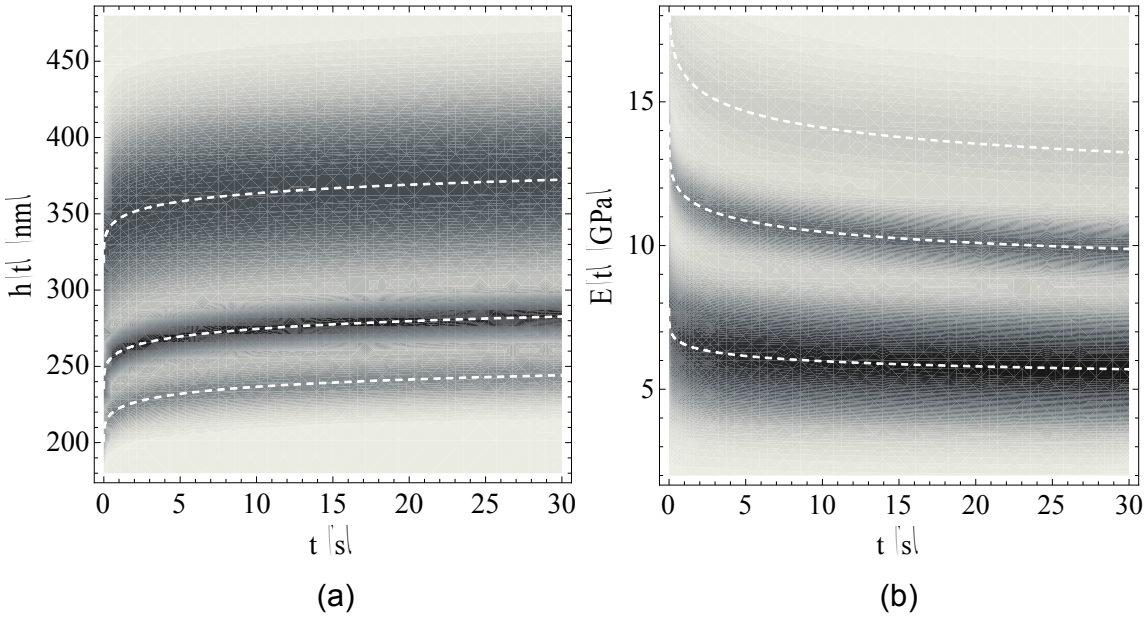

Figure 26: The probability density plots of (a) and (b) showing the trimodal trend of measured displacements and viscoelastic properties extracted from the nanoindentation tests. Darker areas indicate higher probability, while dashed lines indicate mean values for each Gaussian probability density function.

Atomic force microscopy

The particular form chosen to represent the viscoelastic compliance in this research is that of a Kelvin chain. The expression for the compliance is

$$J(t) = \frac{1}{E_0} + \sum \frac{1}{E_i}\left(1 \quad e^{(t/\tau_i)}\right), \tag{37}$$

where E_0 defines the instantaneous deformation response of the indented material, E_i are the fit parameters, and τ_i are the characteristic times over which the relaxation occurs. As with the load $P(t)$, the creep data was very accurately characterized with three terms corresponding to three decades of time response.

With (30) defined, the approximation that $\nu = 0.25$, and a form for $J(t)$ as shown in (37), the experimental data could be fitted with (29) using a non-linear fitting routine in *Mathematica*. A typical viscoelastic indentation test with the best fit line from (29) is shown in Figure 27.

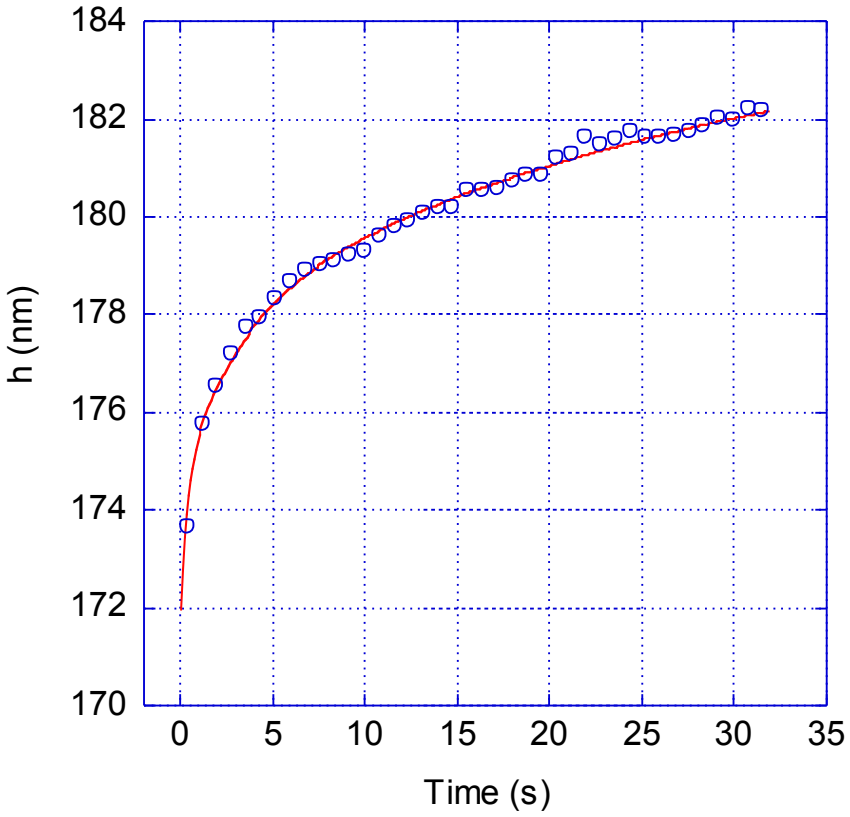

Figure 27: Typical creep indentation test data obtained with AFM showing the best fit line obtained using (29).

Once the experimental data was fitted, the fit parameters from (29) could be tabulated and analyzed. Table 2 shows the fit parameters obtained for the 30 second AFM based creep indentation tests performed at the various relative humidity levels.

Table 2. Fit parameters for the 30 s load holding data obtained at various relative humidity levels.

	RH=40%				RH=80%			
	E_0	E_1	E_2	E_3	E_0	E_1	E_2	E_3
Average	1.79	85.82	27.15	1236.81	0.86	337592.79	15.16	76.59
Stand. dev.	1.90	255.45	32.98	7968.57	0.37	674346.06	5.80	129.04
Coeff. of var. (COV)	1.06	2.98	1.21	6.44	0.43	2.00	0.38	1.68
	RH=90%				RH=Wet			
	E_0	E_1	E_2	E_3	E_0	E_1	E_2	E_3
Average	2.80	239988.33	89.39	59.20	0.79	179749.52	140.04	23444.83
Stand. dev.	1.56	531353.99	84.33	52.01	0.46	577393.62	401.86	59100.16
Coeff. of var. (COV)	0.56	2.21	0.94	0.88	0.59	3.21	2.87	2.52

A large number of tests were conducted at general laboratory conditions to compare with the nanoindentation results from [44]. The relative humidity in the lab was measured with the same electronic sensors used in the bubbler apparatus and was determined to be 40% and very stable. The fit parameters obtained from fitting these 40% RH experimental data were tabulated and are presented graphically in Figure 28. It is interesting to compare Figure 28 to the analogous Figure 25 from the nanoindentation tests. While some modality may be present in Figure 28 it does not appear as pronounced as the modality in Figure 25.

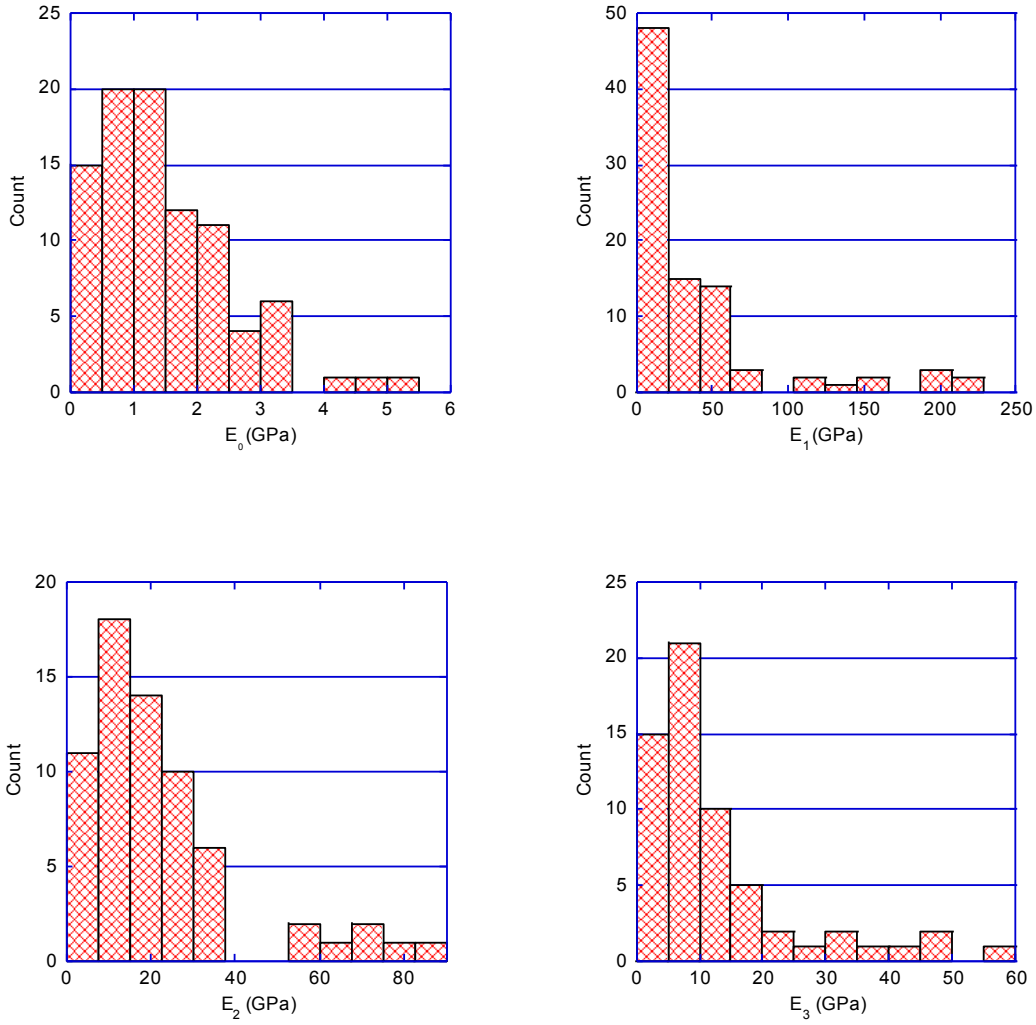

Figure 28: The calculated fit parameters obtained from fitting the 30 second experimental data with(29) at 40% RH, setting $\tau_i = 0.3, 3, \text{and } 30\,\text{s}$.

Figure 29 is a box-and-whisker plot of E_0 for the different moisture levels. The stiffest instantaneous response occurs in the sample at 90% RH while the least stiff measured values occur in the 40% RH tested sample (the lowest mean appears to occur in the 80% RH tests).

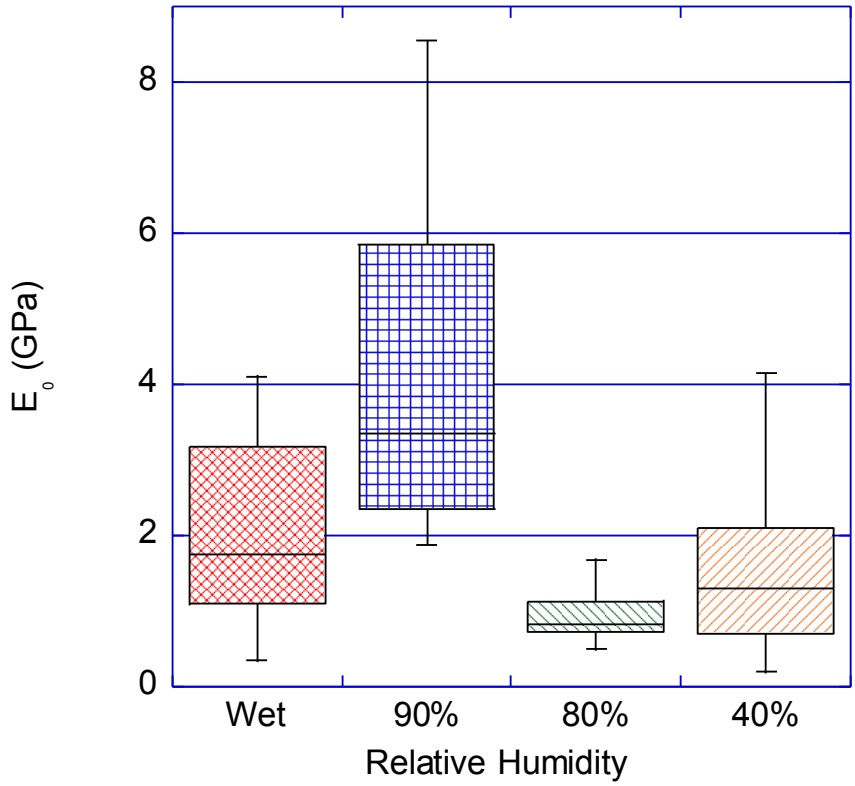

Figure 29: The instantaneous response from the loading portion of the creep indentation (or E_0 from (37)) shows the stiffest instantaneous response at 90% RH.

Additionally, the normalized viscoelastic compliance from the relative humidity controlled tests is shown in Figure 30. The error bars in Figure 31 and Figure 30 represent one standard deviation from the mean in each direction. It is interesting to note that the greatest relaxation occurs in the driest samples rather than the wettest, and that the response does not seem to linearly correlate to the moisture level. Interestingly, the 90% RH tested sample was the least compliant.

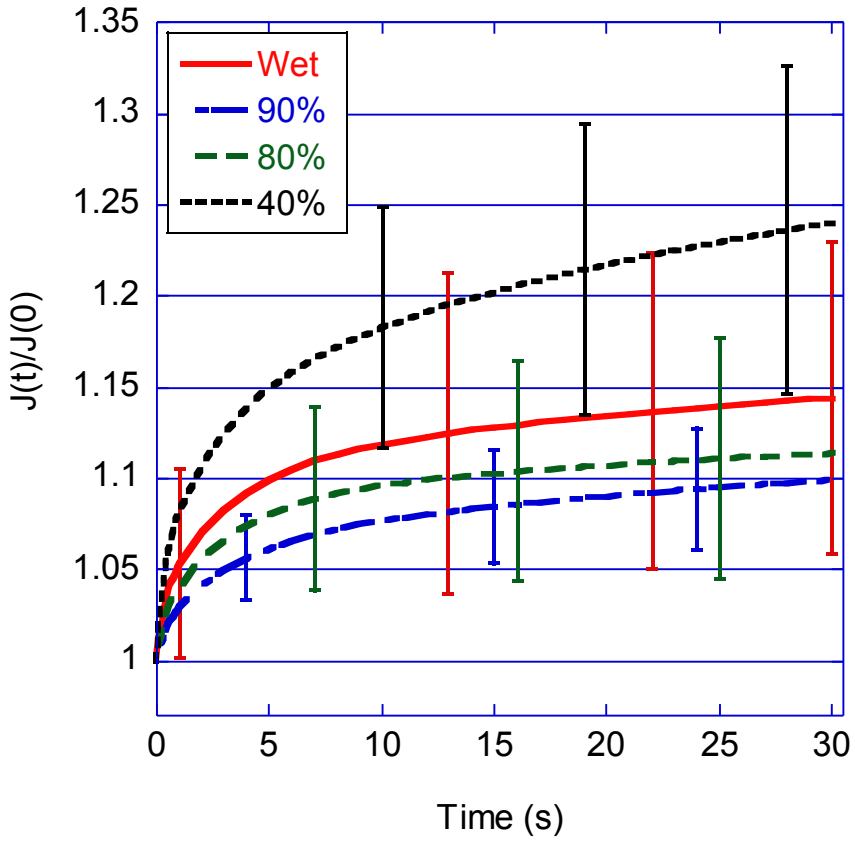

Figure 30: The normalized viscoelastic compliance measured on samples exposed to different relative humidity values shows that the greatest relaxation occurs with the driest sample. The error bars on this plot represent one standard deviation from the mean in each direction.

As a means of addressing the significance in the trends in Figure 30, a Student's T-test was performed using $J(t = 30\text{ s})/J(t = 0\text{ s})$ as the test statistic between the different humidity levels. The T-test revealed significant difference in the means at a 97% or greater level of confidence between the 40% RH tests and each of the other RH levels. There was no statistically significant difference between any of the other combinations. To obtain a more compact representation of the response of the cement paste and to compare the AFM based creep indentation results to analogous results

obtained from nanoindentation, the fit parameters were averaged, and an average compliance function plotted. Figure 31 shows the average compliance $J(t)$ normalized by the initial value, $J(0)$, from this study measured with AFM and with analogous data measured with nanoindentation from [44].

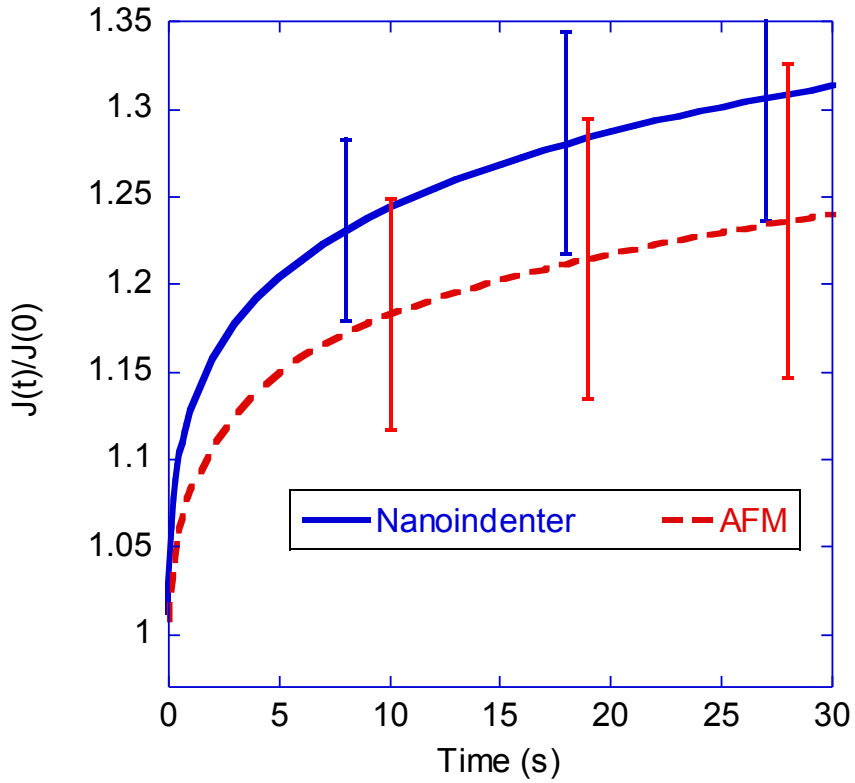

Figure 31: The normalized viscoelastic compliance measured with AFM and nanoindentation at RH = 40% in each case. The error bars in this figure represent one standard deviation from the mean in each direction.

The primary difference noted from Figure 31 is that over this time period, the material relaxes more when tested with nanoindentation than when tested with AFM; however the shape of the two curves appears similar. To validate this apparent

distinction, a Student's T-test was performed using $J\left(t = 30\text{ s}\right) / J\left(t = 0\text{ s}\right)$ as the test statistic between the AFM and nanoindenter data. The T-test revealed significant difference in the means at a 99% level of confidence between the two test methods.

CHAPTER VI

DISCUSSION AND INTERPRETATION

This chapter summarizes the work presented from this research and will also discuss and interpret the results presented in the previous chapter. The discussion in this chapter is indented to provide a measured and unbiased assessment of the results obtained within the context of the relevant literature. The particular field of nano-scale mechanical characterization of portland cement has a relatively high level of controversy, particularly surrounding the implications of the experimental data. Therefore, the present results are interpreted within the context of the relevant competing theories and where appropriate, conclusions are made.

Discussion of elastic results and mechanisms

For the elastic indentation results, two significant trends are apparent when comparing results from the nanoindenter and from AFM based indentation. First, the average elastic Young's modulus value measured with AFM indentation is higher (stiffer) than the measured value with nanoindentation. Second, the distribution of AFM indentation measured Young's modulus appears bimodal while the distribution appears multimodal with nanoindentation. As mentioned previously, there exist two plausible theories in the literature to explain the multimodal distribution of measured properties from nanoindentation tests and these theories can be useful for interpreting the AFM indentation values as well.

Particle packing densities

Within the framework of the colloidal spheres model for C-S-H, it is hypothesized that there exist distinct levels of packing density within the C-S-H and that these levels of packing density are the most likely cause for the multimodal distribution of the measured elastic Young's modulus with nanoindentation [29, 34-36]. Recalling Figure 3, the colloidal spheres model states that individual C-S-H spheres flocculate into clumps that make up the otherwise amorphous C-S-H gel [31, 47, 70]. It is hypothesized that this flocculation occurs with some regularity, and that the C-S-H spheres pack into distinct density levels thus contributing the multiple stiffness modes present in elastic nanoindentation tests.

Interspersed crystalline phases

It is well known that some crystalline products result from the hydration of portland cement paste [53]. It is hypothesized that these crystalline phases present in the otherwise homogenous C-S-H represent a better explanation for the apparent multimodal distribution of elastic Young's modulus results obtained from nanoindentation testing [25, 37, 66, 121]. This theory suggests that crystalline phases may be present within the interaction volume of a typical nanoindentation test and these crystalline phases would influence the measured results in such a way as to cause a multimodal distribution of results.

Interpretation of elastic properties

Measurements of the elastic mechanical properties of portland cement paste have been successfully conducted with nanoindentation and with AFM based indentation. Particle packing density considering a colloidal spheres structure for C-S-H seems to provide the best framework for reconciling the differences between the AFM results and those obtained with nanoindentation. The hypothesis that packing density explains the difference between AFM and nanoindentation results does not necessarily imply distinct C-S-H packing densities rather than a small gradient in packing density. Thus more research is needed to definitively explain the mechanisms responsible for the distribution of elastic Young's modulus found in nanoindentation.

The reduced influence of porosity on every AFM measurement versus nanoindentation measurement could explain the general upward shift in measured E in AFM results versus nanoindentation results. While the presence of crystalline material in the otherwise amorphous C-S-H could still be an explanation for the distribution of measured nanoindentation results, this explanation is not as plausible for AFM indentation tests. Since the interaction volume of the AFM probe is quite small, the measured values are much less likely to involve influence from multiple phases and are thus likely more representative of the intrinsic properties of the C-S-H particles. Furthermore, the intrinsic E of C-S-H has been approximated as 57 GPa [122], 60 GPa [36], 80 GPa [123], and 34-300 GPa, depending on Ca^{2+} concentration [74]. Since the AFM results indicate E approaching 80 GPa, it is apparent that the intrinsic E of C-S-H must be at least 80 GPa. Indeed, DEM simulations of nanoindentation using 57 GPa

as an intrinsic E of C-S-H underpredicted nanoindentation results [24]. If the intrinsic C-S-H E is only slightly greater than 80 GPa, then the presence of CH within the AFM interaction volume cannot explain the measured AFM indentation results that approach 80 GPa since the E of CH is approximately $40\,\text{GPa}$ [71]. A recent analysis involving molecular modeling of C-S-H with the assumed crystalline structures of tobormorite and jennite indicates that the intrinsic Young's modulus of C-S-H ranges between 51 and $95\,\text{GPa}$ [124]. In addition, perhaps due to sample preparation, virtually no crystalline materials were readily observed on the surface (via AFM imaging) of the samples.

While the presence of unhydrated cement grains ($E \approx 118$ GPa) in the AFM indentation interaction volume could theoretically explain the upper end of the measured E using AFM, the very shallow AFM indentation depth greatly reduces the probability of interacting with unhydrated cement particles since the water used during cutting and polishing would ensure sufficient moisture for hydration of any exposed unhydrated cement particles. Therefore, it is hypothesized that the difference between the measured E obtained from nanoindentation and from AFM is due primarily to differences in particle packing between the two length scales.

Another possible source of the distribution of Young's modulus could be interpreted from variability in the intrinsic C-S-H stiffness based upon chemical differences, primarily the calcium to silicon ratio of the C-S-H. Plassard measured elastic Young's modulus values ranging from 50 to $300\,\text{GPa}$ for synthesized C-S-H depending on the calcium ion concentration of the solution in which the C-S-H was grown [74]. It is possible that there may be intrinsic variability within the C-S-H arising

from chemical differences, but it is unclear if these differences would tend to group into distinct modes or phases.

Discussion of viscoelastic results and mechanisms

Though cement paste and concrete have long been known to experience time dependent relaxation, the specific mechanism for the relaxation has not been determined. Traditionally this viscoelastic relaxation has been attributed to the C-S-H phase of portland cement paste. Several theories exist in the literature for the fundamental mechanism responsible for the viscoelasticity of C-S-H.

Nanogranular densification

The nanogranular densification of the C-S-H phase of cement paste has been proposed as the as the primary mechanism for cement paste creep by Vandamme and Ulm [55]. This densification theory is rooted in the colloidal spheres model for C-S-H proposed by Jennings et al. [31, 41, 70]. Vandamme and Ulm assert that, similar to the densification of granular media such as soil, the individual C-S-H particles rearrange to approach the limit packing density in response to the applied stress field from the indentation probe. Vandamme and Ulm argue that since the contact creep compliance scales with indentation hardness, and that since indentation hardness is controlled by plastic deformation of the material being indented, rearrangement of the C-S-H particles likely controls both phenomena. Vandamme and Ulm also argue that there exist distinct types of C-S-H [34, 36] (distinguished by packing density) and that these types of C-S-H

display distinct time-dependent behaviors owing to the amount of densification that can be achieved. Distinct viscoelastic responses have also been identified by the present authors [44] in nanoindentation tests although this trend was not readily apparent with AFM based viscoelastic indentation test results.

Layer sliding

In a recent study that includes macroscale experiments, Alizadeh et al. propose a slightly different mechanism for creep in C-S-H than the nanogranular densification mechanism, which originates from the Feldman-Serada model for C-S-H structure [78, 79]. This proposed mechanism considers the sliding of C-S-H layers into a more dense state to be the primary time-dependent mechanism controlling C-S-H and cement paste [48] viscoelastic behavior.

Poroelastic relaxation

Cement paste has long been recognized as a porous material and poromechanics has been applied by various researchers to characterize the apparent change in mechanical properties resulting from fluid movement within the porous cement paste (see e.g. [50, 125-129]). In general, the apparent viscoelastic relaxation of a poroelastic material is not truly related to inherent material viscoelasticity of the solid phase comprising the porous body, but rather a time-dependent transfer of stress from the fluid phase onto the solid phase resulting in greater overall deformation. The transfer of stress occurs gradually as the fluid flows from areas of high pressure to areas of lower

pressure. Alizadeh et al. identify the movement of water within the C-S-H as an important mechanism for time-dependent response of cement paste through controlled relative humidity testing.

Dissolution of load bearing phases

Similar to the poroelastic effect described above, it is possible that an apparent viscoelastic effect may arise from the dissolution of solid phases in response to the increased stress generated by the indenter probe. In general the thermodynamic equilibrium resulting from the hydration of portland cement can be viewed as an energy minimized set of most likely resultant phases, but this set of most likely outcomes does depend on factors such as temperature, chemical potential and strain energy. The change in the latter may cause otherwise thermodynamically stable phases to dissolve, thus transferring the applied load to other solid phases. This transfer of load would give the appearance of viscoelastic relaxation through an increase in elastic deformation of the remaining solid phases. The peak applied stress underneath the indenter probe may be very high (on the order of 400 MPa in these experiments) which would tend to increase the significance or probability of this effect. Clearly more investigation needs to be done to evaluate the plausibility of this potential phenomenon on the solubility of solid phases in the cement paste.

Consideration of each mechanism

In Figure 29, the average responses of the material in the wet state and at 90% RH are stiffer than the average responses of the material at 80% and 40% RH. This trend suggests that water is playing a larger structural role in the former two cases than the latter two, which agrees well with the general concept of poromechanics. In this theory, stress is partially carried by the fluid (pore water) and this fluid flows in response to any applied pressure gradients, thus transferring the stress to the adjacent solid phases. In the case of a partially saturated sample, this gradient is expected to be over a very short distance since the pressurized fluid need only flow into an adjacent emptied pore. Therefore, it is hypothesized that the poromechanical relaxation time in the less saturated 80% and 40% RH specimens is shorter than the loading time of the indentation test, and therefore the structural contribution of the pore water is not measured. Furthermore, it is known that the pressure within a porous body decreases (negative pressures) with decreasing internal relative humidity. This phenomenon may help to explain the higher instantaneous stiffness values present in the 90% RH compared with the wet sample since the negative internal pressure may generate a confining effect, thus increasing apparent instantaneous stiffness.

It is apparent that if a poromechanical response is present in the 90% RH and wet sample results as stated above, there must also be some mechanism to explain the presently measured, and otherwise known, viscoelasticity at low humidity levels. In Figure 30, the only statistically significant trend is the difference in response between the 40% RH tests and the other, higher moisture tests. The significant difference in this

case is the increased compliance at 40% RH compared with the other relative humidity levels. Figure 32 is a schematic representation of the hypothesized relationship between relative humidity and time dependent deformation mechanisms present in C-S-H. At high relative humidity levels, the poromechanical effect plays a significant role as evidenced by the stiffer initial response of the material in Figure 29. Furthermore, at lower relative humidity levels the poromechanical effect fades while other mechanism(s) play an increasing role as evidenced by the higher levels of relaxation measured at 40% RH as shown in Figure 30.

In comparing the results obtained from AFM based indentation with those obtained from nanoindentation, both at low relative humidity (as shown in Figure 31) it appears that the other mechanism(s) depend on indentation length scale. This length scale dependence could be related to the indentation of a smaller, relatively more homogeneous, and more densely packed region of the material in the case of the AFM based indentation as compared with the nanoindenter. The reduction in viscoelastic compliance as a result of indenting more homogeneous and more densified C-S-H is in agreement with a time dependent densification of the solid phases of the cement paste.

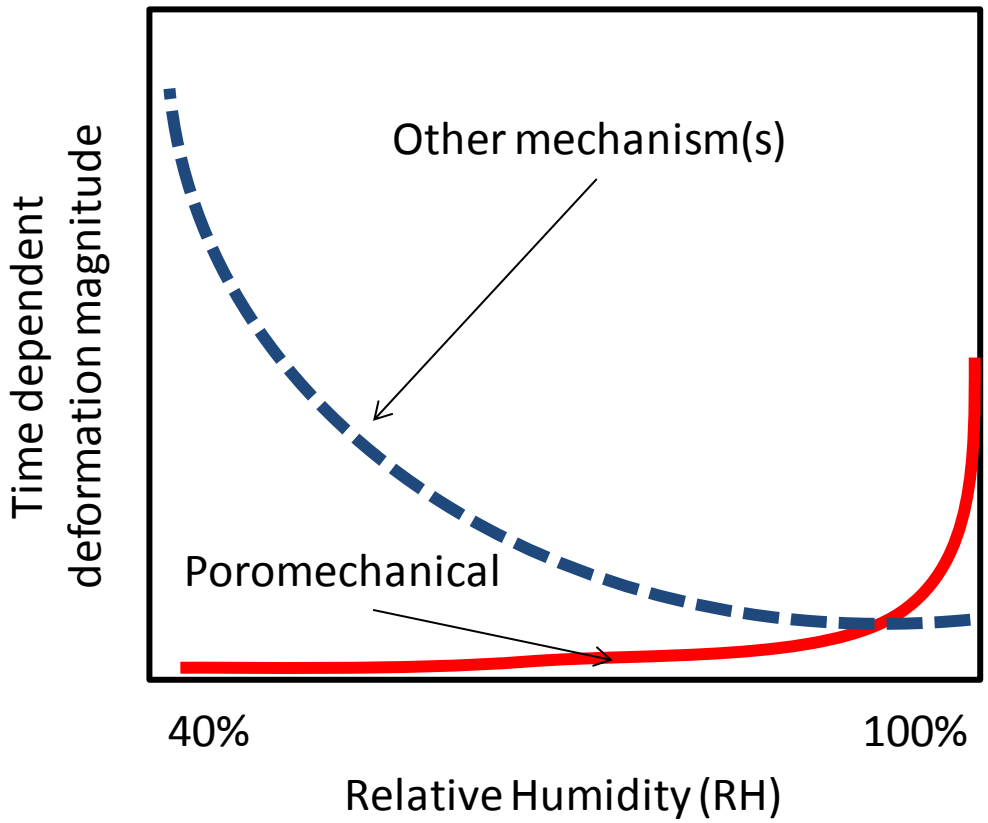

Figure 32: The poromechanical effect is only relevant at high moisture levels and the fact that greater relaxation was measured at low relative humidity levels suggests that other time dependent deformation mechanism(s) must strongly affect the material at low relative humidity levels.

It appears that the nanogranular densification mechanism and the layer sliding mechanism differ mainly in the assumed structure of the C-S-H and that the underlying mechanism of each can be considered equivalent: a time-dependent densification of the solid phase of C-S-H. It is not clear from the experimental data in this study whether the colloidal spheres model or the Feldman-Serada model better represent the true nature of C-S-H. The stress dependent dissolution of load bearing, solid phases deserves more attention, and could also explain the measured, non-poromechanical time dependence, particularly when considering the extremely high stress levels just below the tip.

Interpretation of viscoelastic properties

Viscoelastic material properties of portland cement paste have been successfully measured with AFM based indentation. These properties have been compared to those measured with nanoindentation and significant differences have been identified, most notably the reduction in the overall magnitude of the viscoelastic compliance measured via AFM based indentation versus traditional nanoindentation. From the results presented in this work it appears that the poromechanical effect plays a significant role in the viscoelastic behavior as well as in the instantaneous behavior of C-S-H. Separate from the poromechanical response, it appears that there must be an additional intrinsic mechanism for the time dependency of the mechanical properties of C-S-H. Though the authors have no basis for definitively determining which mechanism is correct, it is likely that a time-dependent densification of the solid phases of C-S-H coupled with the poromechanical effect best explains the measured viscoelastic response of C-S-H. Dissolution of load bearing solid phases remains a possibility, though more investigation is needed to ascertain the plausibility of this mechanism. Furthermore, additional testing should be performed to more completely understand the effect of moisture on the time-dependent response of the material.

CHAPTER VI

CONCLUSIONS AND FUTURE RESEARCH

This chapter will present a summary of the research presented in this work and will identify the main conclusions obtained. Additionally, this section will include a summary of suggested future work that would compliment and advance the research presented in this document.

Research summary

Numerical and analytical modeling approaches are presented and considered for application to AFM based indentation tests, and the two approaches are compared to one another. The numerical approach is considered more general but significantly more computationally intensive. By evaluating a dimensionless parameter θ, the applicability of the analytical techniques can be determined and future experiments may be designed such that analytical modeling is suitable and the computational expense of numerical modeling avoided.

Quantitative AFM based indentation experiments have been performed on portland cement paste for the first time and measured Young's moduli values have been reported. The mean and distribution of the measured values obtained from AFM indentation are distinct from the measured values obtained with nanoindentation.

Creep nanoindentation tests have been performed on cement paste for two different durations. Following the solution of Ulm and Vandamme [54], but with the approximation of a constant value for viscoelastic Poisson's ratio, the displacement

versus time data was fitted. The measured displacement data and fitted viscoelastic constitutive functions indicate that there is a trimodal trend present in the measured creep indentation results and more testing may help to confirm this observation. For the first time, expressions for the viscoelastic uniaxial compliance of C-S-H based on nanoindentation creep tests are reported; these expressions could be used in multi-scale models to predict short-term viscoelastic behavior of bulk cement paste.

Though creep relaxation appears to subside after a few tens of seconds in the 1 hr tests, it is likely due in part to the decrease in applied stress as penetration depth increases. Unfortunately, this phenomenon may limit the applicability of the nanoindentation technique (with a Berkovich indenter) for long loading times and deep indentation depths. Despite this deficiency, the creep nanoindentation technique appears to be a viable experiment for characterizing the viscoelastic response of cementitious materials on a relatively short length and time scale.

Viscoelastic AFM based indentation tests have been performed for the first time on cementitious materials. These tests were conducted at different relative humidity levels by the use of a custom relative humidity control apparatus and these RH controlled measurements have given some insight into the mechanisms responsible for time dependent deformation of cement paste and ostensibly C-S-H.

The most striking result from this research has been the distinct difference in mechanical response of the same material when measured with nanoindentation and with AFM. The exact reason for this difference remains undetermined, however the main test variable changed between the two tests is the indentation length scale. By studying the

various possible mechanisms for deformation of C-S-H present in the literature, some hypotheses can be formed as to this measured difference.

Conclusions

The primary objectives of this study were to experimentally characterize the mechanical properties of ordinary portland cement paste on the tens of nanometers length scale in both an elastic and viscoelastic sense with AFM. Furthermore, this study sought to differentiate these results from analogous results obtained on the hundreds to thousands of nanometers length scale with nanoindentation. In a large sense, these objectives have been reached. In addition several smaller, yet significant, conclusions were reached and they will be presented here.

- The self consistent method, first published by Attard [90], and later generalized by Graham et al. [17] provides the most general description of the contact measured in AFM. For low force and low displacement experiments such as in Figure 10, this self consistent approach is required to accurately model the contact.
- Analytical contact solutions such as the Hertz [80] or Sneddon [81, 82] solutions can be accurately applied to indentation problems, even those on the nanometric length scale, in accordance with high values of the dimensionless parameter θ presented previously.
- AFM based indentation experiments can be designed to maximize θ so that analytical modeling of the experiment can be effectively employed.

- The correspondence principle provides a means of obtaining viscoelastic contact solutions.
- AFM based indentation is generally more experimentally challenging than nanoindenter based indentation, however the AFM approach allows for the extraction of properties from a much smaller length scale.
- High levels of non-monotonic drift present in both the nanoindenter and the atomic force microscope limit the measurement of long term viscoelastic properties with this approach.
- The cement paste and ostensibly the C-S-H has a higher measured Young's modulus on the tens of nanometers length scale (AFM obtained) than on the hundreds of nanometers length scale (nanoindenter obtained).
- The observed distribution of Young's modulus when measured with AFM appears distinct in shape from the nanoindenter obtained values.
- The viscoelastic Young's modulus measured with nanoindentation appears to be trimodally distributed.
- Analogous to the elastic results, the viscoelastic compliance measured with AFM shows less relaxation than the viscoelastic compliance measured with nanoindentation.
- Moisture level plays a role in the time dependent response of the cement paste, though measured viscoelasticity at low relative humidity levels indicate that moisture level, or fluid movement cannot be the only mechanism contributing to viscoelasticity in portland cement paste.

Future work

Though the findings of this research are interesting and significant, questions remain that pertain to this work. For example, some of the conclusions in the preceding section have been about identifying the most likely explanation for the phenomena observed in the experimental data. A natural next step would be to directly test the hypothesized explanations presented. Additional future work would include moving these findings forward within the context of multi-scale modeling.

Future experimental work

In this research, AFM based indentation has been performed for the first time on cementitious materials. More testing should be done to further validate and increase the statistical significance of the measured results from this study. Additionally, the controlled relative humidity testing should be continued and expanded to hopefully better define the trends presented in the results chapter. With more information regarding the influence of moisture on the elastic and viscoelastic properties of cement paste and C-S-H, greater insight into the deformation mechanisms may be obtained.

Other experimental work should also be initiated, in concert with modeling efforts, to validate the results obtained in this work. For example, simple beams could be constructed of the same material tested in this research, which could then be tested in simple flexure either elastically or time dependently. These results could then be compared to predictions generated that consider the presently obtained material properties. This experimental program would serve as a strong validation for the multi-

scale modeling approach and serve to illustrate the predictive power of this multi-scale approach.

Related to the testing and implementation of the multi-scale modeling, experimentation should be initiated to test the hypotheses presented as most likely conclusions in the preceding sections. By performing similar testing on pure C-S-H or paste obtained from reacting chemistry controlled cement, the presence of certain crystalline phases within the interacted volume of material can be reduced or controlled. This testing could help illuminate the discussion surrounding the source of the distribution of properties observed in indentation testing. If the distribution remains similar to the distribution obtained from the testing of ordinary portland cement, then the distinct packing densities in the context of the colloidal spheres model would be supported. On the other hand, if the distribution changes dramatically, then the contribution of the crystalline phases could be considered significant.

Finally, the experimental techniques initiated and mastered in this research are not limited to cementitious materials. Similar experiments could be performed on a host of other materials to investigate similar questions. Of particular interest are those materials that posses heterogeneity on the small length scales probed by nanoindentation and by AFM. Examples could include biological materials, nano-composites, or high performance, multiphase alloys.

Future modeling work

As alluded to above, the natural extension of this research would be the implementation of a multi-scale constitutive model for the mechanical properties of C-S-H, portland cement, and ultimately portland cement concrete. Related to this modeling, conclusions will need to be made regarding the structure of C-S-H in order for the AFM based indentation results to be incorporated into the model. This is due to the fact that the length scale represented by the AFM results is not well characterized structurally in C-S-H.

In addition to multi-scale modeling, careful modeling of the indentation experiment could lead to a better understanding of the nature of cement paste and C-S-H. Similar to the experimental work discussed above, virtual nanoindentation experiments could be conducted with realistic cement paste microstructures. These microstructures could be obtained from serial x-ray computed tomography or from a three dimensional hydration model such as Hymostruc. These microstructures should be considered representative of the microstructure of the cement paste and the results obtained from virtual nanoindentation testing will help to elucidate the discussion surrounding the distribution of mechanical properties obtained from nanoindentation. As above, if the distribution obtained matches the results obtained from real testing, then the hypotheses of Ulm and coworkers would be supported while a significant deviation from the experimental distributions should be seen as a support of the hypotheses of Lura.

REFERENCES

[1] Lomborg B. The skeptical environmentalist: measuring the real state of the world. Cambridge, MA: Cambridge University Press; 2001.

[2] Gillott JE. Review of expansive alkali-aggregate reactions in concrete. J Mater Civ Eng. 1995;7(4):278-82.

[3] Mehta PK. Durability of concrete - The zigzag course of progress. Indian Conc J. 2006;80(8):9-16.

[4] Tinnea J. Rebar corrosion. Mater Performance. 1987;26(12):9-11.

[5] Vitaliano DF. Infrastructure costs of road salting. Resour Conserv Recycl. 1992;7(1-3):171-80.

[6] Richardson IG. The calcium silicate hydrates. Cem Concr Res. 2008;38(2):137-58.

[7] Abrams D. Design of concrete mixtures. Chicago: Structural Materials Research Laboratory, Lewis Institute; 1919.

[8] Bentz D. CEMHYD3D: a three-dimensional cement hydration and microstructure development modelling package, version 2.0. Gaithersberg, MD 2000.

[9] Bullard JW, Garboczi EJ. A model investigation of the influence of particle shape on portland cement hydration. Cem Concr Res. 2006;36(6):1007-15.

[10] Ganneau FP, Ulm FJ, Gondzio J, Garboczi EJ. An algorithm for computing the compressive strength of heterogeneous cohesive-frictional materials - Application to cement paste. Computers and Geotechnics. 2007;34(4):254-66.

[11] Garboczi EJ, Douglas JF, Bohn RB. A hybrid finite element-analytical method for determining the intrinsic elastic moduli of particles having moderately extended shapes and a wide range of elastic properties. Mechanics of Materials. 2006;38(8-10):786-800.

[12] Garboczi EJ, Haecker CJ, Bullard JW, Bohn RB, Sun Z, Shah SP, et al. Modeling the linear elastic properties of Portland cement paste. Cem Concr Res. 2005;35(10):1948-60.

[13] Zhihui S, Garboczi EJ, Shah SP. Modeling the elastic properties of concrete composites: experiment, differential effective medium theory, and numerical simulation. Cem Concr Compos. 2007;29(1):22-38.

[14] Yang T, Keller B, Magyari E. AFM investigation of cement paste in humid air at different relative humidities. Journal of Physics D: Applied Physics. 2002;35(8):25-8.

[15] Saez De Ibarra Y, Gaitero JJ, Erkizia E, Campillo I. Atomic force microscopy and nanoindentation of cement pastes with nanotube dispersions. Physica Status Solidi (A) Applications and Materials. 2006;203(6):1076-81.

[16] Mondal P, Shah SP, Marks LD. Use of atomic force microscopy and nanoindentation for characterization of cemetitious materials at the nanoscale. 254 ed. Denver, CO: American Concrete Institute; 2008. p. 41-56.

[17] Graham MA, Grasley ZC, Abu al-Rub RK. The effect of atomic force microscope probe size on nanoindentation. International Journal of Materials and Structural Integrity. 2010(4):2-3.

[18] Clifford CA, Seah MP. Quantification issues in the identification of nanoscale regions of homopolymers using modulus measurement via AFM nanoindentation. Applied Surface Science. 2005;252(5):1915-33.

[19] Ulm FJ, Vandamme M, Bobko C, Alberto Ortega J, Tai K, Ortiz C. Statistical indentation techniques for hydrated nanocomposites: concrete, bone, and shale. J Am Ceram Soc. 2007;90(9):2677-92.

[20] Bobko C, Ulm F-J. The nano-mechanical morphology of shale. Mechanics of Materials.40(4-5):318-37.

[21] Velez K, Maximilien S, Damidot D, Fantozzi G, Sorrentino F. Determination by nanoindentation of elastic modulus and hardness of pure constituents of Portland cement clinker. Cem Concr Res. 2001;31(4):555-61.

[22] VanLandingham M, Villarrubia J, Guthrie W, Meyers G. Nanoindentation of polymers: An overview. Advances in Scanning Probe Microscopy of Polymers Macromolecular Symposia2001. p. 15-44.

[23] Nemecek J, Smilauer V, Kopecky L, Nemeckova J. Nanoindentation of alkali activated fly ash. Transportation Research Record. 2010;1(2141):36-40.

[24] Chandler MQ, Peters JF, Pelessone D. Modeling nanoindentation of calcium silicate hydrate. Transportation Research Record. 2010;2(2142):67-74.

[25] Chen JJ, Sorelli L, Vandamme M, Ulm F-J, Chanvillard G. A coupled nanoindentation/SEM-EDS study on low water/cement ratio portland cement paste: Evidence for C-S-H/Ca(OH)2 nanocomposites. J Am Ceram Soc. 2010;93(5):1484-93.

[26] Mondal P, Shah SP, Marks LD. Use of atomic force microscopy and nanoindentation for characterization of cemetitious materials at the nanoscale. ACI SP. 2008;254:41-56.

[27] Hughes JJ, Trtik P. Micro-mechanical properties of cement paste measured by depth-sensing nanoindentation: A preliminary correlation of physical properties with phase type. EMABM 2003: 9th Euroseminar on Microscopy Applied to Building Materials 2-4 ed. Trondheim, Norway: Elsevier Inc.; 2004. p. 223-31.

[28] Nemecek J, Kopecky L, Bittnar Z. Size effect in nanoindentation of cement paste. International Conference on Applications of Nanotechnology in Concrete Design. Dundee, Scotland: Thomas Telford Services Ltd; 2005. p. 47-53.

[29] Sorelli L, Constantinides G, Ulm F-J, Toutlemonde F. The nano-mechanical signature of Ultra High Performance Concrete by statistical nanoindentation techniques. Cem Concr Res. 2008;38(12):1447-56.

[30] Zhu W, Hughes JJ, Bicanic N, Pearce CJ. Nanoindentation mapping of mechanical properties of cement paste and natural rocks. Materials Characterization. 2007;58(11-12 SPEC. ISS.):1189-98.

[31] Jennings H. A model for the microstructure of calcium silicate hydrate in cement paste. Cem Concr Res. 2000;30(1):101-16.

[32] Jennings H. Colloid model of C-S-H and implications to the problem of creep and shrinkage. Materials and Structures. 2004;37(1):59-70.

[33] Tennis PD, Jennings HM. Model for two types of calcium silicate hydrate in the microstructure of Portland cement pastes. Cem Concr Res. 2000;30(6):855-63.

[34] Constantinides G, Ulm F-J. The effect of two types of C-S-H on the elasticity of cement-based materials: Results from nanoindentation and micromechanical modeling. Cem Concr Res. 2004;34(1):67-80.

[35] Jennings HM, Thomas JJ, Gevrenov JS, Constantinides G, Ulm F-J. A multi-technique investigation of the nanoporosity of cement paste. Cem Concr Res. 2007;37(3):329-36.

[36] Ulm FJ, Constantinides G. The nanogranular nature of C-S-H. J Mech Phys Solids. 2007;55(1):64-90.

[37] Trtik P, Munch B, Lura P. A critical examination of statistical nanoindentation on model materials and hardened cement pastes based on virtual experiments. Cem Concr Compos. 2009;31(10):705-14.

[38] Ulm F-J, Vandamme M, Jennings HM, Vanzo J, Bentivegna M, Krakowiak KJ, et al. Does microstructure matter for statistical nanoindentation techniques? Cem Concr Compos. 2010;32(1):92-9.

[39] Chen JJ, Sorelli L, Vandamme M, Ulm FJ, Chanvillard G. A Coupled Nanoindentation/SEM EDS Study on Low Water/Cement Ratio Portland Cement Paste: Evidence for C–S–H/Ca (OH) 2 Nanocomposites. J Am Ceram Soc. 2010;93(5):1484-93.

[40] Scherer GW. Characterization of saturated porous bodies. Mater Struct. 2004;37(265):21-30.

[41] Jennings HM. Colloid model of C-S-H and implications to the problem of creep and shrinkage. Mater Struct. 2004;37(265):59-70.

[42] Grasley Z, Lange D. The viscoelastic response of cement paste to three-dimensional loading. Mechanics of Time-Dependent Materials. 2007;11(1):27-46.

[43] Pichler C, Lackner R. A multiscale creep model as basis for simulation of early-age concrete behavior. Computers and Concrete. 2008;5(4):295-328.

[44] Jones CA, Grasley ZC. Short-term creep of cement paste during nanoindentation. Cem Concr Compos. 2010;33(1):12-8.

[45] Powers T. Mechanisms of shrinkage and reversible creep of hardened cement paste. International Conference on the Structure of Concrete: Cement & Concrete Association of Great Britain; 1968. p. 319.

[46] Feldman RF. Mechanism of creep of hydrated Portland cement paste. Cem Concr Res. 1972;2(5):521-40.

[47] Jennings H. Colloid model of C- S- H and implications to the problem of creep and shrinkage. Materials and Structures. 2004;37(1):59-70.

[48] Alizadeh R, Beaudoin JJ, Raki L. Viscoelastic nature of calcium silicate hydrate. Cem Concr Compos. 2010;32(5):369-76.

[49] Vandamme M. The Nanogranular origin of concrete creep: a nanoindentation investigation of microstructure and fundamental properties of calcium-silicate-hydrates. Boston, Massachusetts Institute of Technology; 2008.

[50] Ulm FJ, Constantinides G, Heukamp FH. Is concrete a poromechanics material? - A multiscale investigation of poroelastic properties. Mater Struct. 2004;37(265):43-58.

[51] Sellevold EJ, Richards CW. Short-time creep transition for hardened cement paste. J Am Ceram Soc. 1972;55(6):284-9.

[52] Scherer GW. Measuring permeability of rigid materials by a beam-bending method: I, Theory. J Am Ceram Soc. 2000;83(9):2231-9.

[53] Mindess S, Young JF, Darwin D. Concrete. Second ed. Upper Saddle River, NJ: Prentice Hall; 2003.

[54] Ulm FJ, Vandamme M. Viscoelastic solutions for conical indentation. Int J Solids Struct. 2006;43(10):3142-65.

[55] Vandamme M, Ulm F-J. Nanogranular origin of concrete creep. Proceedings of the National Academy of Sciences. 2009;106(26):10552-7.

[56] Nemecek J. Creep effects in nanoindentation of hydrated phases of cement pastes. Materials Characterization. 2009;60(9):1028-34.

[57] Cheng L, Xia X, Scriven L, Gerberich W. Spherical-tip indentation of viscoelastic material. Mechanics of Materials. 2005;37(1):213-26.

[58] Cheng L, Xia X, Yu W, Scriven L, Gerberich W. Flat-punch indentation of viscoelastic material. Journal of Polymer Science Part B Polymer Physics. 2000;38(1):10-22.

[59] Cheng Y, Cheng C. Relationships between initial unloading slope, contact depth, and mechanical properties for conical indentation in linear viscoelastic solids. Journal of Materials Research. 2005;20(4):1046-53.

[60] Seltzer R, Mai Y. Depth sensing indentation of linear viscoelastic-plastic solids: A simple method to determine creep compliance. Engineering Fracture Mechanics. 2008;75(17):4852-62.

[61] Fischer-Cripps AC. A simple phenomenological approach to nanoindentation creep. Materials Science and Engineering A. 2004;385(1-2):74-82.

[62] Garas V, Jayapalan AR, Kahn LF, Kurtis KE. Multi-scale investigation of the effect of thermal treatment on the tensile creep of ultra-high performance concrete: Preliminary assessment. International Journal of Materials and Structural Integrity. 2009;3(2-3):187-200.

[63] Garas VY, Jayapalan AR, Kahn LF, Kurtis KE. Micro- and nanoscale characterization of effect of interfacial transition zone on tensile creep of ultra-high-performance concrete. Transportation Research Record. 2010(2141):82-8.

[64] Mondal P, Shah SP, Marks L. A reliable technique to determine the local mechanical properties at the nanoscale for cementitious materials. Cem Concr Res. 2007;37(10):1440-4.

[65] Constantinides G, Ulm FJ, Van Vliet K. On the use of nanoindentation for cementitious materials. Mater Struct. 2003;36(257):191-6.

[66] Lura P, Trtik P, Münch B. Validity of recent approaches for statistical nanoindentation of cement pastes. Cem Concr Compos. 2011;33(4):457-65.

[67] Powers T. The physical structure in portland cement paste. The Chemistry of Cements. 1964.

[68] Ulm F-J, Vandamme M, Jennings HM, Vanzo J, Bentivegna M, Krakowiak KJ, et al. Does microstructure matter for statistical nanoindentation techniques? Cem Concr Compos.32(1):92-9.

[69] Jennings HM. Model for the microstructure of calcium silicate hydrate in cement paste. Cem Concr Res. 2000;30(1):101-16.

[70] Jennings H. Refinements to colloid model of CSH in cement: CM-II. Cem Concr Res. 2008;38(3):275-89.

[71] Haecker CJ, Garboczi EJ, Bullard JW, Bohn RB, Sun Z, Shah SP, et al. Modeling the linear elastic properties of Portland cement paste. Cem Concr Res. 2005;35(10):1948-60.

[72] Kim J, Balogun O, Shah S. Atomic Force Acoustic Microscopy to Measure Nanoscale Mechanical Properties of Cement Pastes. Transportation Research Record: Journal of the Transportation Research Board. 2010;2141(-1):102-8.

[73] Mondai P, Shah SR, Marks LD. Nanoscale characterization of cementitious materials. ACI Materials Journal. 2008;105(2):174-9.

[74] Plassard C, Lesniewska E, Pochard I, Nonat A. Investigation of the surface structure and elastic properties of calcium silicate hydrates at the nanoscale. Ultramicroscopy. 2004;100(3-4):331-8.

[75] Shi X, Zhao Y-P. Comparison of various adhesion contact theories and the influence of dimensionless load parameter. Journal of Adhesion Science and Technology. 2004;18(1):55-68.

[76] Zhihui S, Voigt T, Shah SP. Rheometric and ultrasonic investigations of viscoelastic properties of fresh Portland cement pastes. Cem Concr Res. 2006;36(2):278-87.

[77] Grasley ZC, Lange DA. Constitutive modeling of the aging viscoelastic properties of portland cement paste. Mechanics of Time-Dependent Materials. 2007;11(3-4):175-98.

[78] Feldman RF, Sereda PJ. A new model for hydrated Portland cement and its practical implications. Engineering Journal. 1970;53(8-9):53-9.

[79] Feldman RF, Sereda P. A model for hydrated Portland cement paste as deduced from sorption-length change and mechanical properties. Materials and Structures. 1968;1(6):509-20.

[80] Hertz H. On the contact of elastic solids. J Reine Angew Math. 1881;92:156-71.

[81] Galin L, Sneddon I, Moss H. Contact problems in the theory of elasticity. Raleigh: Dept. of Mathematics, North Carolina State College; 1961.

[82] Sneddon IN. Relation between load and penetration in axisymmetric Boussinesq problem for punch of arbitrary profile. International Journal of Engineering Science. 1965;3:47-57.

[83] Jones J. On the determination of molecular fields. II. From the equation of state of a gas. Proceedings of the Royal Society of London Series A, Containing Papers of a Mathematical and Physical Character. 1924:463-77.

[84] Carnie SL, Torrie GM. The statistical mechanics of the electrical double layer. 1984.

[85] Johnson KL, Kendall K, Roberts AD. Surface energy and the contact of elastic solids. Proceedings of the Royal Society of London Series A, Mathematical and Physical Sciences. 1971;324(1558):301-13.

[86] Derjaguin BV, Muller VM, Toporov YP. Effect of contact deformations on the adhesion of particles. J Colloid Interface Sci. 1975;53(2):314-26.

[87] Paul B, Abadan I. Contact geometry associated with arbitrary rail and wheel profiles. Annual Meeting of the American Society of Mechanical Engineers. Chicago: ASME; 1980. p. 93.

[88] Paul B, Hashemi J. Contact pressures on closely conforming elastic bodies. Journal of Applied mechanics. 1981;48:543.

[89] Kalker J, Van Randen Y. A minimum principle for frictionless elastic contact with application to non-Hertzian half-space contact problems. Journal of Engineering Mathematics. 1972;6(2):193-206.

[90] Attard P, Parker JL. Deformation and adhesion of elastic bodies in contact. Physical Review A 1992;46(12):7959-71.

[91] Attard P. Interaction and deformation of elastic bodies: Origin of adhesion hysteresis. Journal of Physical Chemistry B. 2000;104(45):10635-41.

[92] Attard P. Interaction and deformation of viscoelastic particles. 2. Adhesive particles. Langmuir. 2001;17(14):4322-8.

[93] Attard P. Interaction and deformation of viscoelastic particles: Nonadhesive particles. Physical Review E. 2001;63(6):61604.

[94] Attard P. Measurement and interpretation of elastic and viscoelastic properties with the atomic force microscope. Journal of Physics: Condensed Matter. 2007;19:473201.

[95] Johnson K. The correlation of indentation experiments. J Mech Phys Solids. 1970;18(2):115-26.

[96] Johnson K. One hundred years of Hertz contact. Archive: Proceedings of the Institution of Mechanical Engineers 1847-1982 (vols 1-196). 1982;196(1982):363-78.

[97] Oliver W, Pharr G. Improved technique for determining hardness and elastic modulus using load and displacement sensing indentation experiments. Journal of Materials Research. 1992;7(6):1564-83.

[98] Fuller K, Tabor D. The effect of surface roughness on the adhesion of elastic solids. Proceedings of the Royal Society of London Series A, Mathematical and Physical Sciences. 1975;345(1642):327-42.

[99] Tabor D. Surface forces and surface interactions. J Colloid Interface Sci. 1977;58(1):2-13.

[100] Lee EH, Radok JRM. Contact problem for viscoelastic bodies. Journal of Applied Mechanics Series E. 1960;27(3):438-44.

[101] Radok J. Visco-elastic stress analysis. Quarterly of Applied Mathematics. 1957;15:198-202.

[102] Lakes R. The time-dependent Poisson’s ratio of viscoelastic materials can increase or decrease. Cell Polym. 1992;11:466–9.

[103] Lakes RS, Wineman A. On poisson's ratio in linearly viscoelastic solids. Journal of Elasticity. 2006;85(1):45-63.

[104] Bazant Z. Theory of creep and shrinkage in concrete structures: A precis of recent developments. Mechanics today. 1975;2:1-93.

[105] Gopalakrishnan K, Neville A, Ghali A. Creep Poisson's ratio of concrete under multiaxial compression. Journal of the American Concrete Institute. 1969;66.

[106] Hannant D. Creep and creep recovery of concrete subjected to multiaxial compressive stress. Journal of the American Concrete Institute. 1969;66.

[107] Jordaan I, Illston J. The creep of sealed concrete under multiaxial compressive stresses. Mag Conc Res. 1969;21(69):195-204.

[108] Jordaan I, Illston J. Time-dependent strains in sealed concrete under multiaxial compressive stress. Mag Conc Res. 1971;23:75-6-9-88.

[109] Bernard O, Ulm F, Germaine J. Volume and deviator creep of calcium-leached cement-based materials. Cem Concr Res. 2003;33(8):1127-36.

[110] Grasley ZC, Scherer GW, Lange DA, Valenza JJ. Dynamic pressurization method for measuring permeability and modulus: II. cementitious materials. Mater Struct. 2007;40(7):711-21.

[111] Jones CA. Hollow Cylinder Dynamic Pressurization and Radial Flow Through Permeability Tests for Cementitous Materials. College Station, Texas A&M University; 2008.

[112] Stehfest H. Numerical inversion of Laplace transforms. Commun of the ACM. 1970;13(1):47-9.

[113] Kjellsen KO, Monsøy A, Isachsen K, Detwiler RJ. Preparation of flat-polished specimens for SEM-backscattered electron imaging and X-ray microanalysis--importance of epoxy impregnation. Cem Concr Res. 2003;33(4):611-6.

[114] AXS B. Dimension Icon Atomic Force Microsocope with ScanAsyst. In: http://www.bruker-axs.com/typo3temp/pics/95fdf0e334.jpg, editor. Karlsruhe, Germany2011.

[115] Bazant Z, Chern J. Concrete creep at variable humidity: constitutive law and mechanism. Materials and Structures. 1985;18(1):1-20.

[116] Nohava J, Randall N, Conte N. Novel ultra nanoindentation method with extremely low thermal drift: Principle and experimental results. Journal of Materials Research. 2009;24(3):873-82.

[117] Cardona M, Chamberlin RV, Marx W. The history of the stretched exponential function. Annalen der Physik. 2007;16(12):842-5.

[118] Vichit-Vadakan W, Scherer GW. Measuring permeability and stress relaxation of young cement paste by beam bending. Cem Concr Res. 2003;33(12):1925-32.

[119] Nemecek J, Kopecky L, Bittnar Z. Size effect in nanoindentation of cement paste. Dundee, Scotland: Thomas Telford Services Ltd; 2005. p. 47-53.

[120] Oehlert GW. A note on the delta method. The American Statistician. 1992;46(1):27-9.

[121] Beaudoin JJ, Alizadeh R. A discussion of the paper "A multi-technique investigation of the nanoporosity of cement paste" by Hamlin M. Jennings, Jeffrey J. Thomas, Julia S. Gevrenov, Georgios Constantinides and Franz-Josef Ulm. Cem Concr Res. 2007;37(9):1373-.

[122] Pellenq RJ-M, Vandamme H. Why does concrete set?: the nature of cohesion forces in hardened cement-based materials. Warrendale, PA, ETATS-UNIS: Materials Research Society; 2004.

[123] Fonseca P. Nanoindentation Simulations to Predict Macroscale Properties of Cement. TMS Annual Meeting. Seattle, WA Minerals, Metals and Materials Society/AIME; 2010.

[124] Shahsavari R, Buehler MJ, Pellenq RJM, Ulm FJ. First principles study of elastic constants and interlayer interactions of complex hydrated oxides: case study of tobermorite and jennite. J Am Ceram Soc. 2009;92(10):2323-30.

[125] Jones CA, Grasley ZC. Correlation of hollow and solid cylinder dynamic pressurization tests for measuring permeability. Cem Concr Res. 2009;39(4):345-52.

[126] Scherer GW, Valenza JJ, II, Simmons G. New methods to measure liquid permeability in porous materials. Cem Concr Res. 2007;37(3):386-97.

[127] Scherer GW. Dynamic pressurization method for measuring permeability and modulus: I. Theory. Mater Struct. 2006;39(294):1041-57.

[128] Vichit-Vadakan W, Scherer GW, Grutzeek M. Measuring permeability of rigid materials by a beam-bending method: III, cement paste. J Am Ceram Soc. 2002;85(6):1537-44.

[129] Scherer GW. Thermal expansion kinetics: method to measure permeability of cementitious materials. I. Theory. J Am Ceram Soc. 2000;83(11):2753-61.

APPENDIX A

MATLAB CODE FOR THE IMPLEMENTATION OF ATTARD'S SELF CONSISTENT METHOD

This appendix is the Matlab code used for the self consistent numerical modeling of the AFM contact. The code uses one subroutine, roundcone.m that allows for the consideration of a rounded cone with a specified tip radius and cone half angle. The self consistent code will be presented first followed by the subroutine. The model uses nanometers as the base measure of length, which requires the conversion of various model parameters such as stiffness or stress.

AttardElastic.m

```
%% ELASTIC ATTARD CONTACT MODEL
%   This script calculates the interaction between to bodies in contact
%   based on realistic surface forces. The approach is based on the
%   work of Attard and Parker (1992) and Attard (2000, 2001).
%
%  Author:
%    Mike Graham
%    mikegraham@gmail.com


%%
```

```
clear
clc


%% SET THE VALUE OF PARAMETERS


% MATERIAL PARAMETERS
%
%  Effective modulus
E = 30 * 10^(9-18); %N/nm^2  =  Exapascals = 10^18 Pa
%
%
% Here is the pressure function p(h).
%==Exponential-Expoential Potential==
% P_attract = 12 * 10^(6-18); %Exapascals
% kappa_attract = 1.0; % 1/(nm)
% P_repulse = 60 * 10^(6-18); %Exapascals
% kappa_repulse = 2.0; % 1/(nm)
%
% pressure = @(h) P_repulse * exp(-kappa_repulse*h) ...
%              - P_attract * exp(-kappa_attract*h);
%
```

```
%==Lennard-Jones adhesion==
% A = 10^(-19 + 9); %nJ = N * nm, Hammicker's constant
% z0 = 1.0; %nm
% pressure = @(h) A/6/pi./h.^3 .* ((z0 ./ h).^6 - 1);
%
%==Exponential repulsion==
Pr = 250 * 10^(6-18); %EPa
kr = 5; %nm
pressure = @(h)  Pr * exp(-kr * h);
%
%
% GEOMETRIC AND SIMULATION PARAMETERS
%
% The history of the _position_ h_0 through the simulation at step.
%step = 0.05;
%h0 = [5:step:-5 -5:step:5];
h0=importdata('h0data.txt');
%
%
% Specify the profile function
profilefun = @(r) roundcone(r, 90, 40);
%
```

```
% The maximum radius to consider (in place of infinity. The point at
% which no deformation is expected).
maximum_radius = 400; %nm
%
% The number of grid points for the spatial integration.
meshnum = 25;
%
% The maxiumum blending parameter for self-consistent blending. It is
% the greatest proportion to which the new trial solution is introduced.
% Smaller is more stable.
maxblend = 0.01;
%
% The error tolerance, which is the largest RMS value that two trials'
% predictions for the new deformation profile can vary.
maxerror = 0.001;  %1pm



%% INITIALISE AND CALCULATE NEEEDED VARIABLES
%
% Set up the time parameters.
num_time_steps = length(h0);
%
```

```
%
% This just allocates a lot of arrays, for speed.
u = zeros(meshnum, num_time_steps);
u_inf = zeros(meshnum, num_time_steps);
pdot = zeros(meshnum, num_time_steps);
udot = zeros(meshnum, num_time_steps);
h = zeros(meshnum, num_time_steps);
integralp = zeros(meshnum, 1);
integralpdot = zeros(meshnum, 1);
udotnew = zeros(meshnum, 1);
F = zeros(1, num_time_steps);
u0 = zeros(1, num_time_steps);
%
% Make the points in the radii. %nm
radius = linspace(0, maximum_radius, meshnum);
dr = radius(2);
radius = radius + dr/2;
%
% This is the profile for the undeformed shape, i.e. round (for radius
% values much smaller than the effective radius of the solids.)
profile = profilefun(radius');
%
```

```
% The initial separation should be the initial undeformed separation.
h(:,1) = h0(1) + profile;
%
Deltah0 = diff(h0);
%
Delta_u0_trial = 0;



%% COMPUTE THE KERNEL
% The kernel is used to perform the pressure-force relation (Attard 2001,
% Eq. 2) and arises from the enforcement of axisymmetry
% (Attard and Parker 1992, 15).
kernel = zeros(meshnum, meshnum);
for r = 1:meshnum
for s = 1:meshnum
  % For the special case that the dummy variable equals the radius value,
  % the elliptic integral is unbounded and we have to calculate the
  % kernel using the limit from each side (Attard 2001).
  if s==r
    Iminus = (dr/pi - dr^2/4/pi/radius(r)) ...
          * (1 + log(16*radius(r)^2/(radius(r)*dr - dr^2/4)) );
    Iplus  = dr/4*log(16*(radius(r)+dr/2)^2/(radius(r)*dr + dr^2/4))...
```

```
            + 4*radius(r)/pi*log((2*radius(r)+dr)/(2*radius(r)+dr/2));
    kernel(r,s) = (Iminus+Iplus)/radius(r)/dr;
    break
  else
    % Compute the kernel normally. Since it is symmetric k(r,s) = k(s,r),
    % we only do half of it and the break above keeps us from seeing the
    % case s>r.
    kernel(r,s) = 4/pi/radius(r) * ellipke((radius(s)/radius(r))^2);
    kernel(s,r) = kernel(r,s);
  end
end
end



%% MAIN SIMULATION
for t = 2:num_time_steps
  err = Inf;


  u(:,t) = 0.5 * ( (h0(t) + profile) - h(:,t-1) );


  c = 0;
```

```
blend = maxblend;

while err > maxerror

 % Calculate the separation (for finding the pressure and pressure
 % derivative), based on Attard and Parker (1992) Eqs. (17) and (18).
 h(:,t) = h0(t) + profile - u(:,t);

 % This is the main equation! (Attard 2000) Eq (11)
 %   u(r) = int( p(s) k(r,s) s ds, 0, inf)
 for r = 1:meshnum
  integralp(r) = sum(pressure(h(:,t)) .* kernel(:,r) .* radius(:)) * dr;
 end
 unew  = -2/E * integralp(:);

 % Self-consistent blending:
 u_old = u(:,t);
 u(:,t) = (1 - blend) * u(:,t) + blend * unew(:);
 u0(t) = (3 * u(1,t) - u(2,t)) / 2;

 % Calculate the error
 if c > 5000
```

```
    error('Convergence judged unlikely')
  elseif c > 0
    err = norm(u(:,t) - unew) / meshnum;
  end
  [t h0(t) err c/100];
  c = c + 1;

  % Decrease the blending ratio if we have oscillation or error
  % growth (Attard 2000).
  Delta_u0_old = Delta_u0_trial;
  Delta_u0_trial = u0(t) - u0(t-1);
  if (Delta_u0_trial * Delta_u0_old) < 0
    blend = blend / 1.5;
%   elseif abs(Delta_u0_trial) > abs(Delta_u0_old)
%     blend = blend / 1.2;
  elseif c > 0
    blend = min(1.3 * blend, maxblend);
  end

%   subplot(2,2,4,'replace');
%     plot(radius, h(:,t), 'r', radius,h0(t)+profile, 'b:')
%     title('Rigid and Deformed profiles')
```

```
%       xlabel('Radial Coordinate')
%       ylabel('Separation, Position')
%       axis([0 500 0 12])

  end

  % Integrate the pressure to find the load. [Attard and Parker (1992), (20)].
  %   F = 2pi int(p(r) r dr, r=0, r=inf) %should be Newtons (N)
  F(t) = 2 * pi * sum(pressure(h(:,t)) .* radius(:)) * dr;

end

delta = 2*u(1,:);
P=importdata('Pdata.txt');

  figure(1)
  subplot(2,2,1,'replace')
    plot(radius, h(:,t), 'r', radius,h0(t)+profile, 'b:')
    title('Rigid and Deformed profiles')
    xlabel('Radial Coordinate')
    ylabel('Separation, Position')
    axis([0 10 0 12])
```

```
subplot(2,2,2,'replace');
  plot(radius,h(:,1:t));
  title('h');
  set(get(gca,'YLabel'),'String','separation (nm)');
  set(get(gca,'XLabel'),'String','radial coordinate (nm)');
subplot(2,2,3,'replace');
  plot(radius,u(:,1:t));
  title('u');
  set(get(gca,'YLabel'),'String','displacement (nm)');
  set(get(gca,'XLabel'),'String','radial coordinate (nm)');
subplot(2,2,4,'replace');
  plot(radius,pressure(h(:,1:t)));
  title('p');
  set(get(gca,'YLabel'),'String','pressure (Pa)');
  set(get(gca,'XLabel'),'String','radial coordinate (nm)');

figure(2)
subplot(2,2,1,'replace');
  plot(F(1:t),-u(1,1:t));
  title('F-\delta');
  set(get(gca,'XLabel'),'String','force (N)');
  set(get(gca,'YLabel'),'String','center displacement (nm)');
```

```
  subplot(2,2,2,'replace');
    plot(h0(1:t),-u(1,1:t));
    title('deflection vs. position');
    set(get(gca,'XLabel'),'String','position (nm)');
    set(get(gca,'YLabel'),'String','center displacement (nm)');
  subplot(2,2,3,'replace');
    plot(h0(1:t),F(1:t),h0(1:t),P(1:t));
    title('Force vs. position');set(get(gca,'XLabel'),'String','position (nm)')
    set(get(gca,'YLabel'),'String','force (N)');



%data=[h0;F]';
%save data.txt data -ascii
```

APPENDIX B

NANOINDENTER TEST DATA

This appendix contains the test data from the creep nanoindentation tests. In the interest of saving space, five tests will be presented on each plot instead of plotting each test individually. In the nanoindentation testing program two tests were rejected due to erratic jumps or skips in the data. This could be attributed to breakage of the material or possibly isolated machine events. In total 44 tests were kept. The plots show creep displacement where the initial displacement from each test is subtracted from each data point to normalize all the data to zero at $t = 0^+$. The modality of the viscoelastic response is particularly noticeable in Figure B - 2,Figure B - 4, and Figure B - 9 where the creep displacement is separated into distinct response groups. For all the data presented, the effect of creep was subtracted from the response.

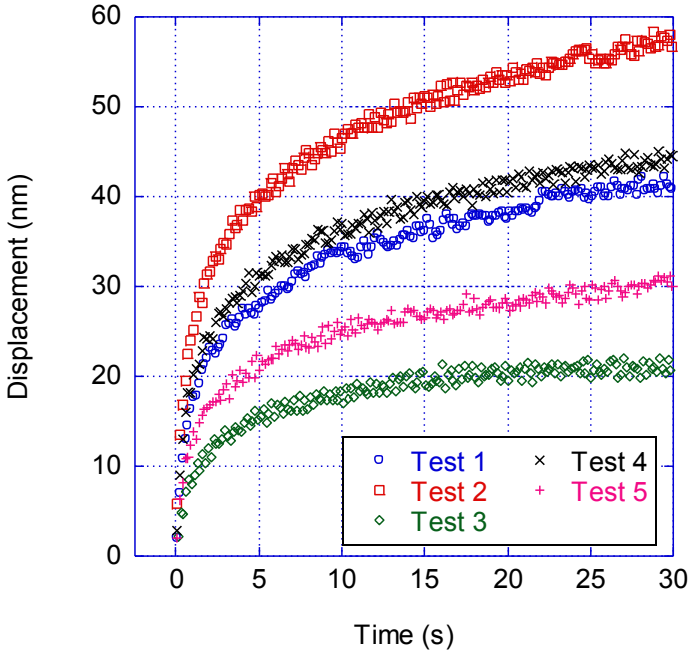

Figure B - 1: The creep displacement for the first five tests performed with the nanoindenter show significant time dependent relaxation of the material.

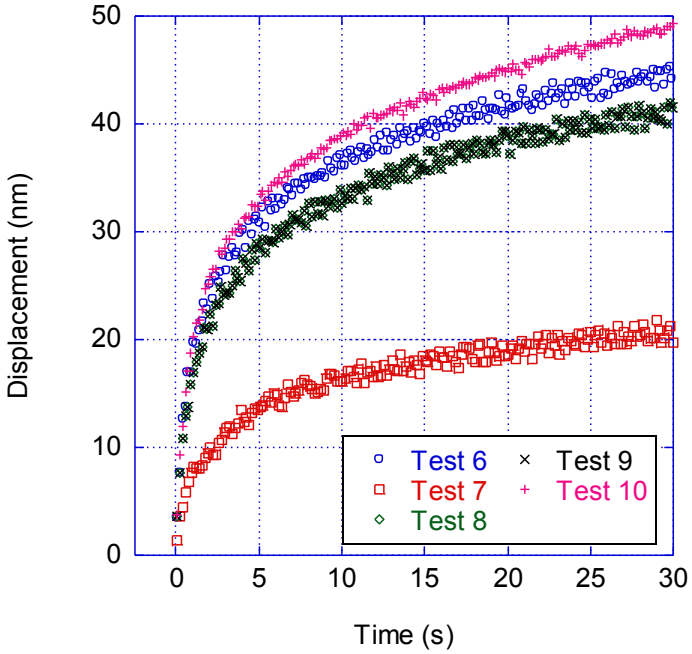

Figure B - 2: The creep displacement for tests 6-10 performed with the nanoindenter show significant time dependent relaxation of the material.

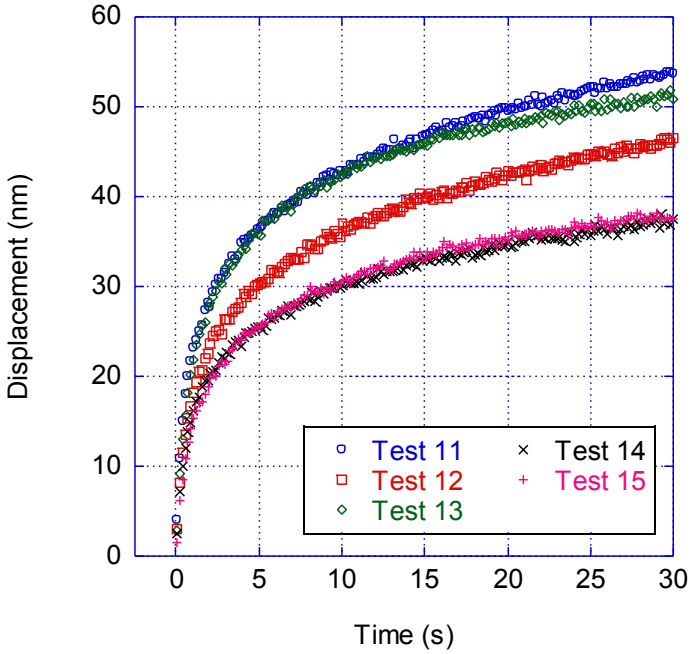

Figure B - 3: The creep displacement for tests 11-15 performed with the nanoindenter show significant time dependent relaxation of the material.

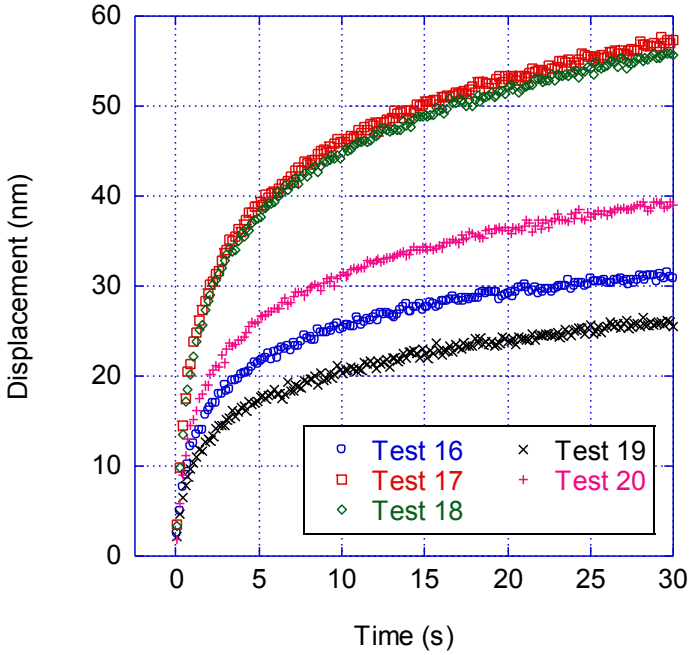

Figure B - 4: The creep displacement for tests 16-20 performed with the nanoindenter show significant time dependent relaxation of the material.

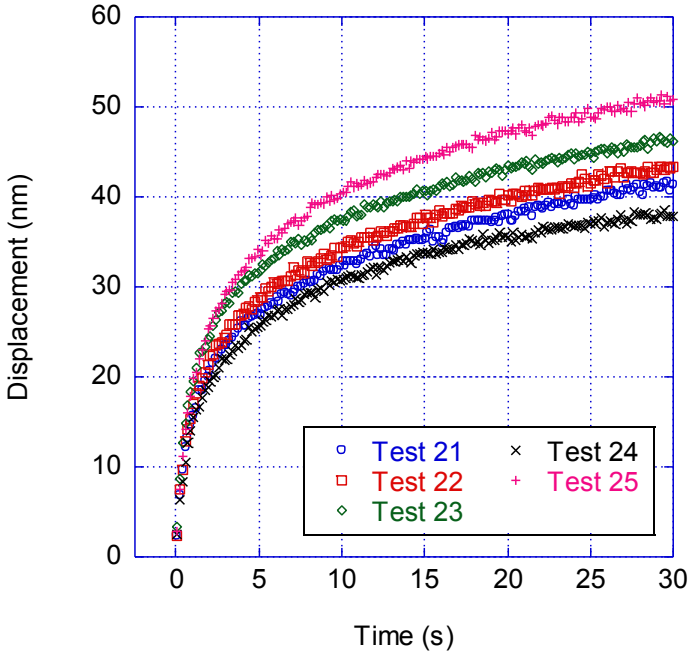

Figure B - 5: The creep displacement for tests 21-25 performed with the nanoindenter show significant time dependent relaxation of the material.

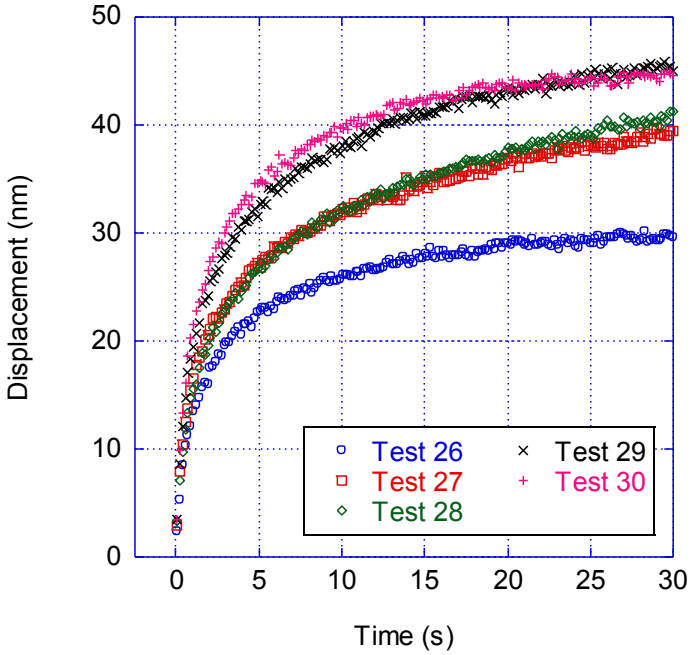

Figure B - 6: The creep displacement for tests 26-30 performed with the nanoindenter show significant time dependent relaxation of the material.

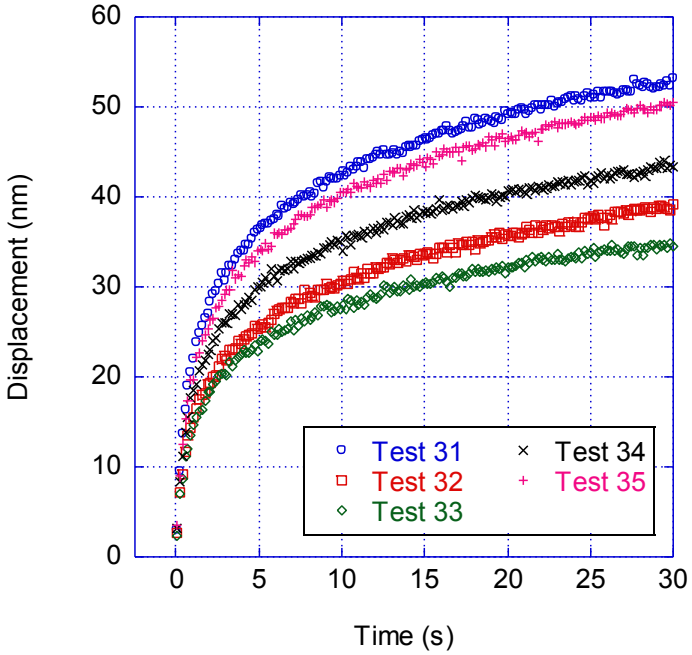

Figure B - 7: The creep displacement for tests 31-35 performed with the nanoindenter show significant time dependent relaxation of the material.

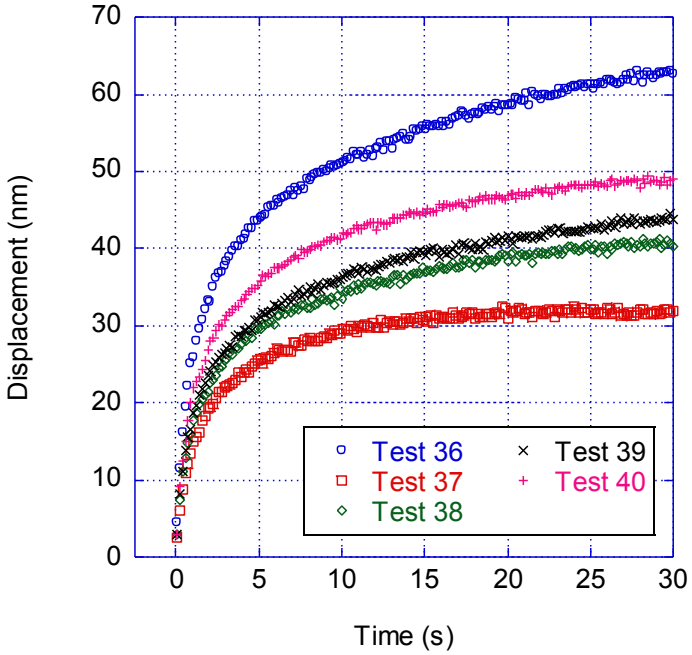

Figure B - 8: The creep displacement for tests 36-40 performed with the nanoindenter show significant time dependent relaxation of the material.

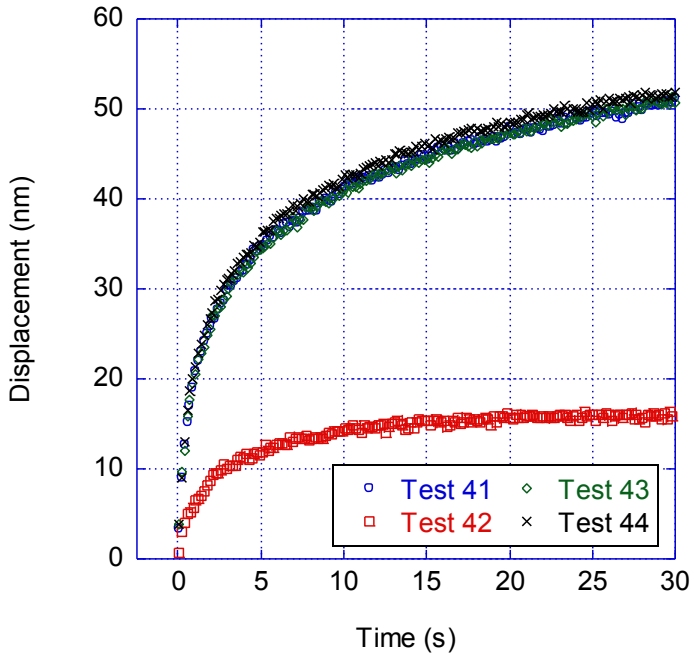

Figure B - 9: The creep displacement for tests 41-44 performed with the nanoindenter show significant time dependent relaxation of the material.

APPENDIX C

ATOMIC FORCE MICROSCOPE TEST DATA

The test results obtained from the atomic force microscope are presented in this appendix. The data are broken down into elastic test data and viscoelastic test data. The viscoelastic data are further broken down by the relative humidity level at which the test was conducted.

Elastic experimental data

The elastic indentation experiments performed with AFM were conducted at two different maximum force levels. The first twenty six tests were loaded at approximately $50\,\mu N$ while the remaining tests were loaded at approximately $20\,\mu N$.

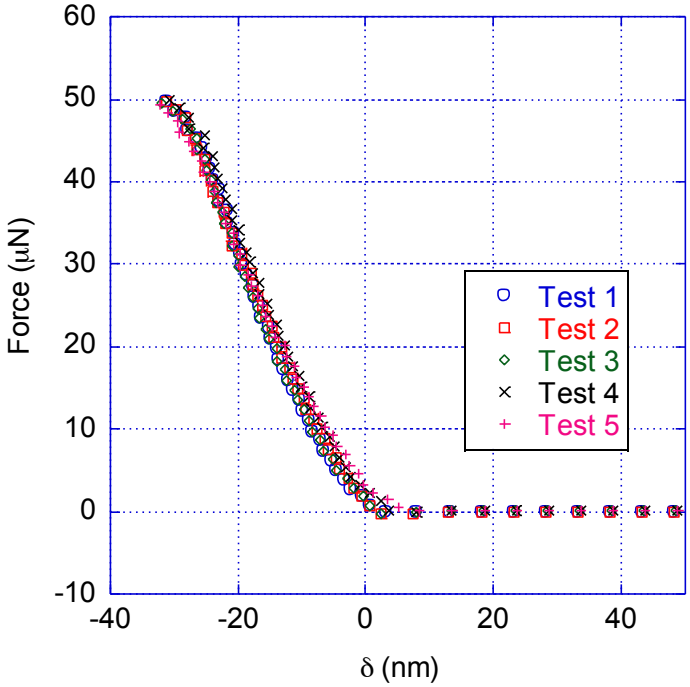

Figure C - 1: The elastic AFM based indentation tests 1-5.

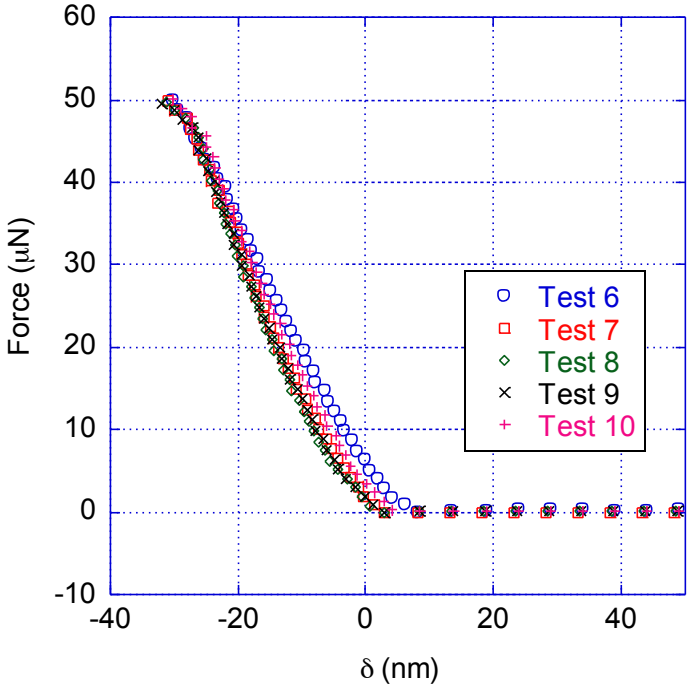

Figure C - 2: The elastic AFM based indentation tests 6-10.

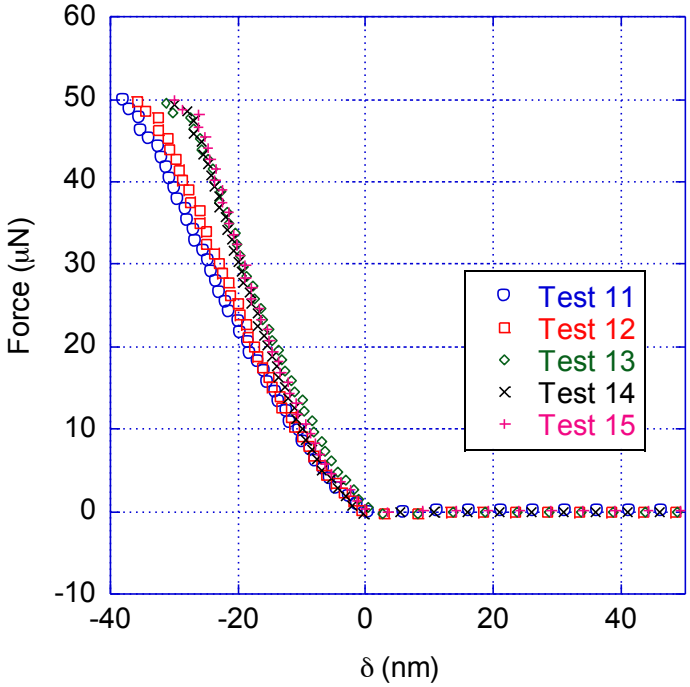

Figure C - 3: The elastic AFM based indentation tests 11-15.

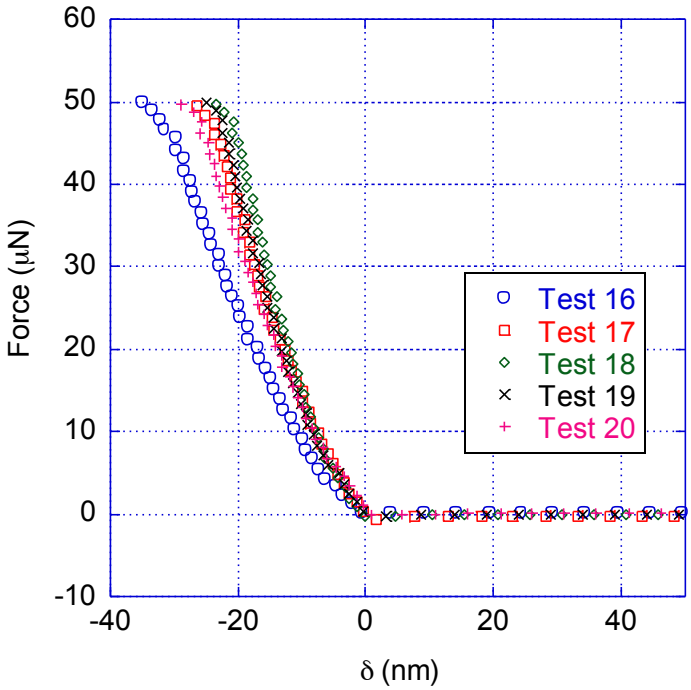

Figure C - 4: The elastic AFM based indentation tests 16-20.

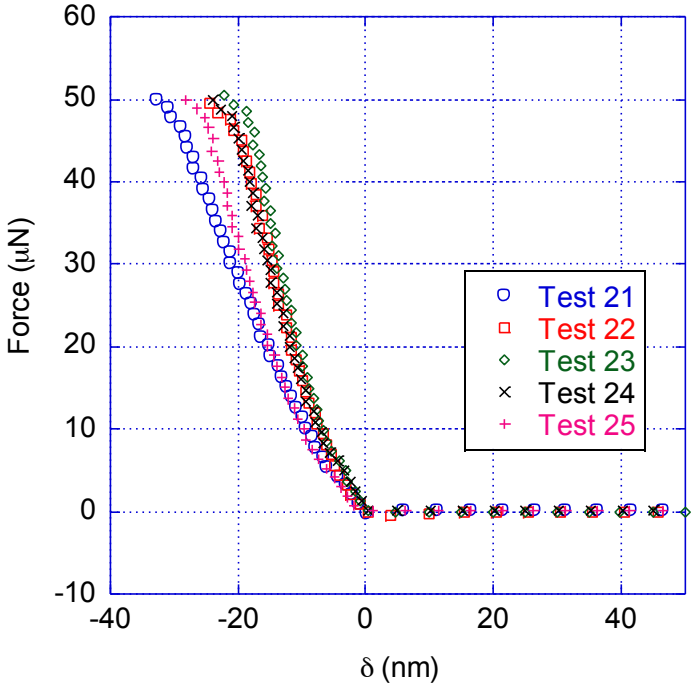

Figure C - 5: The elastic AFM based indentation tests 21-25.

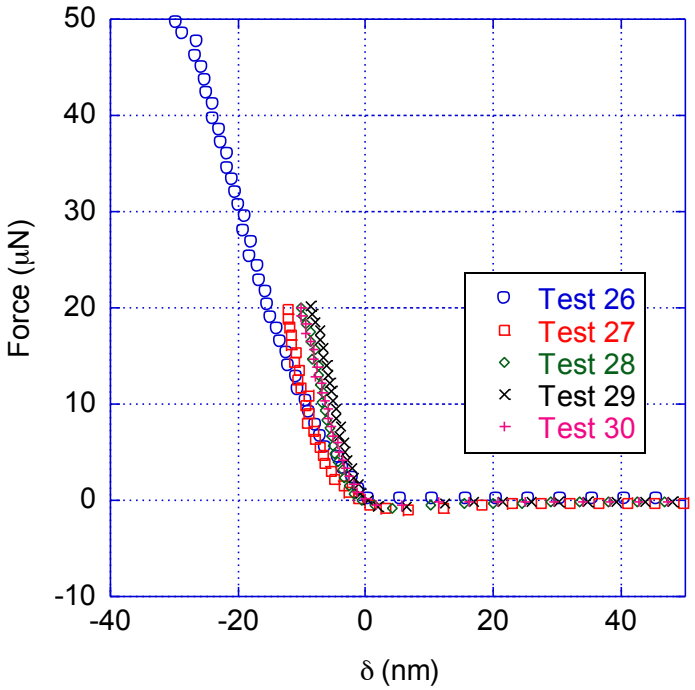

Figure C - 6: The elastic AFM based indentation tests 26-30.

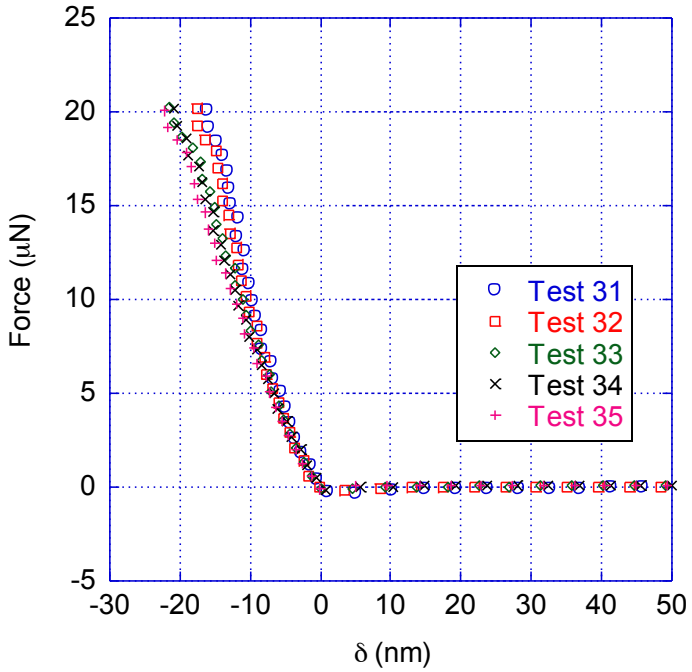

Figure C - 7: The elastic AFM based indentation tests 31-35.

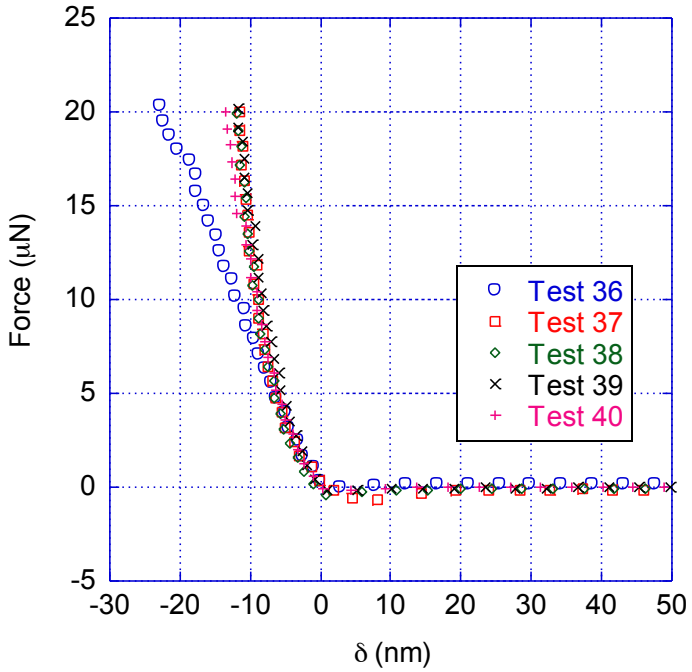

Figure C - 8: The elastic AFM based indentation tests 36-40.

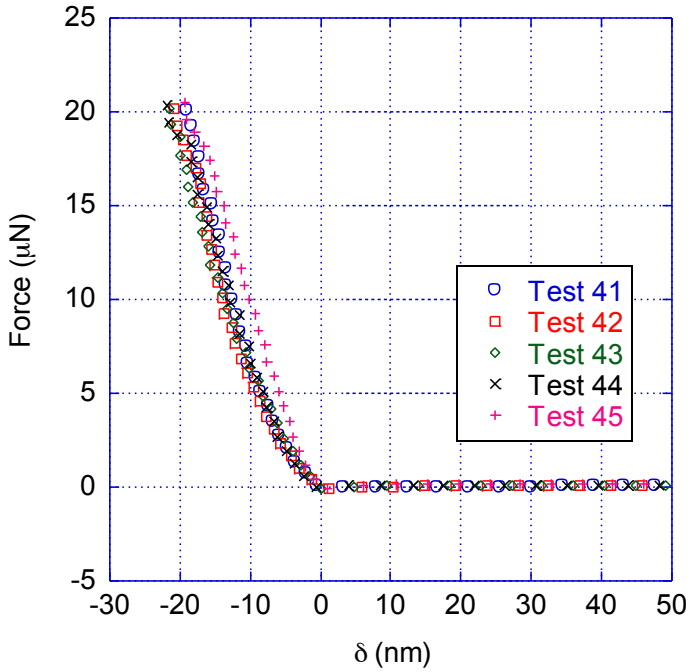

Figure C - 9: The elastic AFM based indentation tests 41-45.

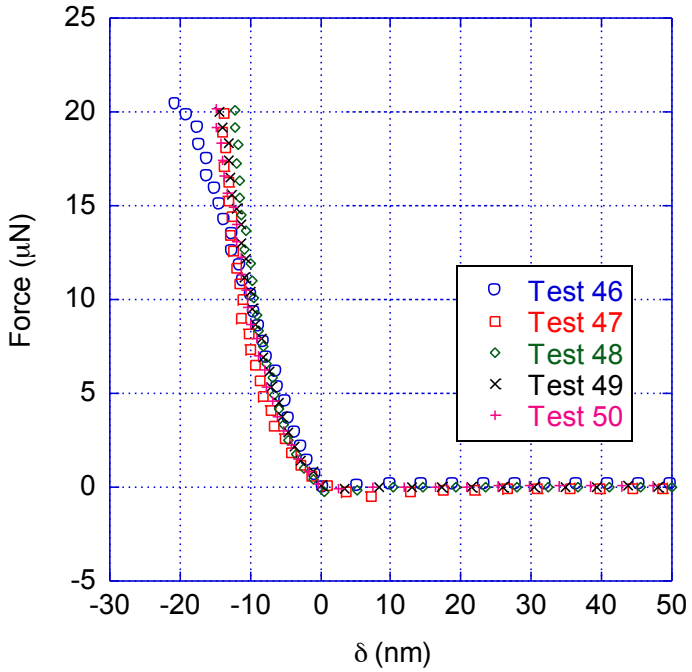

Figure C - 10: The elastic AFM based indentation tests 46-50.

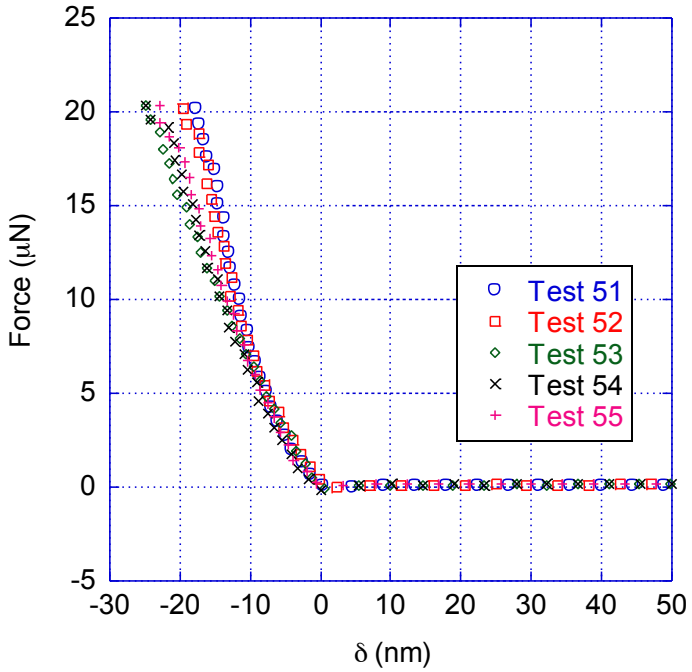

Figure C - 11: The elastic AFM based indentation tests 50-55.

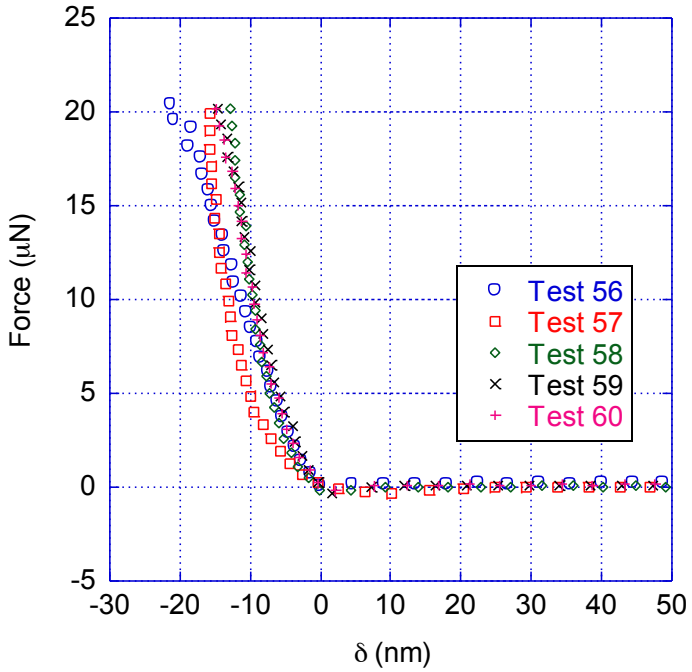

Figure C - 12: The elastic AFM based indentation tests 56-60.

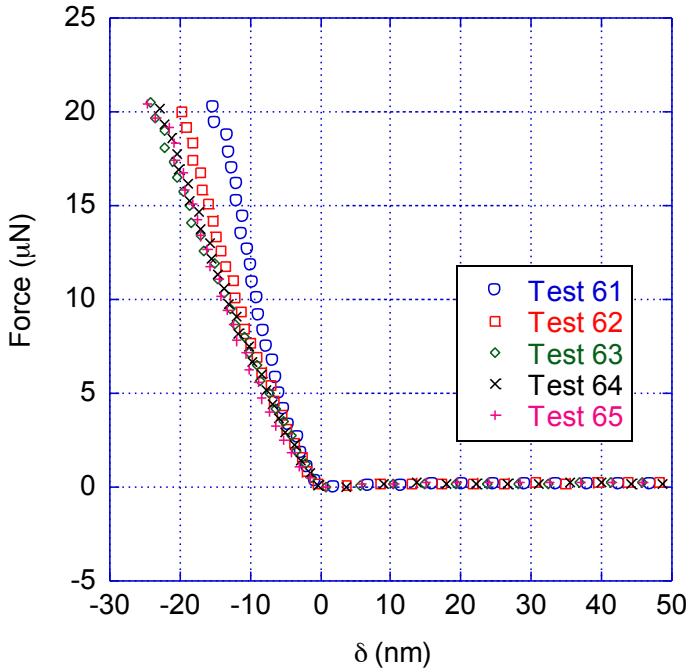

Figure C - 13: The elastic AFM based indentation tests 61-65.

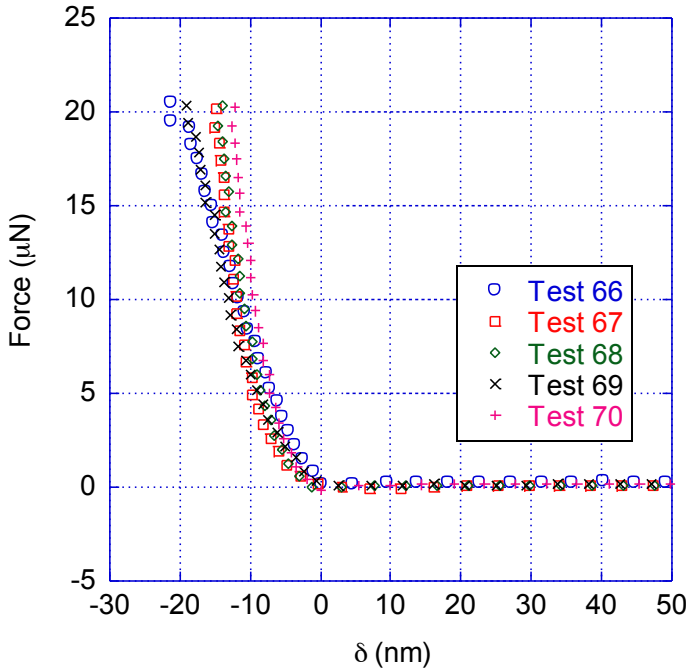

Figure C - 14: The elastic AFM based indentation tests 66-70.

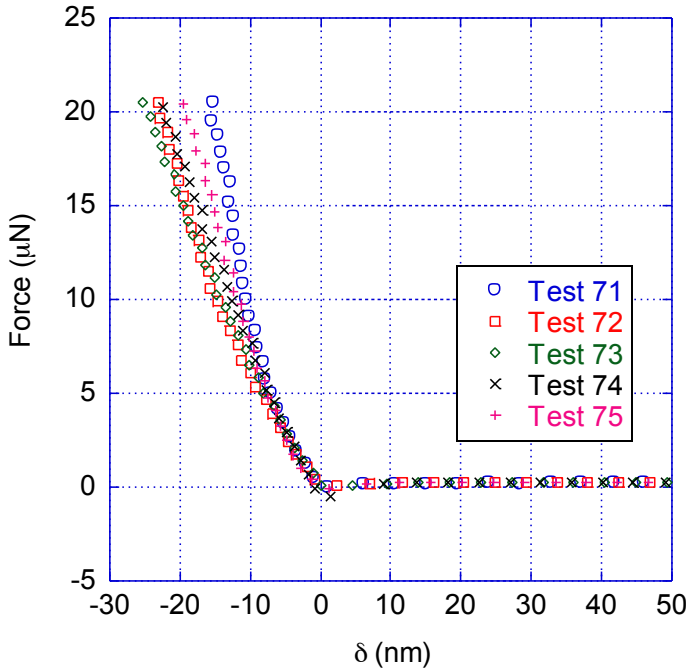

Figure C - 15: The elastic AFM based indentation tests 71-75.

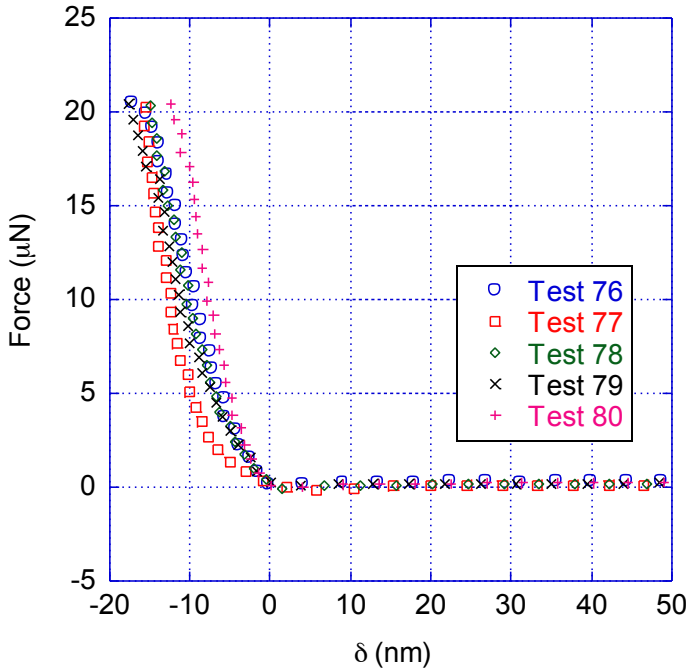

Figure C - 16: The elastic AFM based indentation tests 76-80.

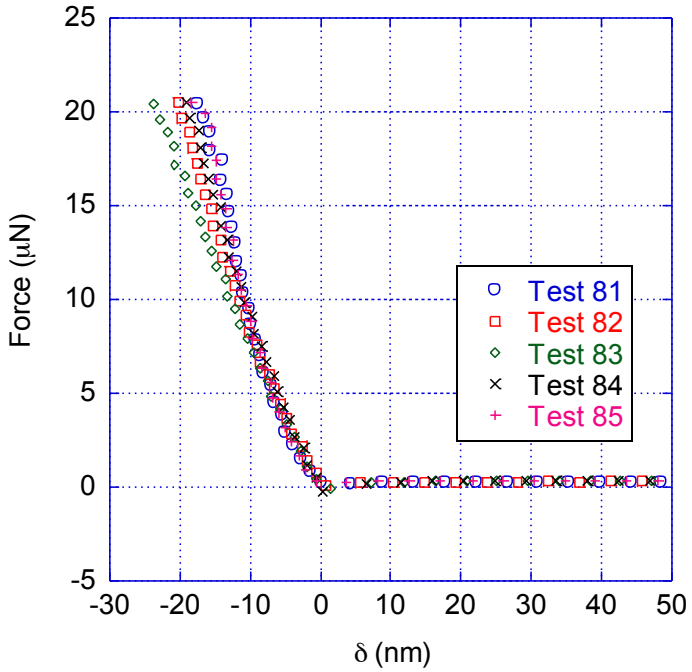

Figure C - 17: The elastic AFM based indentation tests 81-85.

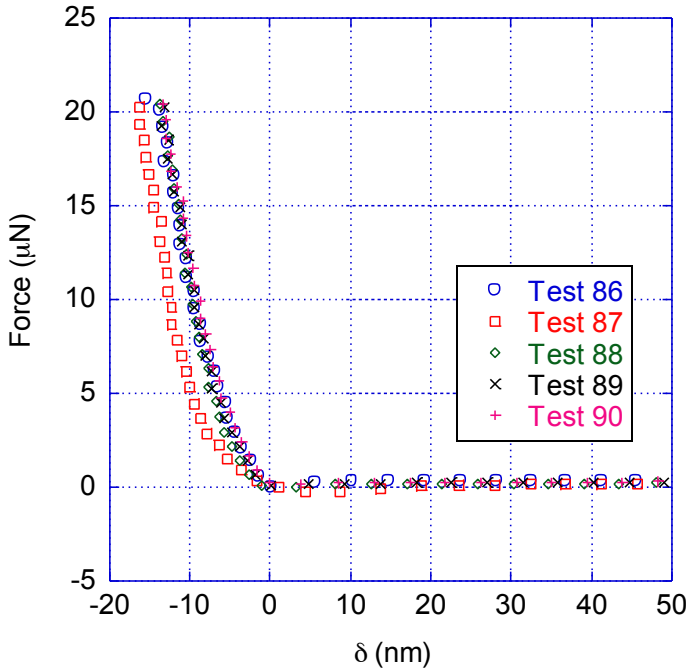

Figure C - 18: The elastic AFM based indentation tests 86-90.

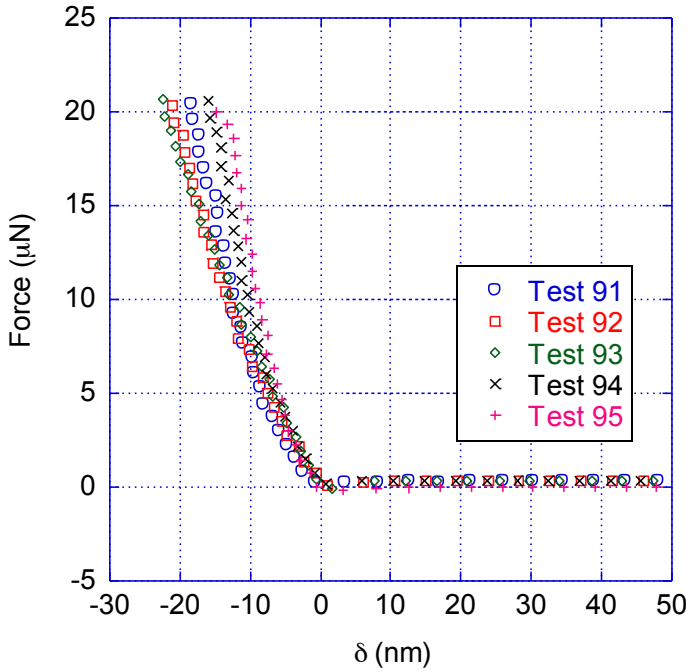

Figure C - 19: The elastic AFM based indentation tests 91-95.

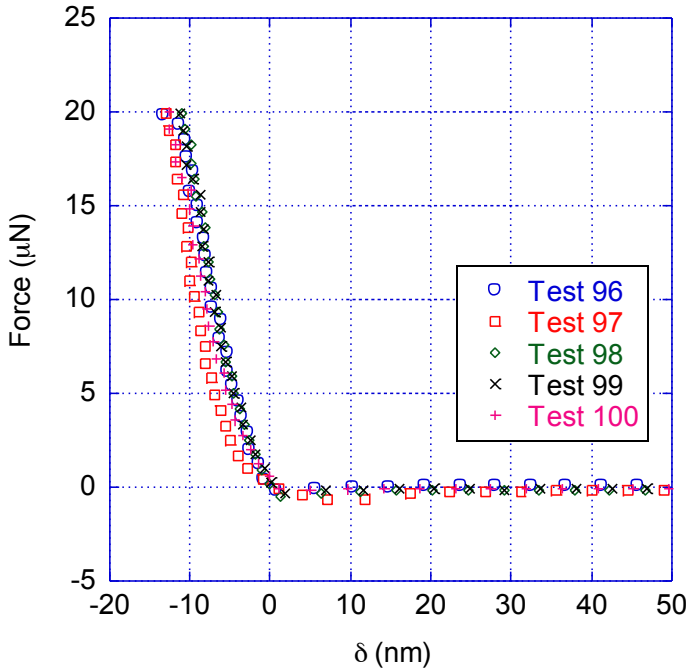

Figure C - 20: The elastic AFM based indentation tests 96-100.

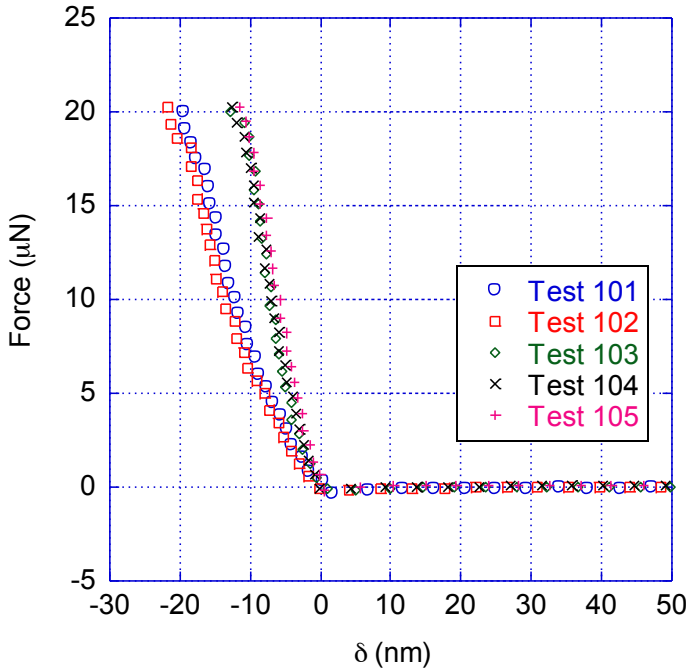

Figure C - 21: The elastic AFM based indentation tests 101-105.

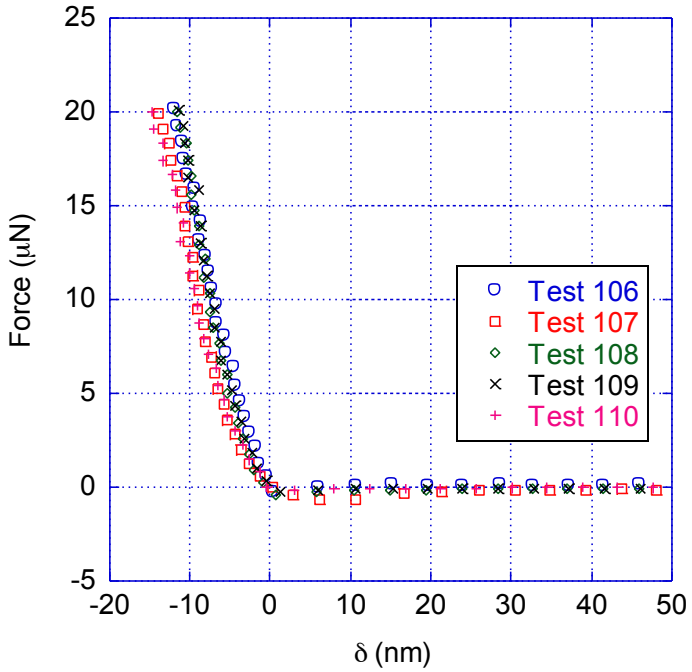

Figure C - 22: The elastic AFM based indentation tests 106-110.

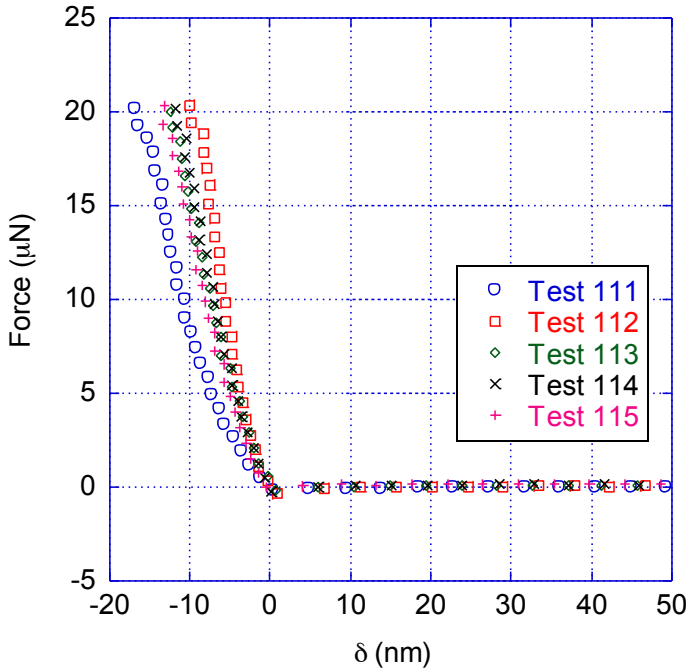

Figure C - 23: The elastic AFM based indentation tests 111-115.

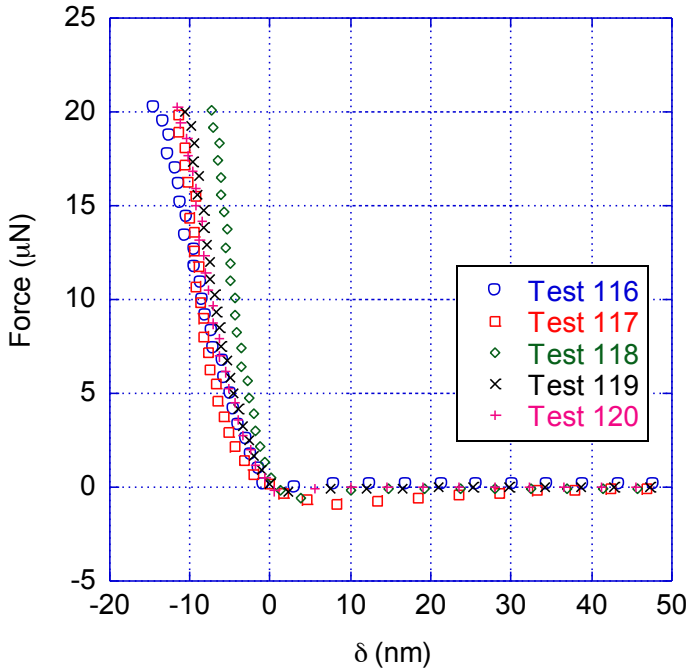

Figure C - 24: The elastic AFM based indentation tests 116-120.

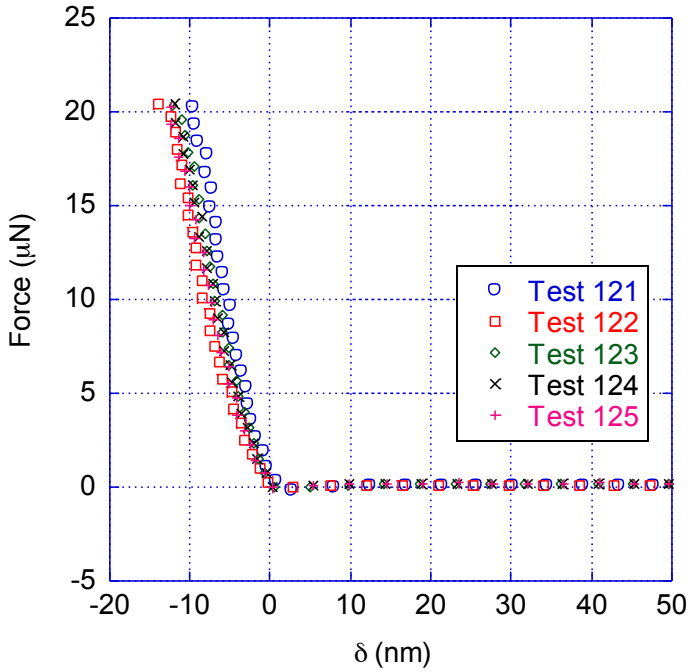

Figure C - 25: The elastic AFM based indentation tests 121-125.

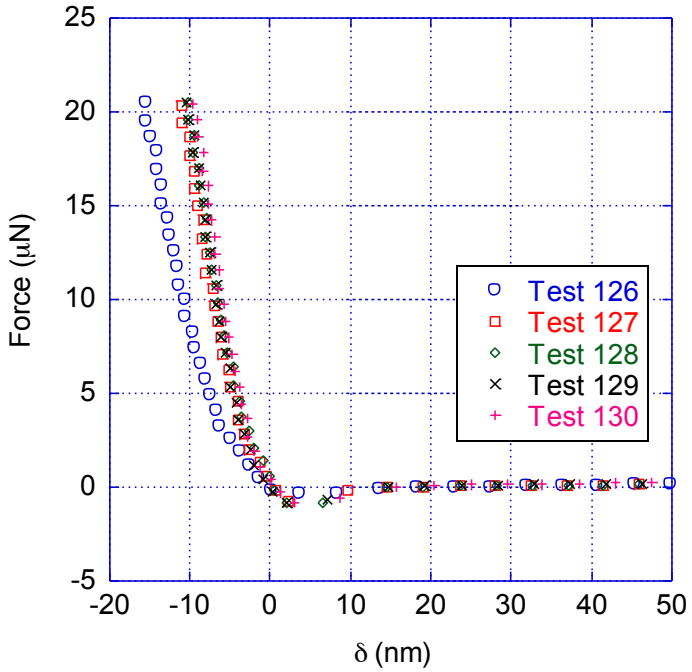

Figure C - 26: The elastic AFM based indentation tests 126-130.

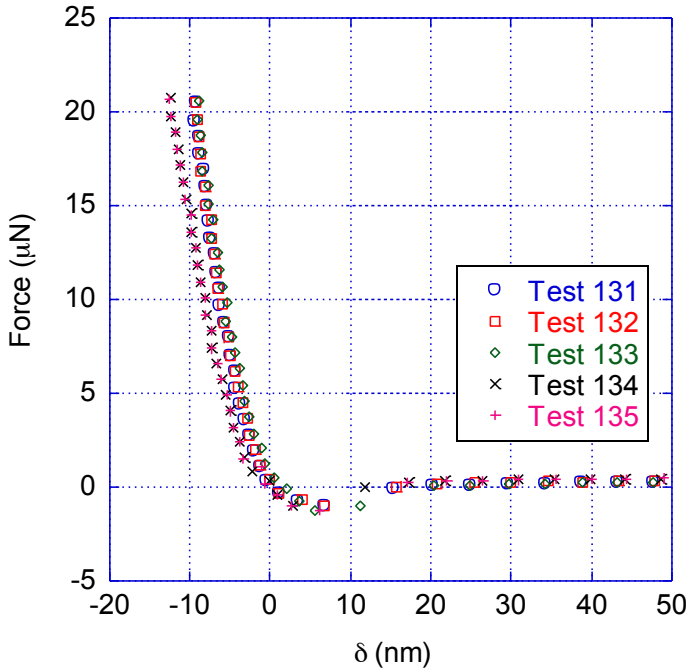

Figure C - 27: The elastic AFM based indentation tests 131-135.

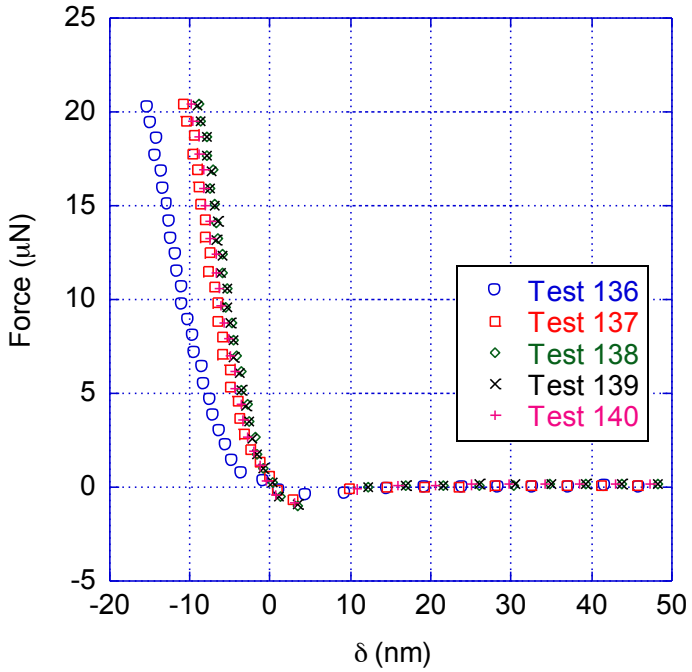

Figure C - 28: The elastic AFM based indentation tests 136-140.

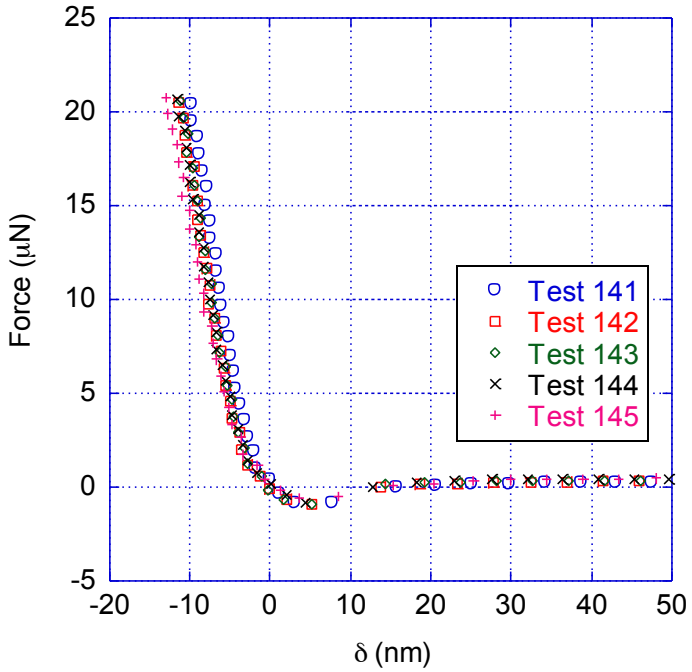

Figure C - 29: The elastic AFM based indentation tests 141-145.

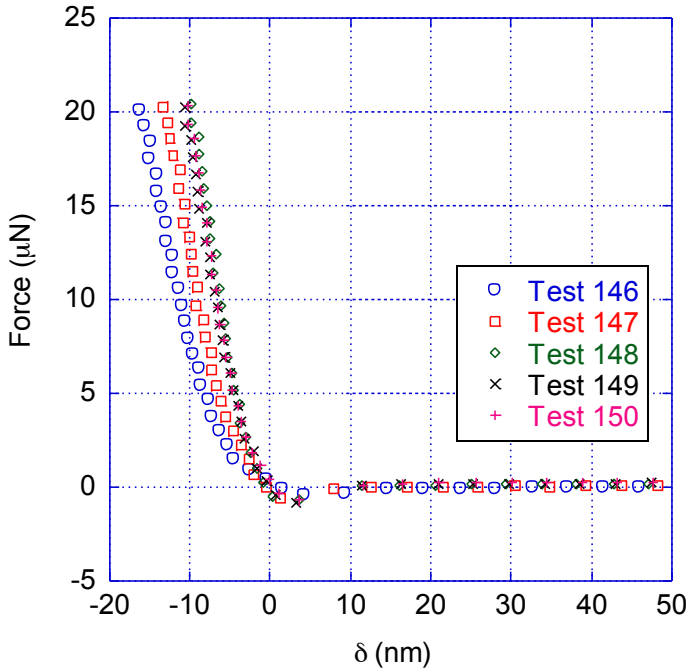

Figure C - 30: The elastic AFM based indentation tests 146-150.

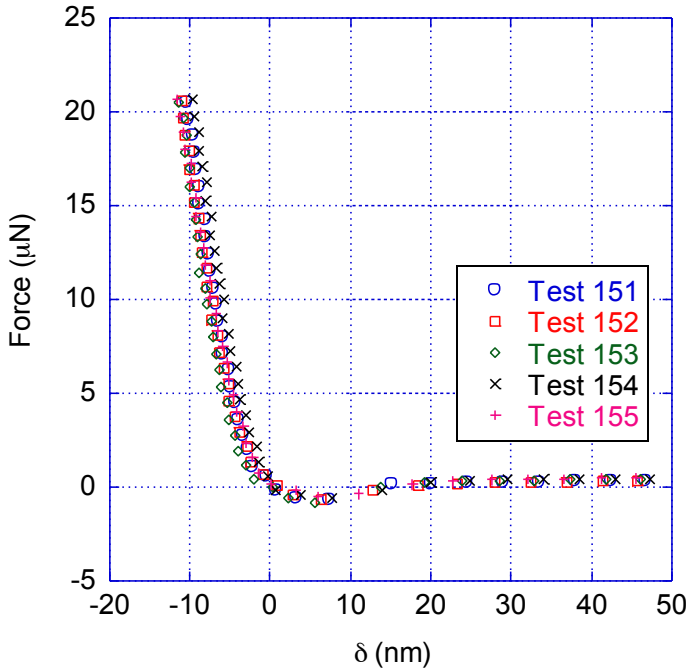

Figure C - 31: The elastic AFM based indentation tests 151-155.

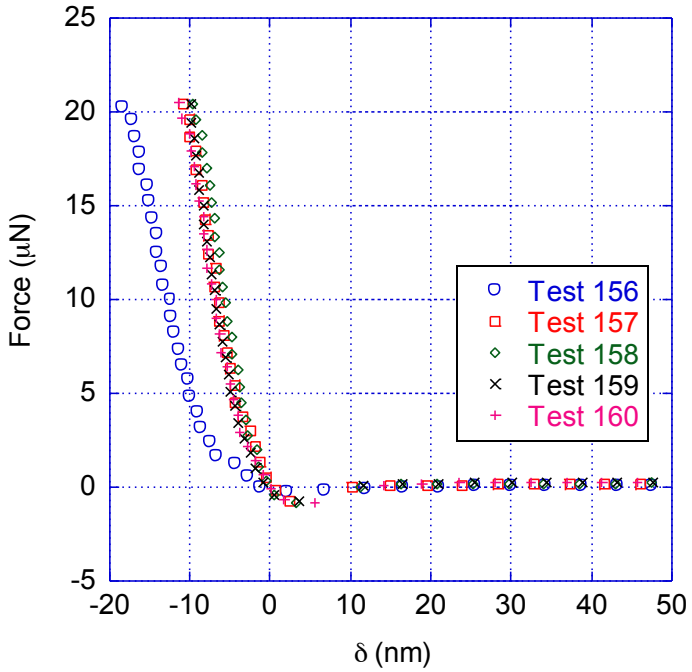

Figure C - 32: The elastic AFM based indentation tests 156-160.

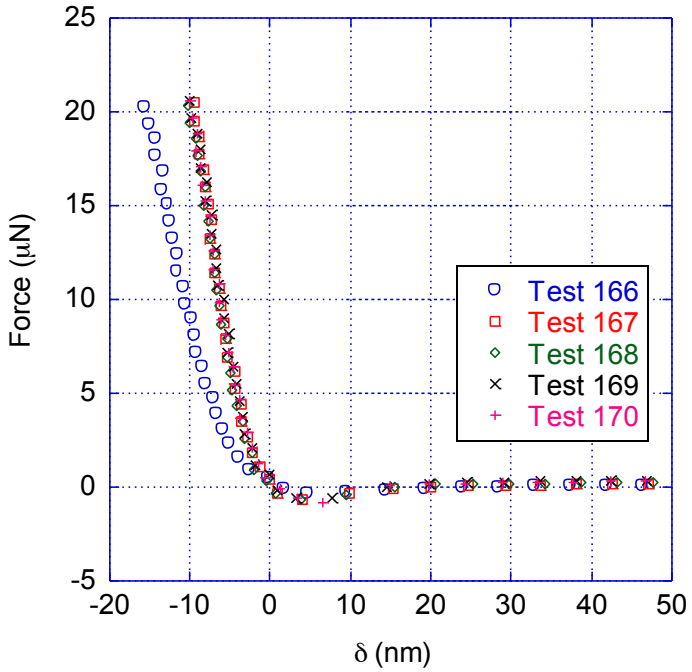

Figure C - 33: The elastic AFM based indentation tests 166-170.

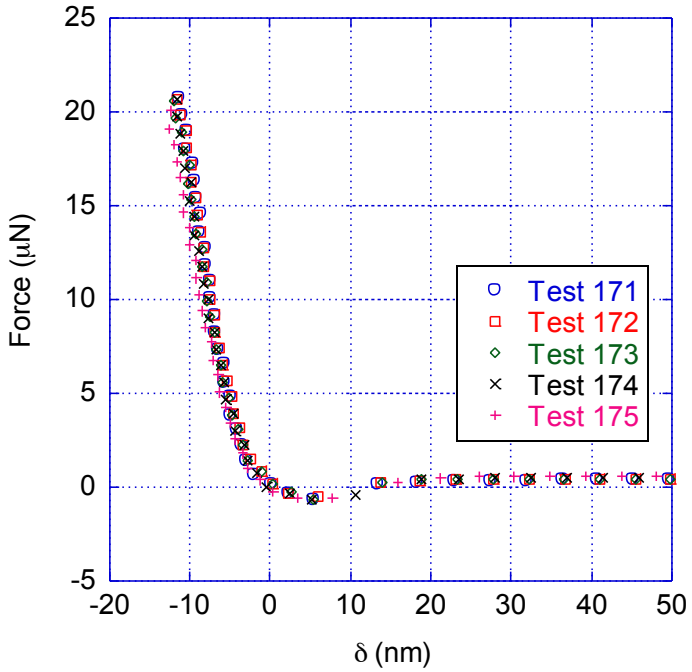

Figure C - 34: The elastic AFM based indentation tests 171-175.

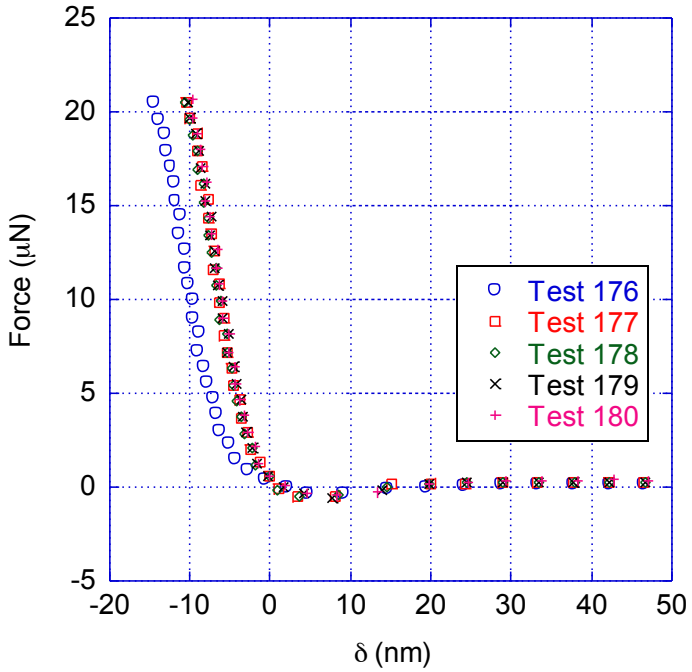

Figure C - 35: The elastic AFM based indentation tests 176-180.

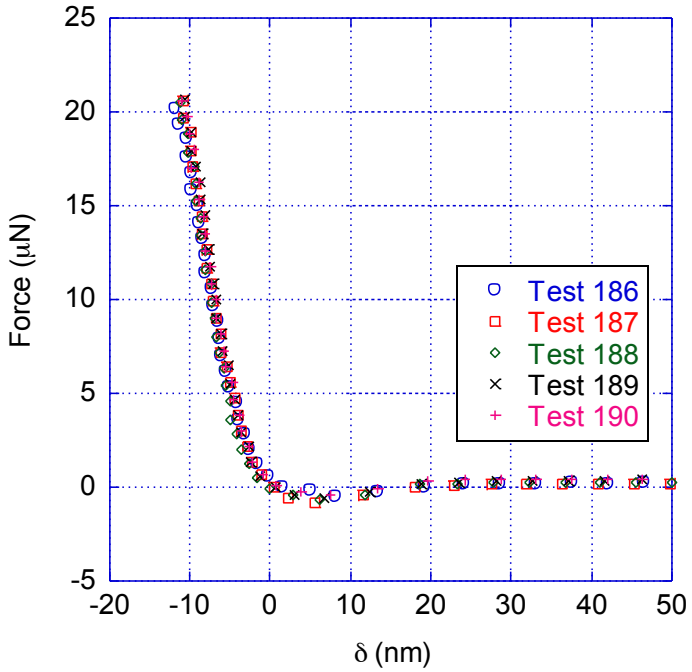

Figure C - 36: The elastic AFM based indentation tests 186-190.

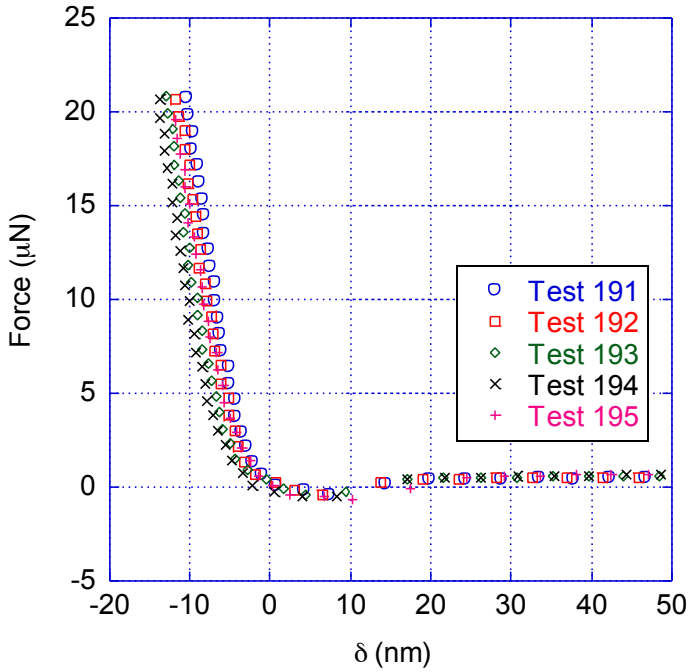

Figure C - 37: The elastic AFM based indentation tests 191-195.

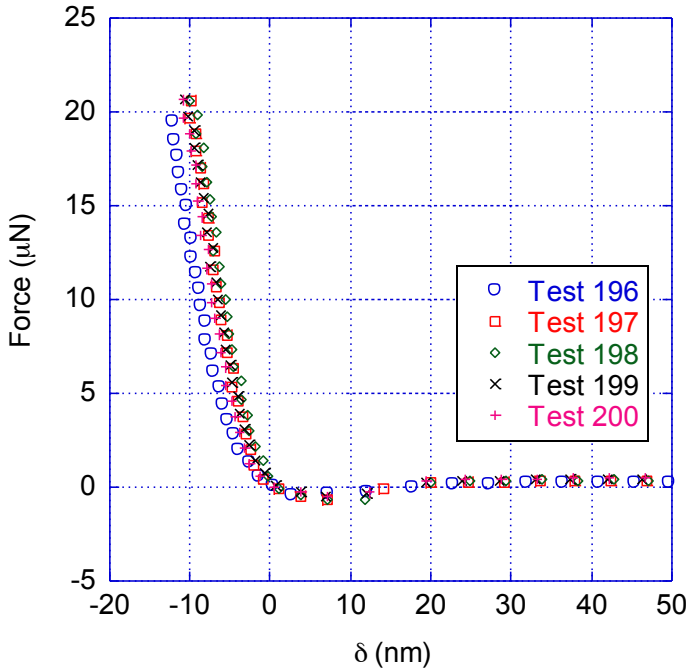

Figure C - 38: The elastic AFM based indentation tests 195-200.

Viscoelastic experimental data

The AFM based creep indentation measurements are presented in this appendix. In the interest of saving space, five indentations will be plotted in each figure. The plots show creep displacement where the initial displacement from each test is subtracted from each data point to normalize all the data to zero at $t = 0^+$. The data presented is broken down by the relative humidity level of the test. All the data presented has been corrected for the drift of the instrument.

40% relative humidity

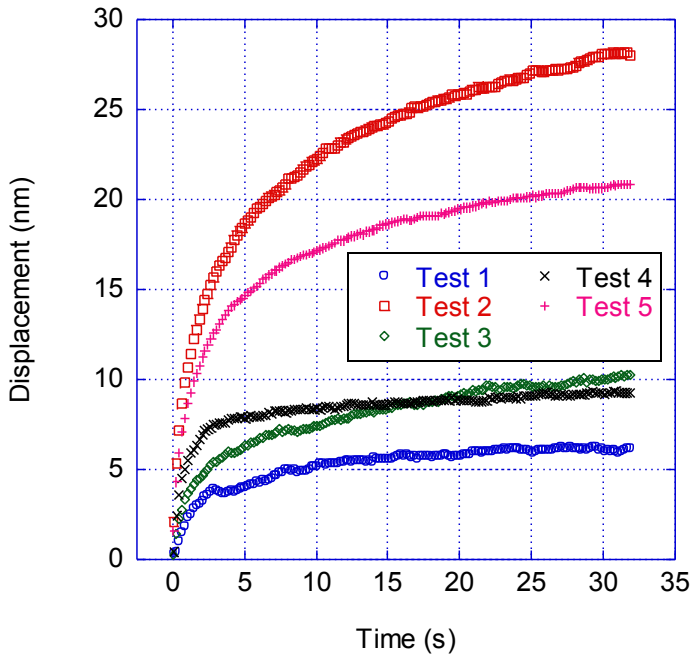

Figure C - 39: The creep displacement for tests 1-5 performed with the atomic force microscope show significant time dependent relaxation of the material.

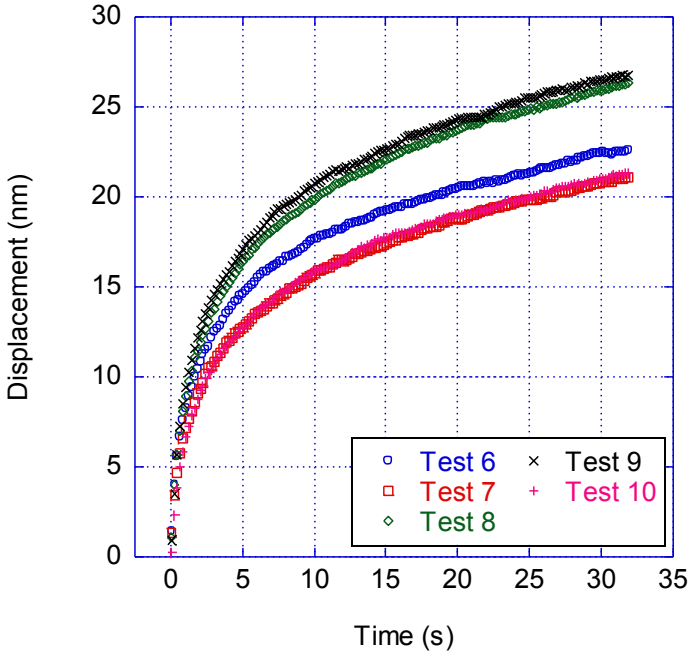

Figure C - 40: The creep displacement for tests 6-10 performed with the atomic force microscope show significant time dependent relaxation of the material.

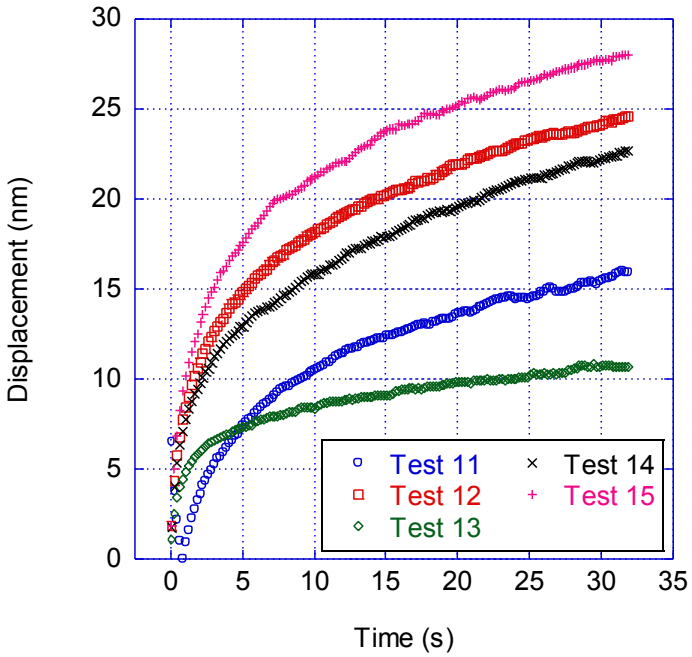

Figure C - 41: The creep displacement for tests 11-15 performed with the atomic force microscope show significant time dependent relaxation of the material.

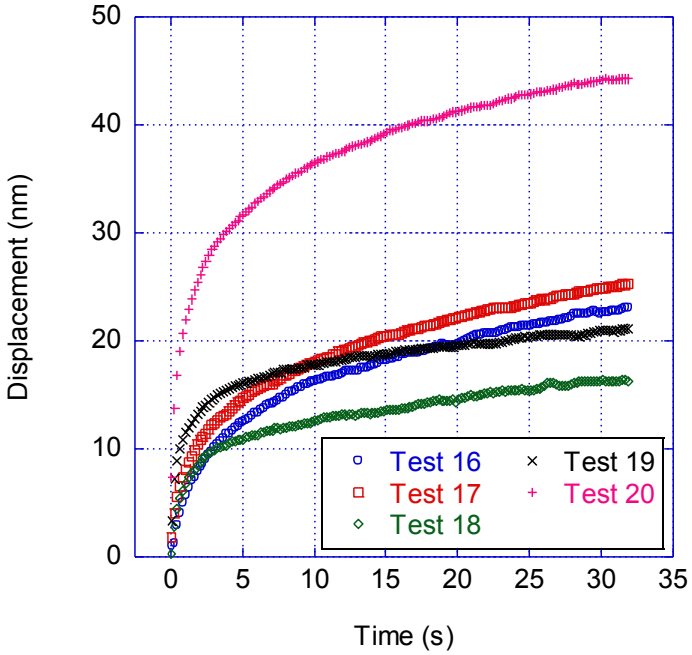

Figure C - 42: The creep displacement for tests 16-20 performed with the atomic force microscope show significant time dependent relaxation of the material.

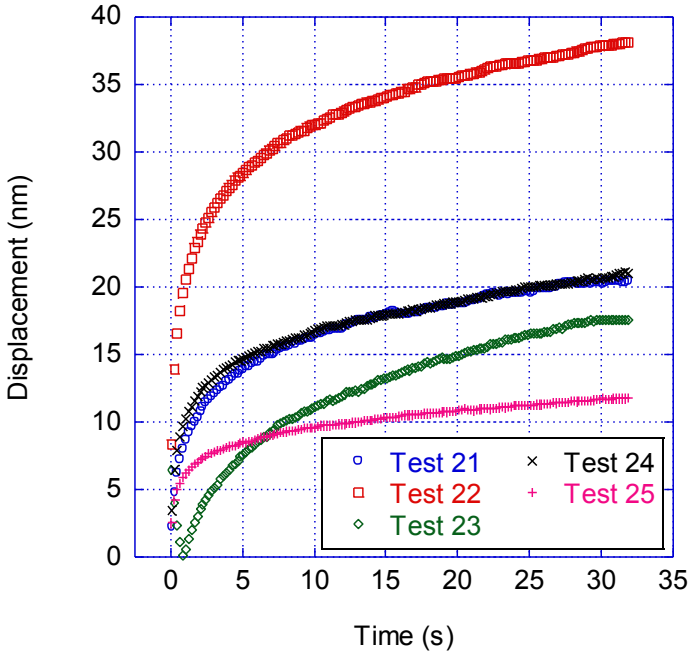

Figure C - 43: The creep displacement for tests 21-25 performed with the atomic force microscope show significant time dependent relaxation of the material.

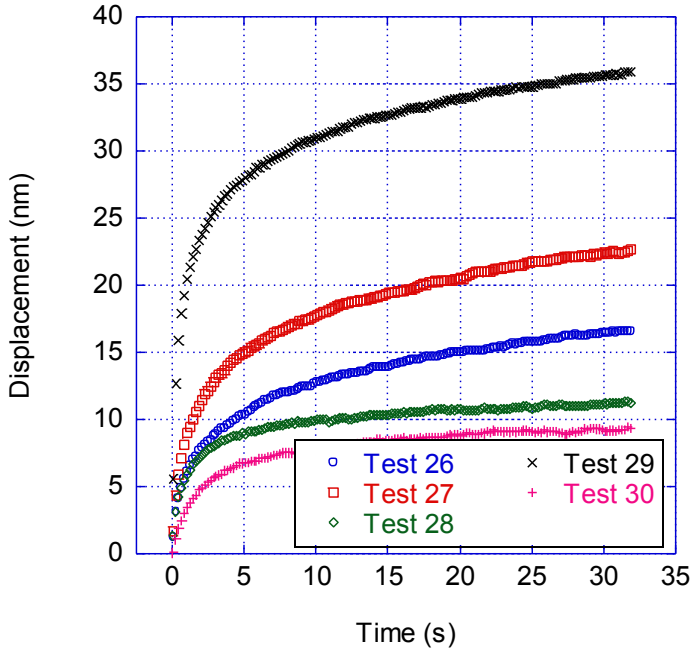

Figure C - 44: The creep displacement for tests 26-30 performed with the atomic force microscope show significant time dependent relaxation of the material.

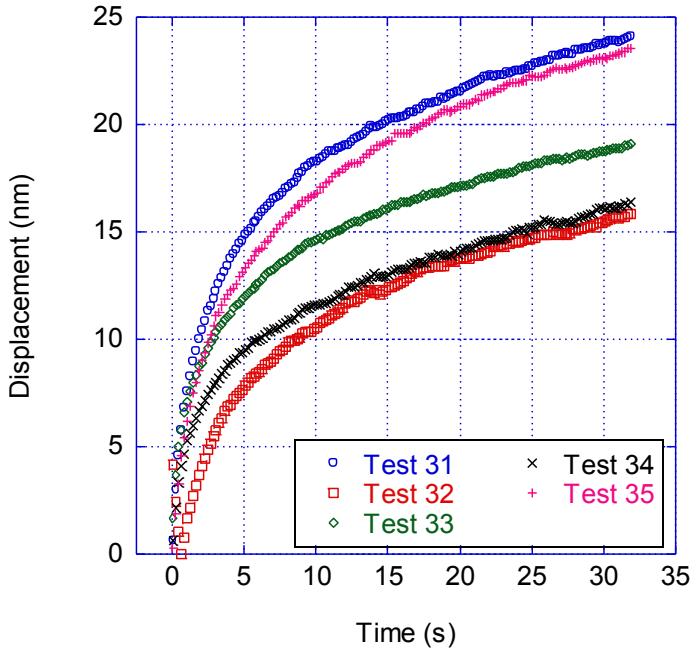

Figure C - 45: The creep displacement for tests 31-35 performed with the atomic force microscope show significant time dependent relaxation of the material.

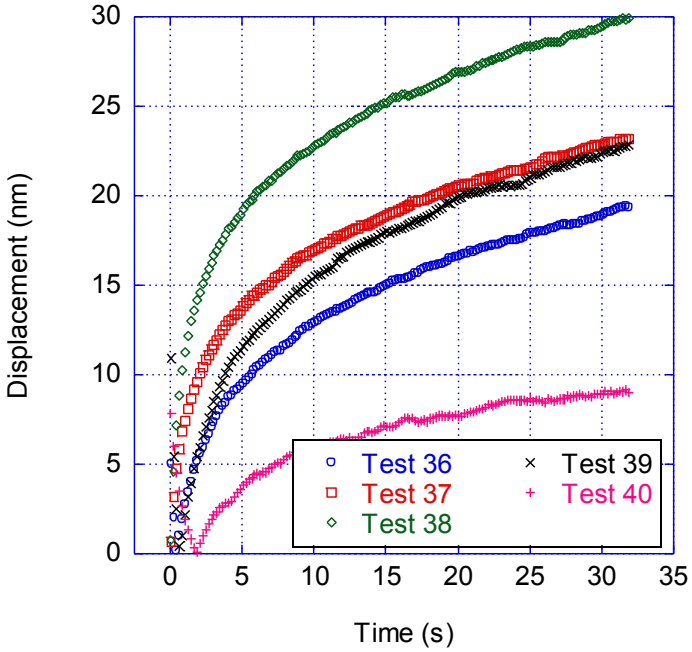

Figure C - 46: The creep displacement for tests 36-40 performed with the atomic force microscope show significant time dependent relaxation of the material.

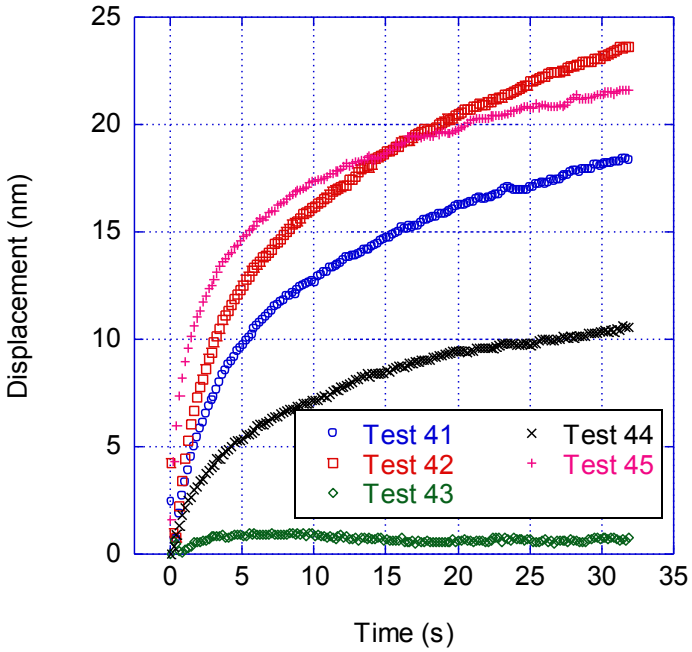

Figure C - 47: The creep displacement for tests 41-45 performed with the atomic force microscope show significant time dependent relaxation of the material.

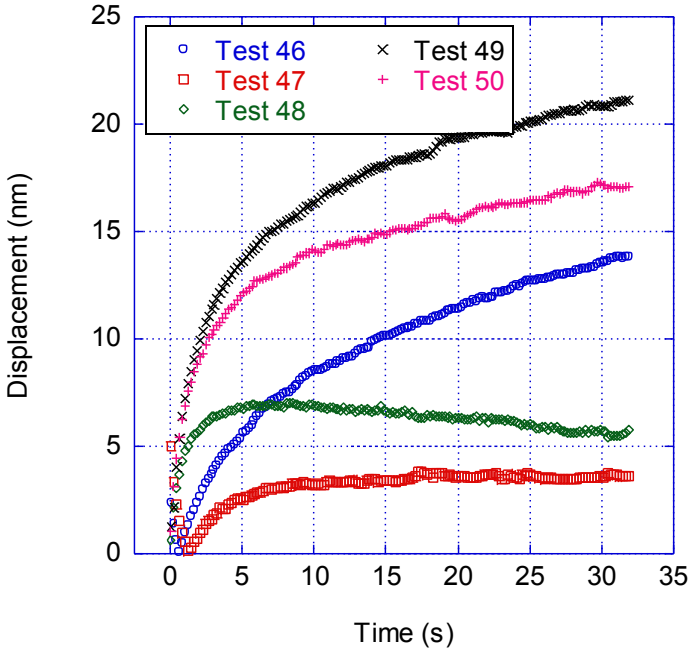

Figure C - 48: The creep displacement for tests 46-50 performed with the atomic force microscope show significant time dependent relaxation of the material.

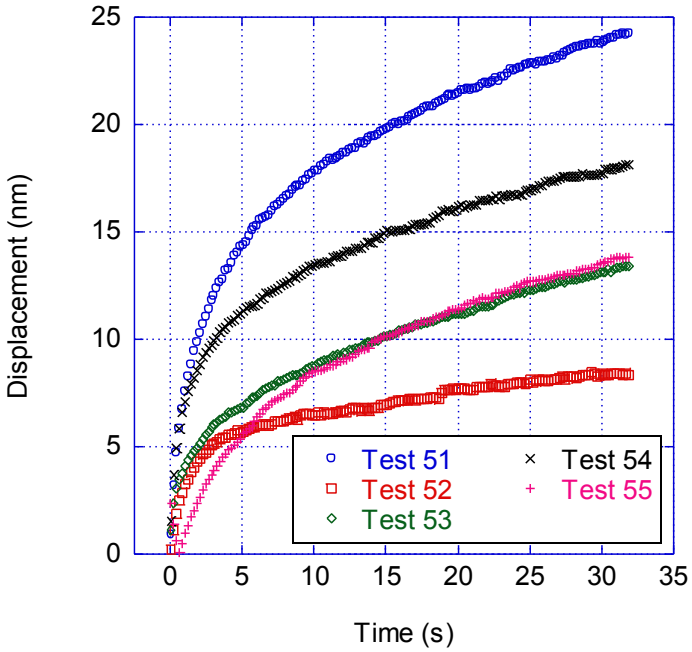

Figure C - 49: The creep displacement for tests 51-55 performed with the atomic force microscope show significant time dependent relaxation of the material.

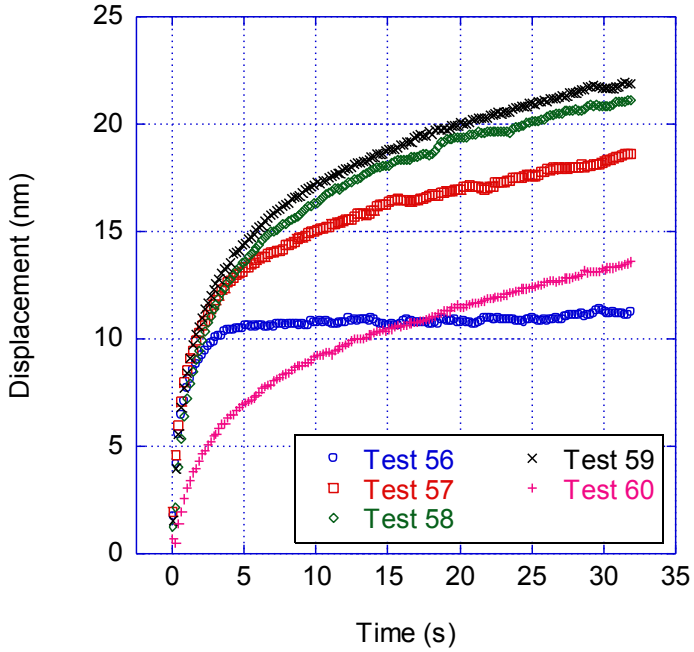

Figure C - 50: The creep displacement for tests 56-60 performed with the atomic force microscope show significant time dependent relaxation of the material.

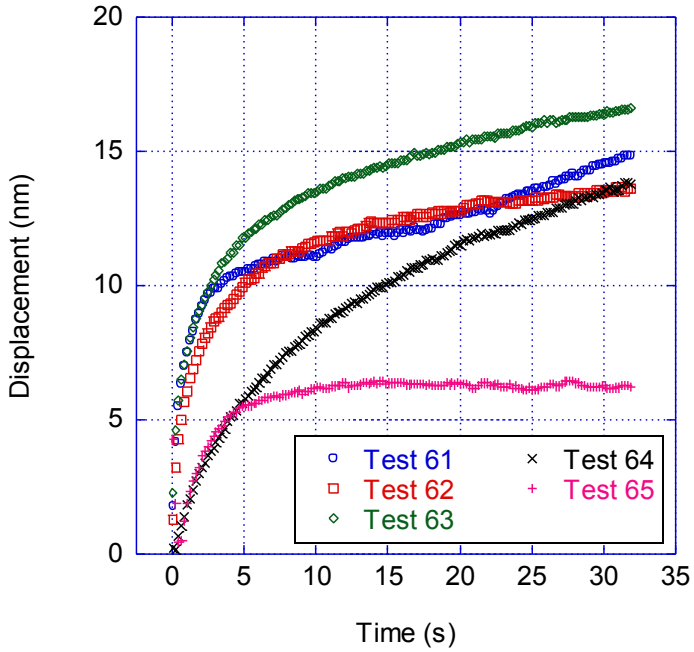

Figure C - 51: The creep displacement for tests 61-65 performed with the atomic force microscope show significant time dependent relaxation of the material.

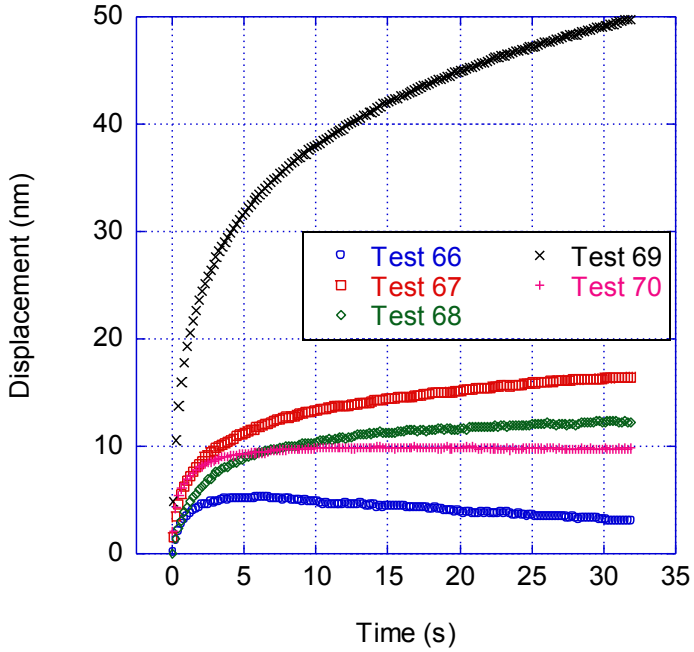

Figure C - 52: The creep displacement for tests 66-70 performed with the atomic force microscope show significant time dependent relaxation of the material.

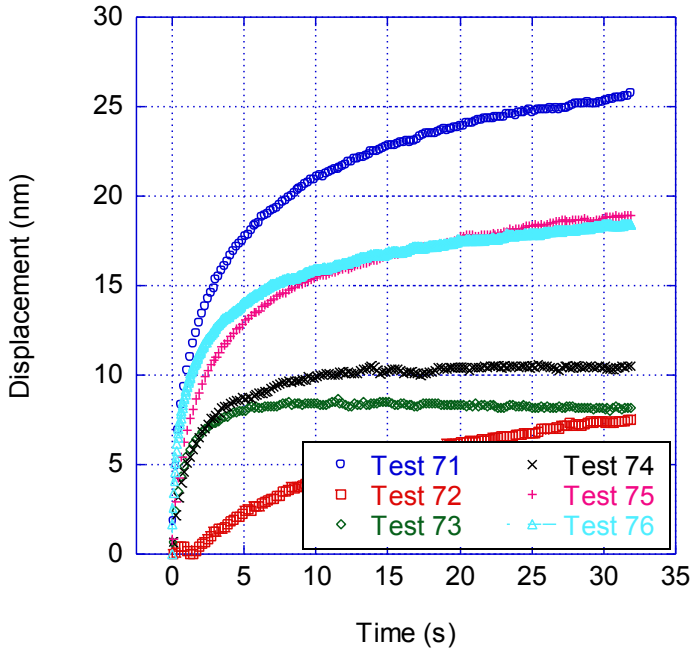

Figure C - 53: The creep displacement for tests 71-76 performed with the atomic force microscope show significant time dependent relaxation of the material.

80% relative humidity

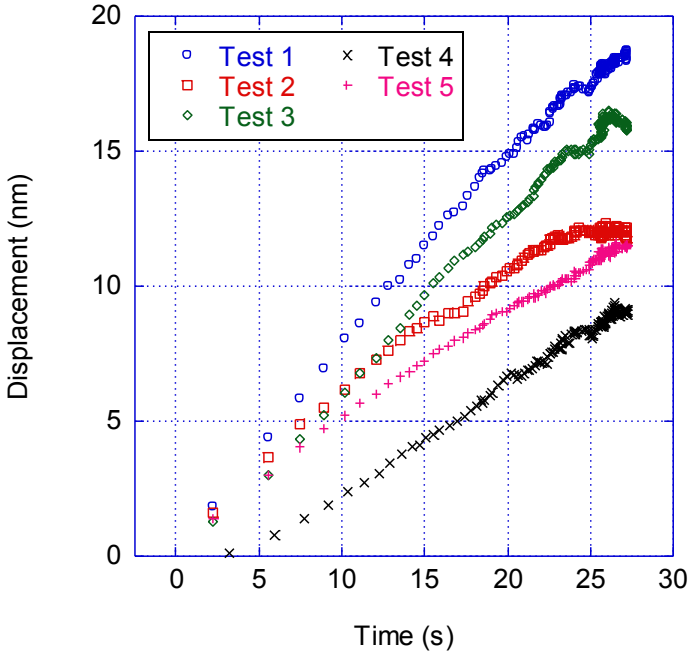

Figure C - 54: The creep displacement for tests 1-5 performed with the atomic force microscope show significant time dependent relaxation of the material.

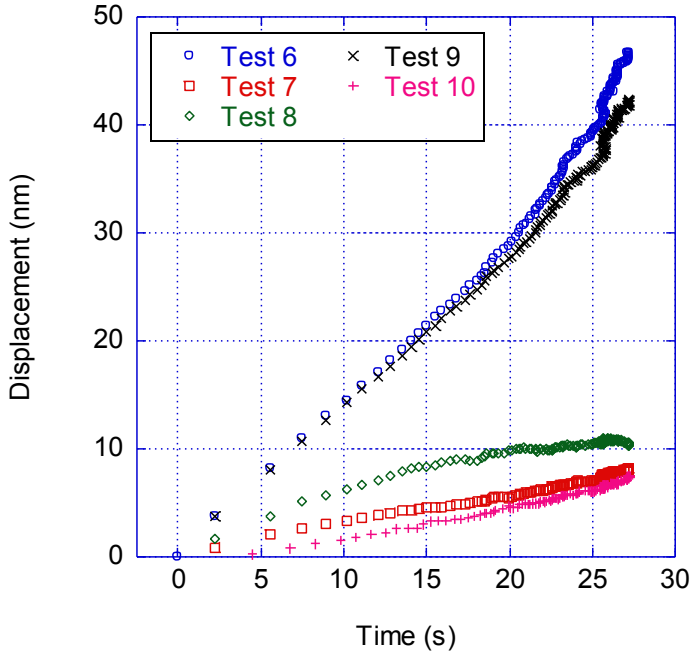

Figure C - 55: The creep displacement for tests 6-10 performed with the atomic force microscope show significant time dependent relaxation of the material.

90% relative humidity

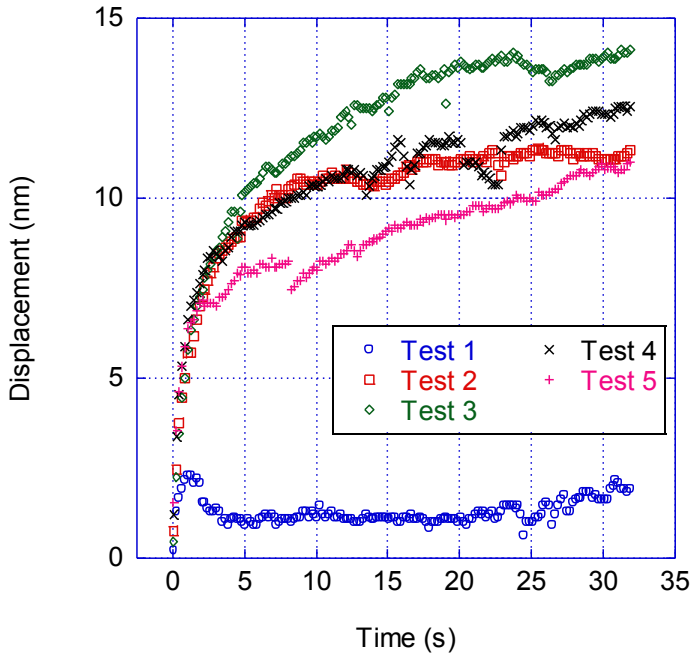

Figure C - 56: The creep displacement for tests 1-5 performed with the atomic force microscope show significant time dependent relaxation of the material.

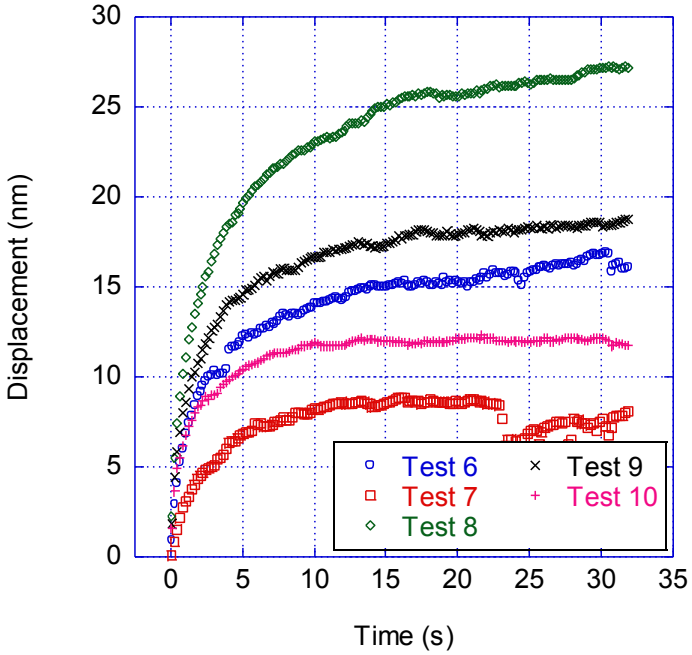

Figure C - 57: The creep displacement for tests 6-10 performed with the atomic force microscope show significant time dependent relaxation of the material.

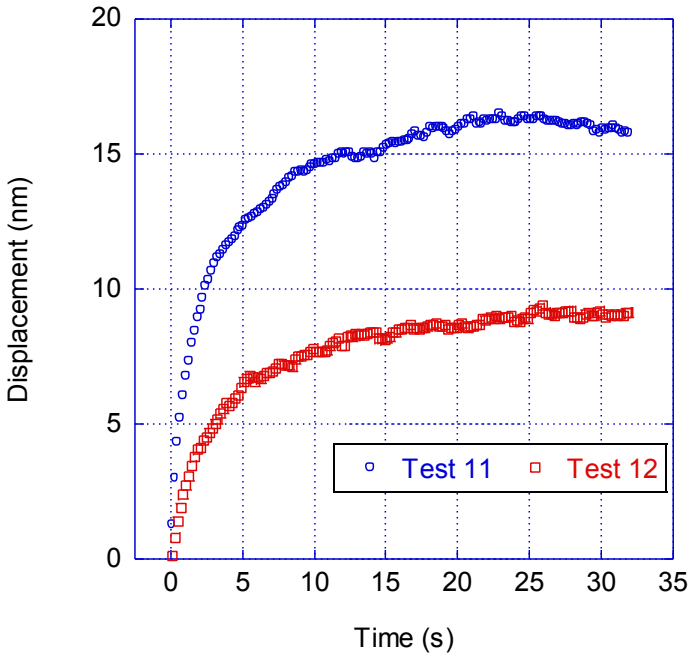

Figure C - 58: The creep displacement for tests 11 and 12 performed with the atomic force microscope show significant time dependent relaxation of the material.

Wet

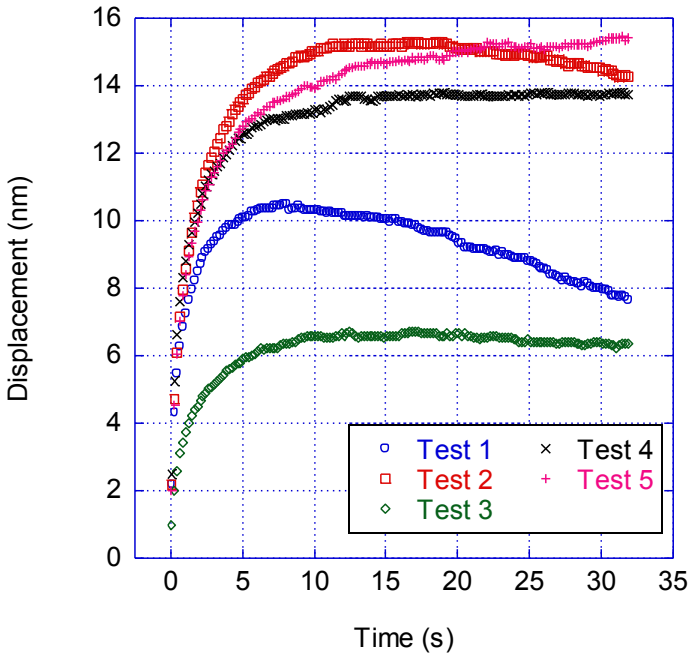

Figure C - 59: The creep displacement for tests 1-5 performed with the atomic force microscope show significant time dependent relaxation of the material.

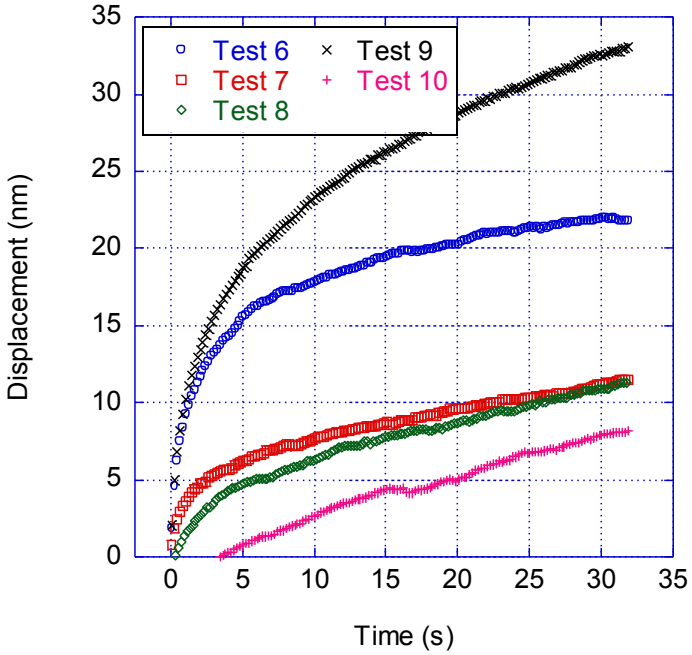

Figure C - 60: The creep displacement for tests 6-10 performed with the atomic force microscope show significant time dependent relaxation of the material.

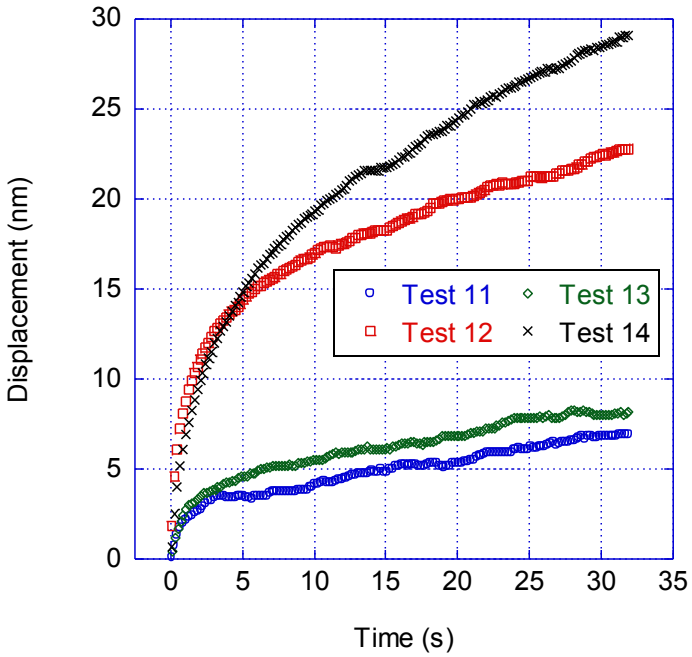

Figure C - 61: The creep displacement for tests 11-14 performed with the atomic force microscope show significant time dependent relaxation of the material.

VITA

Christopher Andrew Jones was born in Corpus Christi, Texas. After graduation from W. B. Ray High School, he enrolled in the 3-2 Engineering program at Southwestern University in Georgetown, Texas where he ultimately earned a Bachelor of Arts degree in physical science in 2006. Within the framework of the 3-2 engineering program, Christopher transferred to Texas A&M University where he earned Bachelor and Master of Science degrees in civil engineering in 2006 and 2008, respectively. During his undergraduate work at Texas A&M, Christopher was supported with the Truman R. Jones ’43 departmental scholarship and during his graduate studies, Christopher received fellowships from the Southwest Region University Transportation Center and the Chemical Lime Foundation. Christopher received his Ph.D. in 2011 and may be reached at PO Box 5800, Albuquerque, NM 87185.